An Improved N_2 Model for Predicting Gas Adsorption in MOFs and Using Molecular Simulation to Aid in the Interpretation of SSNMR Spectra of MOFs

Bianca Provost

Thesis submitted to the
Faculty of Graduate and Postdoctoral Studies
In partial fulfillment of the requirements
For the MSc degree in Chemistry

Department of Chemistry
Faculty of Science
University of Ottawa

Contents

Abstract

Microporous metal organic frameworks (MOFs) are a novel class of materials formed through self-assembly of inorganic and organic structural building units (SBUs). They show great promise for many applications thanks to record-breaking internal surface areas, high porosity as well as a wide variety of possible chemical compositions. Molecular simulation has been instrumental in the study of MOFs to date, and this thesis work aims to validate and expand upon these efforts through two distinct computational MOF investigations.

Current separation technologies used for CO_2/N_2 mixtures, found in the greenhouse gas-emitting flue gas generated by coal-burning power plants, could greatly benefit from the improved cost-effective separation MOF technology offers. MOFs have shown great potential for CO_2 capture due to their low heat capacities and high, selective uptake of CO_2. To ensure that simulation techniques effectively predict quantitative MOF gas uptakes and selectivities, it is important that the simulation parameters used, such as force fields, are adequate. We show that in all cases explored, the force field in current widespread use for N_2 adsorption over-predicts uptake by at least 50% of the experimental uptake in MOFs. We propose a new N_2 model, NIMF (Nitrogen in MoFs), that has been parameterized using experimental N_2 uptake data in a diverse range of MOFs found in literature. The NIMF force field yields high accuracy N_2 uptakes and will allow for accurate simulated uptakes and selectivities in existing and hypothetical MOF materials and will facilitate accurate identification of promising materials for CO_2 capture and storage as well as air separation for oxy-fuel combustion.

We also present the results of grand canonical and canonical Monte Carlo (GCMC and canonical MC), DFT and molecular dynamics (MD) simulations as well as charge density analyses, on both CO_2 and N,N-dimethylformamide adsorbed in $Ba_2TMA(NO_3)$ and MIL-68(In), two MOFs with non-equivalent inorganic structural building units. We demonstrate the excellent agreement found between our simulation results and the solid-state NMR (SSNMR) experiments carried out by Professor Yining Huang (Western University) on these two MOFs. Molecular simulation enables discoveries which complement SSNMR such as the number, distribution and dynamics of guest binding sites within a MOF. We show that the combination of SSNMR and molecular simulation forms a powerful analytical procedure for characterizing MOFs, and this novel set of microscopic characterization techniques allows for the optimization of new and existing MOFs.

Table of Figures

Table of Tables

List of Acronyms

- **ABSL**: **A**utomatic **B**inding **S**ite **L**ocalization
- **BBC**: 4,4',4''-[benzene-1,3,5-triyl-tris(benzene-4,1-diyl)]tribenzoate
- **BDC**: 1,4-**B**enzene**D**i**C**arboxylate
- **BET**: **B**runauer-**E**mmett-**T**eller
- **BTB**: 1,3,5-**B**enzene**T**ri**B**enzoate
- **CCS**: **C**arbon **C**apture and **S**torage
- **CIF**: **C**rystallographic **I**nformation **F**ile
- **CSA**: **C**hemical **S**hift **A**nisotropy
- **CSV**: **C**omma **S**eparated **V**alues File
- **DFT**: **D**ensity **F**unctional **T**heory
- **DOBDC**: 2,5-**D**i**O**xido-1,4-**B**enzene**D**i**C**arboxylate
- **ECP**: **E**ffective **C**ore **P**otential
- **GCMC**: **G**rand **C**anonical **M**onte **C**arlo
- **HF**: **H**artree-**F**ock
- **IAST:** **I**deal **A**dsorption **S**olution **T**heory
- **MAS**: **M**agic **A**ngle **S**pinning
- **MD**: **M**olecular **D**ynamics
- **MIL**: **M**aterials from **I**nstitut **L**avoisier (MOF cataloguing tag)
- **MM**: **M**olecular **M**echanics
- **MOF**: **M**etal **O**rganic **F**ramework
- **NIMF**: **N**itrogen **I**n **M**o**F**s
- **PAW**: **P**rojector **A**ugmented **W**ave method
- **PBE**: **P**erdue, **B**urke, **E**rnzerhof density functional
- **PSA:** **P**ressure **S**wing **A**dsorption
- **PXRD**: **P**owder **X**-**R**ay **D**iffraction
- **QM**: **Q**uantum **M**echanics
- **REPEAT**: **R**epeating **E**lectrostatic **P**otential **E**xtracted **AT**omic charges
- **SBU**: **S**tructural **B**uilding **U**nit
- **SHARCNET**: **S**hared **H**ierarchical **A**cademic **R**esearch **NET**work
- **SSNMR**: **S**olid-**S**tate **N**uclear **M**agnetic **R**esonance
- **TMA:** **T**ri**M**esic **A**cid (benzene-1,3,5-tricarboxylic acid)
- **TraPPE**: **Tra**nsferable **P**otentials for **P**hase **E**quilibria
- **TSA:** **T**emperature **S**wing **A**dsorption
- **VT**: **V**ariable **T**emperature (type of SSNMR experiment)
- **XRD**: **X**-**R**ay **D**iffraction
- **ZIF**: **Z**eolitic **I**midazolate **F**ramework

Simulation Packages

- **FA^{3}PS**: **F**ully **A**utomated **A**dsorption **A**nalysis in **P**orous **S**olids
- **SIESTA:** **S**panish **I**nitiative for **E**lectronic **S**imulations with **T**housands of **A**toms
- **VASP**: **V**ienna **A**b-initio **S**imulation **P**ackage

Acknowledgements

I have spent over 3 years as a member of the Woo group, both as an undergraduate and graduate student. I am incredibly grateful for the lessons I have learned in my time here, whether scientific and on a more personal level. For most of these experiences, I have my supervisor Professor Tom Woo to thank. He took a chance on me nearly four years ago, and he has since allowed me to grow by giving me independence to develop my own ideas and research projects. At the same time, he provided guidance by asking me the difficult questions, challenging me when I was wrong and encouraged me when projects were headed in a good direction. From the very beginning, I was made to feel a part of the team, and I will fondly recall our many group activities and memories made.

During my time spent in Ottawa, I got to meet many knowledgeable group members (so-called "Wookies") who made an impression on me through scientific and leisurely activities. I feel it is important to thank all those people, as in one way or another they contributed to my development during my time as a "Wookie". These people are (in alphabetical order): Peter Boyd, Arif Ismail, Brad Wells, Carlos Campaña, Professor Chris Rowley, Djanet Choukri Bouziani, Eugene Kadantsev, Evans Monyoncho, Hana Ouci-Dureckova, Jason Lo, Lei Guo, Max Roose, Michael Fernandez, Mike Nohra, Mohammad Zein Aghaji, Moshtagh Aljawahari, Phil De Luna, Phil Bulsink, Professor Saied Yeganegi, Saman Alavi, Sarah Piotrkowski and Sean Collins. I wish I could give more detailed credit to each one of these people in this section but, alas I feel I would have too much to write.

For the first part of this thesis project, it was necessary to collect numerical experimental isotherm data from a wide variety of groups. I'd like to extend my sincere thanks to the following experimental MOF scientists who contributed to this work by sending me their

adsorption isotherm uptake data: Professor George Shimizu (University of Calgary) and Dr. Simon Iremonger for the CALF-15 data; Professor Wei-Yin Sun (Nanjing University) for the [Co(HL)]2H_2O data; Dr Qipu Lin and Professor Xianhui Bu (California State University Long Beach) for the CPF-6 data; Professor Michael Zaworotko, Mona Mohamed and Stephen Burd (University of South Florida) for their CROFOUR-1-Ni, MOOFOUR-1-Ni, Cubpy1-SiF_6 and Cubpy2-SiF_6 data; Professor Reiner Staudt (University of Applied Sciences Offenburg) and Dr. Jens Moellmer (Institut für Nichtklassische Chemie e.V.) for the Cu 1,2,4-triazolyl isophthalate based MOF data; Professor Jeff Long and Jarad Mason (University of California, Berkeley) for their MOF-177 data; Professor Sasidhar Gumma and Prashant Mishra (Indian Institute of Technology Guwahati) for their NiDABCO data; Dr. Bai Junfeng and Dr. Zheng (Nanjing University) for their NJU-Bai3 data; Professor Hongcai Zhou and Weigang Lu (Texan A&M University) for their PCN-26 data; Professor Jian Zhang and Fei Wang (Fujian Institute of Research on the Structure of Matter, Chinese Academy of Sciences) for TIF-A1 data; Professor Zhong Li and Zhijuan Zhang (South China University of Technology) for their ZIF-8 data and Dr. Ramanathan Vaihyanathan for his as yet unpublished Ni4PyC data.

For the second part of my thesis project, I would like to give special thanks to Professor Yining Huang and his students, notably Dr. Andre Sutrisno, Wei David Wang and Yue Hu for solid-state NMR data and useful discussions and questions via e-mail and at conferences. I'd also like to acknowledge Fred Perras from the Bryce group for excellent discussions on underlying solid-state NMR theory and practical considerations. Finally, I would like to thank Saman Alavi for great discussions on practical considerations associated with simulating SSNMR lineshapes from molecular dynamics.

Special thanks must go out to my siblings Erica, Max and Zach, as well as to my parents, especially my mother Nicole. My entire family has supported me throughout my Master's, but as my mother has a PhD, she was easily able to empathize, guide and support me as someone who had first-hand experience with graduate school.

Last but not least, I'd like to give special thanks to my partner Tom Daff. The support he has provided throughout this journey has been a blessing. I feel privileged to have been able to discuss and the intricacies of my work with someone whom at once can evaluate them ably and be invested in my happiness and success.

1 – Introduction

Metal organic frameworks, also known as MOFs or porous coordination polymers (PCPs), are an exciting new class of materials which have the potential to be applied to catalysis[1–3], gas capture and separations[4,5], sensing[6,7], photoluminescence[8], electrical conductivity (porous electrodes)[9], drug delivery[10] and many other fields. These microporous crystalline materials, which are formed through self-assembly of inorganic and organic structural building units (SBUs), show great promise thanks to record-breaking internal surface areas, high porosity, a wide variety of possible chemical compositions and high tuneability.

The work in this thesis is composed of two computational-based MOF-related projects. The first topic pertains to the study and development of a new N_2 force field for improved uptake N_2 predictions which leads to better gas mixture (CO_2/N_2 and O_2/N_2) selectivity predictions. The second topic relates the results of in depth studies of the interactions of both CO_2 and N,N-dimethylformamide (DMF) adsorbed on the MOFs MIL-68(In) and $Ba_2TMA(NO_3)$. This is done in order to better understand the interactions at play within these two MOFs, as well as to corroborate solid-state NMR (SSNMR) findings for these two MOFs as derived by Professor Yining Huang's group (Western University).

A more in-depth discussion of defining MOF characteristics and examples of MOFs from literature follows. Then, some of the MOF applications, in particular gas storage and separation, will be explored. Next, an overview of modern MOF characterization techniques shall be presented, with particular emphasis placed on use of SSNMR in this context. Finally, computational contributions to the area of MOFs will be reviewed. The objectives of the thesis will be given at the end of the chapter.

1.1 Metal Organic Frameworks (MOFs)

Interest in MOFs reached an all-time high on the scientific scene in the early 2000s when Yaghi *et al.* published their seminal work on MOF-5[11], a now highly studied porous material, and introduced use of reticular chemistry to achieve unprecedented systematic and controlled design of new MOFs.[12,13] Before the "MOF" term being coined by Yaghi, porous coordination polymers (PCPs) had already been investigated for many years by pioneers such as S. Kitagawa.[14] Since the discovery of this class of materials, hundreds of new MOF structures have been discovered and are being actively tested for a wide variety applications. MOFs have potential for application to a plethora of industrial problems (see section 1.2 for a more detailed account of these).[15]

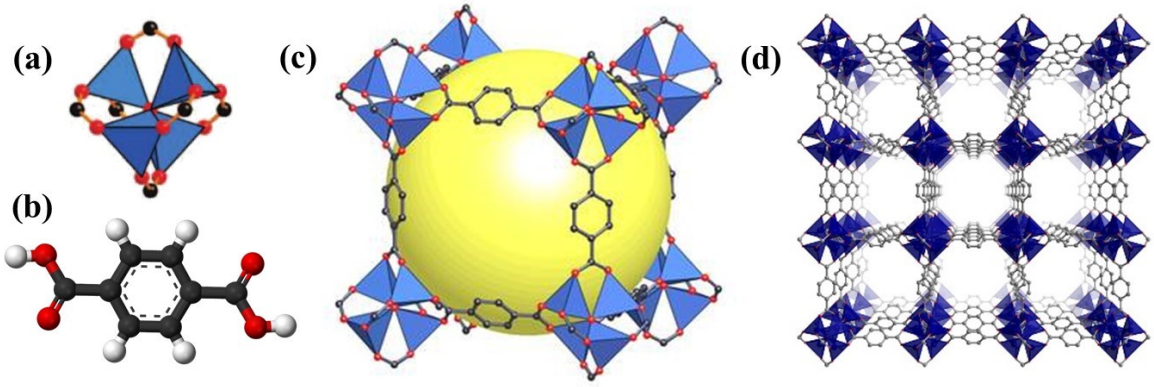

Figure 1-1. *MOF-5, from its Zn_4O tetrahedral SBU (a) and organic H_2BDC SBU (b), a single MOF-5 unit cell with yellow sphere to indicate pore space (c) and finally a slice through the {100} plane of the 3D MOF-5 material (d).*[11]

In terms of basic structure and function, MOFs can readily be compared to zeolites. Conventional zeolites are microporous aluminosilicate materials which can be naturally-occuring or man-made, whereas MOFs are microporous materials which can be synthesized using an infinite combination of inorganic and organic structural building units (SBUs). With this unlimited number of possible SBUs, an enormous number of unique MOFs with different surface properties and chemistry have the potential to be made. Another major

difference is that zeolites are significantly more challenging to synthesize. A little over 200 zeolite structures have been reported up until now[16] and thousands of X-ray crystallographic MOF atomic coordinates have been deposited in the Cambridge Structural Database (CSD), with the number of 3D structures reported doubling on average every 4 years.[17]

One property which makes MOFs unique is the presence of coordinatively unsaturated metal centers, which result in what is called an "open metal site" MOF. These MOFs present certain advantages over their coordinatively saturated counterparts: the exposed metal cation site will interact preferentially with guest molecules, providing strong physisorption character while still remaining energetically well below the strength characteristic of a chemisorption (< 50 kJ/mol). This type of interaction is ideal for easy desorption of adsorbed guests, which is an important feature for many applications. Because of strong, localized binding provided by open metal sites, Mg-MOF-74, a MOF with unsaturated Mg sites and 2,5-dioxido-1,4-benzenedicarboxylate (DOBDC) linkers, demonstrates high and selective CO_2 adsorption of 89 g per kg of MOF at conditions relevant for industrial gas separation and 87% of the captured CO_2 can be released at room temperature.[18,19] These open-metal site materials do present some disadvantages depending on the application at hand. For example, because of the ease of access to the metal center, open-metal site MOFs tend to be much more hydrophilic than many coordinatively saturated MOFs, and will therefore tend to bind water over other guests when humidity is present.[20] Although many coordinatively unsaturated MOFs like Mg-MOF-74 show relatively good stability when in the presence of water, water stability represents a major challenge for many MOFs used as industrial sorbents, as humidity is present in many typical adsorption problems.[21,22] Other gas impurities found in industrial processes such as H_2S, SO_x and NO_x

also have been shown to bind strongly and selectively to certain frameworks resulting in lowered adsorption capacity for another gas of interest.[23–25] Work on better understanding these stability problems is challenging, and it is of great interest based on current literature.[22,26,27]

Recent synthetic advances have allowed MOFs with targeted pore sizes, internal surface areas, specific topologies and surface chemistry to be made and tested. MOFs can be made with essentially any metal center, ranging from explosive-detecting Li-centered MOFs[28] to bio-compatible Fe-based frameworks[29,30] and even luminescent/light-emitting lanthanide-organic frameworks.[31] Pore sizes for these materials may range from mesoporous (between 20 and 500 Å) to microporous (between 2 and 20 Å). IRMOF-74-IX has pore space in the mesoporous regime (pore diameter = 61 Å) and retains its crystal structure after inclusion of green fluorescent protein (GFP) (barrel structure with diameter = 34 Å and length = 45 Å).[32] NU-110 is a MOF with exceptional internal surface area (7140 m^2/g) and holds the world record pore volume (4.40 cm^3/g), which is over 4 times greater than that of average zeolites, silicas or porous carbons.[33,34] At the other end of the pore-size spectrum are MOFs found in the microporous regime, which can be advantageous for gas separations when one guest is preferentially adsorbed thanks to a molecular sieving effect.[35] In other cases, a MOF will structurally transform or "breathe" upon gas adsorption, which will enable pore sizes to change significantly and accommodate larger guest molecules.[36] MOFs also can have unique topologies (the underlying geometry of a framework) and exist in a variety of forms. Traditionally, MOFs tend to be thought of as 3-dimensional, periodic, highly organized insoluble micron-sized crystals, but the MOFs being explored in recent years do not necessarily have all those qualities. The first rationally designed MOF nanotube was

recently reported and shows great promise as a semi-conductor[37], composite materials in which MOFs are anchored on surfaces or particles are emerging as appealing industrial catalysts and as systems for chromatographic separations[38] and around 30 amorphous MOF (aMOF) structures, MOFs which lack any long-range periodicity, have been reported to date and show higher mechanical stability compared to traditional MOFs, which could be very interesting for drug delivery, ion transport and other applications where the collapse of MOF around a guest is desirable.[39]

The constant growing need for new technologies in areas such as power generation and storage, industrial chemical production and pharmaceutical drug delivery pushes synthetic discovery of novel, record-breaking MOF systems like the ones mentioned in this section.

1.2 Applications

Application of MOFs to industrial processes, although promising, is still in a relatively early stage of commercialization.[15] Their potential for impact at a larger scale is certainly recognized, as BASF, arguably the largest chemical company in the world, is now producing MOFs (Basolite® C 300 {HKUST-1}, Basolite ® A100 {MIL-53(Al)} and Basolite® Z1200 {ZIF-8}) at kilogram scales. Their interesting host-guest chemistry offers opportunities in many areas of industrial processes, but for the sake of brevity and because of the nature of the research done for this thesis, only two shall be explored in this chapter: gas capture/storage and gas separation.

1.2.1 Gas capture and storage

Identifying and implementing renewable energy resources to replace rapidly decreasing fossil fuel reserves and to reduce the anthropogenic impact on climate change has

proven to be one of our century's greatest challenges. Hydrogen and methane are promising replacements for traditional gasoline thanks to their cleaner combustion and superior energy payout. One major challenge associated with the use of these gases as fuels is their efficient and high-capacity storage, for example for use in automobiles. MOFs are an excellent adsorbent choice for this application thanks to their particularly low desorption energy requirements as well as their ability to adsorb gas at very high capacity. They are seriously being explored to store alternative fuels, and competitive MOF candidates have been identified.[40–43] MOF-210 can store up to 15 weight percent H_2 at 80 bar and 77K, whereas the U.S. Department of Energy's 2017 target for H_2 storage is 5.5 wt% and 45 g L^{-1} at temperatures between 233-333K and under a maximal delivery pressure of 100 bar.[40,44] Mercedez-Benz recently released a research vehicle, the F125, which makes use of a MOF reservoir to store H_2 gas.[45] BASF announced that they were conducting trials for storage of methane gas in MOF-filled vehicle tanks.[46] Storage of fuels in MOFs is certainly an exciting area with a very real potential for application, but gas storage in MOFs is not limited to fuels.

1.2.2 Gas separation

CO_2 is a greenhouse gas which is contributing to the depletion of the ozone layer, and about 80% of worldwide CO_2 emissions are generated through fossil fuel combustion.[47] 60% of worldwide carbon emissions originate from electricity generation, a stationary point source, which accounts for 28 billion tons of greenhouse gas released in 2004.[48] Because of its stationary nature and massive CO_2 production, a promising strategy to reduce CO_2 emissions is to make use of carbon capture and storage (CCS) to trap the gas directly at the source. The gas can then be transported and injected into a permanent storage site, such as

empty saline aquifers, depleted oil fields or even buried in the the deep ocean floor.[49,50] At present, large scale CCS is not occurring, because current CO_2 scrubbing technologies require too much energy and are not cost effective. One such technology is liquid amines, which are inefficient due to requiring high regeneration temperatures which arise from high heat capacity and to a lesser extent the chemisorptive nature of the adsorption process.[51] A key advantage of MOFs is that their regeneration costs are comparably small thanks to their lower heat capacity. Because amine concentrations in solution must be low to prevent corrosion of the vessel which contains them, their heat capacities are very close to that of pure water (C_p = 4.18 J K^{-1} g^{-1}) whereas a representative MOF like MOF-177 ($Zn_4O(BTB)_2$, where BTB = 1,3,5-benzenetribenzoate) has a much lower heat capacity at ambient temperature (C_p ~ 0.5 J K^{-1} g^{-1}) and even at higher temperatures (C_p ~ 1.6 J K^{-1} g^{-1} at 498K).[52] In addition to the significantly lowered desorption costs, MOFs have shown excellent capacity for CO_2 with the current capacity record-holder being MOF-200 ($Zn_4O(CO_2)_6$[BBC], where BBC = 4,4′,4″-[benzene-1,3,5-triyl-tris(benzene-4,1-diyl)]tribenzoate) with an exceptional CO_2 capacity of 2347 mg/g of MOF (298K, 50 bar).[44] This translates to potential for storage of 17 times as much CO_2 as an empty pressurized gas cylinder at 35 bar.[17]

A major concern with CCS and other gas capture applications is separation of the target gas from a mixture. In the context of CCS, the separation process accounts for around 70% of the cost of the operation.[49] As an example, typically the gas produced from coal combustion contains 15% CO_2 in addition to 73-77 % N_2, 5-7% H_2O and trace amounts of O_2, SO_x, NO_x, CO and HCl which all must be separated from CO_2 by the sorbent used.[51] In the event that non-target gases are adsorbed, not only will efforts be wasted extracting and

storing non-greenhouse gases but it is possible that contaminant gases may irreversibly bind to the framework or even induce collapse of the framework, which may significantly reduce a MOF's capacity for adsorbing carbon dioxide over time.

There are three CCS strategies to mitigate CO_2 emissions generated by power plants.[51] Two of these strategies can be used when building new power plants, and one strategy is to be used to retrofit existing plants. The first strategy to be used for new plants is called oxyfuel combustion. In this strategy, N_2 is separated from air to provide a pure O_2 stream for higher efficiency coal or gas combustion. The final products of this combustion process are CO_2 and H_2O gases, which needn't be separated from any other gases. In the second approach called pre-combustion separation, also aimed at new power plants, coal is first gasified at elevated temperature and high pressure in the presence of oxygen or air to produce syn gas, which is mainly composed of H_2 and CO. The syn gas is then further reacted with steam at high pressure and moderate temperatures to form H_2 and CO_2, which together are known as "shifted syn gas". H_2 is the fuel intended for combustion, and therefore must finally be separated from CO_2. The third and final strategy which is of great interest because it can be directly applied to existing power plants is called post-combustion separation. This approach consists of separation of CO_2 from the flue gas generated after combustion, which contains mostly N_2 and CO_2. Evidently, these three approaches involve separation of very different gas mixtures. In spite of the differences, MOFs have shown great promise for separation of the gas mixtures in these three cases as well as in many other areas including air separation (O_2/N_2), landfill gas separation and natural gas purification (CH_4/CO_2), hydrocarbon (alkane or olefin) separation[53] and even separation of toxic carbon monoxide, ammonia or chlorine from other gases or air.[35,54,55]

In any of the three CCS strategies listed above, the MOF can be regenerated in a few different ways. The two main methods used are entitled Temperature Swing Adsorption (TSA), Pressure Swing Adsorption (PSA).[51] TSA makes use of temperature increase for desorption, whereas PSA make use of a decrease in pressure. TSA in particular is promising because low-grade heat emitted by various functions within the power plant can be recycled for this process, reducing the cost of the operation. Although TSA is promising for post-combustion CCS, PSA is showing more promise for pre-combustion CCS, because the gas stream is already pressurized in this process. Combinations of these methods (ie. TPSA) have also been shown to be effective for certain adsorbents.[56] In any event, the regeneration method is another parameter to consider in the optimization of MOFs for CCS, as desorption will be ideal when the regeneration process conditions match those of the selected adsorbent.[56]

To date, many different reasons for why a MOF has the capacity to selectively adsorb certain gases over others have been identified.[5] In certain cases, gases can be separated simply based on their difference in size or shape with respect to the MOF's pore aperture. This is observed for CO_2 (smallest dimension: 2.5 Å) and CH_4 (smallest dimension: 3.8 Å) gases in the MOF MIL-96, $Al_{12}O(OH)_{18}(H_2O)_3(Al_2(OH)_4)[BTC]_6 \cdot 24H_2O$ (pore aperture: 2.5 – 3.5 Å), which selectively captures CO_2 due to pore aperture size constraints.[57] Adsorbate-surface interactions also tend to play an important role in separation of certain guests. Again, CO_2 and CH_4 can be compared in this context. CO_2 has a strong quadrupole moment and it has been shown that interactions with the framework can heavily influence adsorption capacity.[58] For other gases like CH_4 which has no quadrupole moment, identifying high capacity materials is a "space-filling" problem, meaning that a large pore volume as opposed

to optimal pore wall chemistry will provide optimal uptake.[59] This difference in molecular properties can be exploited for many gas mixtures, as was done by Bae *et al.* to optimize CO_2 uptake through design of the cavity surface of $[Zn_2(4,4',4'',4'''$- benzene-1,2,4,5-tetrayltetrabenzoate)(py-$CF_3)_2]_n$, which selectively captures CO_2 over N_2 thanks to -CF_3 functionalization intended to interact favourably with carbon dioxide.[58] More complex reasons for selective adsorption occur, such as framework "breathing" mentioned earlier where framework flexibility can play a role in selective gas capture[36], structural rearrangements induced by surface-adsorbate interactions, or even adsorbate specific "gate-opening" pressures. It is worth noting however that these complex adsorption selectivity mechanisms may result in greater engineering challenges, so rigid MOFs will be more easily applied for most real-world problems.

It is evident that microscopic guest-host interactions within MOFs must be studied in order to provide appropriate explanations for observed selectivities and uptake capacities. Experimental tools do exist to probe these phenomena (for more details on some of these techniques, see the introduction to Chapter 4), but calculations can provide insights not otherwise easily obtained through other means. The next chapter discusses some of the advances in experimental characterization carried out in MOFs.

1.3 MOF Characterization

Finding links between properties which arise from a MOF's specific structural features and guest-host interactions is of great importance. Experimental characterization of MOFs is crucial for rational design of better materials as well as for improvement of existing MOFs.

One of the techniques used most often for characterization of materials (including MOFs) is single-crystal X-ray Diffraction (XRD), also called x-ray crystallography. In this

method, a beam of X-rays are projected upon a crystalline material. The crystal will then diffract the incident beam, and this diffracted beams' angle and intensity will provide information regarding the density of electrons within the structure. The electron density can in turn be correlated with more useful information such as atomic coordinates, chemical bonds and crystallographic disorder caused by multiple favourable configurations of the atomic positions.

In practice, it can be difficult to obtain sufficient and/or high-quality MOF single crystals for X-ray crystallography experiments. In cases where MOF single crystals are available, they often have issues with excessive internal thermal motions, severe crystallographic disorder as well as the inability to provide information on trapped guest molecules. In cases where it is impossible to make use of a single crystal for XRD, it is also possible to perform x-ray experiments on a powder (powder x-ray diffraction or PXRD), but these provide more limited structural information for a material. Therefore, other characterization techniques which do not require single crystals are necessary to better understand MOF structure.

Up to date, a large number of experimental tools have been used to characterize MOFs in different ways. These include (but are not limited to): Infrared spectroscopy[60], low-temperature X-ray and neutron diffraction[61–63], inelastic neutron scattering[64], FTIR spectroscopy[65] and Electron Paramagnetic Resonance (EPR) Spectroscopy[66]. Use of multiple characterization tools is also often performed to gain access to information not readily provided by either tool alone.[60,61] The characterization tool of main interest for this thesis however is solid-state NMR (SSNMR). Use of SSNMR as a characterization technique for MOFs and gas adsorption in MOFs is a fairly recent development in the NMR field.

However, SSNMR has been used for some time for characterization of microporous materials on other related porous materials. In terms of zeolite structural characterization, SSNMR gained wide acceptance early in the 80s, and has since been applied to a wide array of macromolecules and materials, from proteins to polymers to porous carbons.[67,68] SSNMR has also been used extensively to characterize hybrid organic-inorganic complexes (ie. Hybrid silicas, hybrid cationic/anionic clays, biomaterials and coordination polymers such as MOFs) for some time.[69,70] The highly variable composition of MOFs has greatly extended the number of SSNMR-active nuclei under currently investigation for characterization of nanoporous materials.[68] To better understand the choice of nuclei present in this thesis work, some background on the common MOF SSNMR nuclei will briefly be presented. Ideas in NMR crystallography, which forms a major basis for this work, shall also be reviewed. Recent reviews by Sutrisno and Huang[71,72] and Brunner *et al.*[73] more thoroughly outline the progress which has been made in MOF-based SSNMR over the last decade.

SSNMR analyses in MOFs usually aim to accomplish one or both of two goals: characterization of the framework (1) and characterization of the interactions a framework has with guest molecules (2). SSNMR analyses using specific nuclei will accomplish goals related in some way to one of these two goals. An established technique used in the study of porous materials which is used solely for framework characterization is ^{129}Xe SSNMR. Because of its low reactivity, it serves as an excellent probe to determine the porosity of a MOF as well as to identify binding locations within a MOF, as many studies have already shown.[74–77] ^{129}Xe SSNMR was even used to follow a phase transition in MIL-53(Al), a MOF well known for its breathing behaviour.[78] Deuterium (^{2}H) SSNMR is used regularly in the study of MOFs, as it can indicate the motion of organic SBUs as well as give information on

the dynamics of organic linkers.[79–84] Of course, SSNMR performed on the nuclei for elements included within the MOF structure are also performed. In particular, ^{1}H and ^{13}C, which are often performed together, are used extensively to confirm organic SBU identity within a framework, indicate the presence of functional groups after linker modification as well as to probe adsorption of guest molecules.[82,83,85–93] SSNMR studies using ^{13}C and ^{1}H nuclei to probe guest-host interactions have provided insight for a wide variety of potential MOF applications and problems, from testing MOFs for drug delivery[92] to diffusion of hydrocarbons in MOFs[93] to evaluating CO_2 capture in open metal site MOFs.[94,95] ^{15}N SSNMR is used in the same ways, but is comparatively less common that ^{1}H and ^{13}C due to low natural abundance of the isotope.[85,87–89] Studies on MOFs using ^{17}O and ^{11}B isotopes have also recently begun to emerge.[66,96]

A category of nuclei which have contributed greatly to the study of MOFs are metal nuclei. The most common metal nuclei studied include ^{27}Al, ^{71}Ga and ^{45}Sc, which have all been used successfully to directly probe the metal environment in Al, Ga and Sc-containing MOFs.[86,90,91,97–100] The three metals listed are however not the metal centers which are found in many important MOFs in literature. It is difficult to analyze MOFs containing Zn, Mg and Zr for example because the corresponding nuclei, ^{67}Zn, ^{25}Mg and ^{91}Zr all have low natural abundances, low gyromagnetic ratios and large quadrupole moments in addition to being in a relatively low concentration in MOFs. This results in low-sensitivity and broad resonances, which makes peak assignment and identification challenging.[71] Recent advances in SSNMR methods and instrumentation, such as ultra-high magnetic fields, has made studies on these nuclei possible, as evidenced by recent studies by Professor Huang's group at Western with ^{67}Zn on ZIFs 7, 8, 4 and 14[101] and ^{25}Mg on MOFs α-$Mg_3(HCOO)_6$ (commercially known as

Basosive M050)[102] and CPO-27-Mg.[103] To the best of our knowledge, SSNMR studies on ^{115}In and $^{135/137}$Ba, which feature prominently in this work, have yet to be reported in literature.

Although SSNMR spectroscopy can provide a great deal of information on a MOF's structure and interaction with guest molecules, SSNMR experiments on MOFs and other microporous materials are often most useful when coupled with other structure probing tools. Several examples in the literature of combined SSNMR experiments and calculations (including DFT calculations, MD simulations and other simulation techniques) have been shown to provide information which cannot be acquired by either tool alone.[77,88,101] NMR crystallography is an emerging field in which a combination of NMR studies, powder XRD and simulations are coupled to elucidate structural information.[104,105] These types of multi-component studies are being carried out presently in MOFs as well as other porous materials, and constitute an especially promising complement and supplement to pure diffraction studies.[100–102]

1.4 Molecular Simulation of MOFs

As computational resources continue to increase in power and performance, computations are playing a more important role in many areas of research and development, particularly in materials chemistry.[106,107] Computational chemistry is another characterization tool which is particularly well-suited for predictive analysis of MOFs, as these materials can be time consuming and challenging to synthesize. As these materials are unique, new computational methods are necessary to make accurate assessments regarding their chemistry. Efforts have been such in the area of method development for simulations in MOFs that they have recently warranted a full review.[108] Now that the framework

required for carrying out calculations in MOFs is relatively mature, the potential for computations to benefit MOF research presents itself in many ways. Studies of this nature include (but are not restricted to): testing the adsorption properties of hypothetical or real MOF structures to determine whether they are worthy of expensive experimental synthesis and testing, providing explanations for macroscopic phenomena (ie. Selectivity for one guest over another[109], high uptake capacities[110], chemical/mechanical stability[111], etc.) from molecular insights and calculating quantities which are difficult to obtain experimentally, such as gas diffusion properties, guest binding sites and multi-component gas adsorption.[112–119]

In the context of gas adsorption specifically, grand canonical Monte Carlo (GCMC) molecular simulation can give great insight into prediction and analysis of gas adsorption properties in MOFs. These calculations have been successful in quantitatively reproducing experimental adsorption data as well as providing atomistic-level information not easily obtainable through experimental means in MOFs.[108,119,120] The reader is referred to Chapter 2 for further information on computational techniques used throughout this thesis (including GCMC), all of which are commonly employed by MOF researchers.

From the first real computational study on a MOF reported in 2004[121] until now, much progress has been made in computational method development for simulations of MOF materials as well as in production of meaningful, quantitative results which can truly guide modern MOF chemistry. The work from this thesis contributes to both MOF method development and applied computational MOF research, as Chapter 3 addresses gas force field parameterization and Chapter 4 demonstrates computational – experimental synergistic MOF research. The next chapter provides an outline of the entire thesis.

1.5 Thesis Goals and Outline

We have observed that a popular force field used for collecting simulated N_2 gas uptake isotherms in MOFs called N_2-TraPPE typically shows overestimation in uptake compared to experiment. Therefore, the goal of the first part of this thesis will be to further study the performance of the N_2-TraPPE force field for gas adsorption in MOFs and to develop an improved force field for high accuracy N_2 adsorption in MOFs. To study the performance of the existing and new force fields, we will compare the simulated N_2 uptake isotherms we derive with analogous experimental isotherms. The new force field will accurately reproduce experimental data by fitting the parameters directly to experimental N_2 uptake isotherms in a wide variety of MOFs.

In the second part of this thesis, we provide an in depth molecular simulation study of CO_2 and DMF adsorption in the MOFs MIL-68(In)[122] and $Ba_2TMA(NO_3)$[123]. This is done to provide insight on the guest-host interactions within these MOFs as well as to complement the SSNMR experiments carried out by Professor Yining Huang's group on MIL-68(In) and $Ba_2TMA(NO_3)$. The broad aim of this part of the thesis is to contribute our findings to the growing field of NMR crystallography, and to validate combined use of SSNMR and molecular simulation for characterization of MOFs.

The thesis is organized as follows. In Chapter 2, the general theory and methods used throughout this thesis project will be explored. This includes combined used of Density Functional Theory (DFT) electronic structure calculations, the REPEAT algorithm for charge calculation and finally the grand Canonical Monte Carlo (GCMC) algorithm for determining gas uptake in MOFs. The Automated Binding Site Localization code's function (ABSL) will also be outlined.

Although a general introduction is provided in this first chapter, this thesis project encompasses two distinct parts, each of which addresses a fairly different research interest related to MOFs. A more in-depth introduction and goals for each project shall be provided in Chapters 3 and 4. The first project, "Parameterization of N_2 TraPPE Model for Improved Simulated CO_2/N_2 and O_2/N_2 Selectivity Predictions in Metal Organic Frameworks", shall be presented in Chapter 3 and the second project, "Using Molecular Simulation to Aid in the Interpretation of Solid-State NMR spectra of Metal-Organic Frameworks" shall be presented in Chapter 4. In addition to the general methods and theory presented in Chapter 2, specific methods were used for each project. These will also be presented as sub-sections in Chapters 3 and 4.

Finally, in Chapter 5 conclusions shall be drawn for each part of the thesis work conducted and directions for future work shall be presented. Appendices are available at the end of the thesis (Chapter 6).

1.6 References

(1) Lee, J.; Farha, O. K.; Roberts, J.; Scheidt, K. a; Nguyen, S. T.; Hupp, J. T. *Chem. Soc. Rev.* **2009**, *38*, 1450–9.

(2) Corma, A.; García, H.; Llabrés i Xamena, F. X. *Chem. Rev.* **2010**, *110*, 4606–55.

(3) Ma, L.; Abney, C.; Lin, W. *Chem. Soc. Rev.* **2009**, *38*, 1248–56.

(4) Farha, O. K.; Yazaydın, A. Ö.; Eryazici, I.; Malliakas, C. D.; Hauser, B. G.; Kanatzidis, M. G.; Nguyen, S. T.; Snurr, R. Q.; Hupp, J. T. *Nat. Chem.* **2010**, *2*, 944–8.

(5) Li, J.-R.; Kuppler, R. J.; Zhou, H.-C. *Chem. Soc. Rev.* **2009**, *38*, 1477–504.

(6) Xie, Z.; Ma, L.; deKrafft, K. E.; Jin, A.; Lin, W. *J. Am. Chem. Soc.* **2010**, *132*, 922–3.

(7) Kreno, L. E.; Leong, K.; Farha, O. K.; Allendorf, M.; Van Duyne, R. P.; Hupp, J. T. *Chem. Rev.* **2012**, *112*, 1105–25.

(8) Allendorf, M. D.; Bauer, C. a; Bhakta, R. K.; Houk, R. J. T. *Chem. Soc. Rev.* **2009**, *38*, 1330–52.

(9) Givaja, G.; Amo-Ochoa, P.; Gómez-García, C. J.; Zamora, F. *Chem. Soc. Rev.* **2012**, *41*, 115–47.

(10) Horcajada, P.; Gref, R.; Baati, T.; Allan, P. K.; Maurin, G.; Couvreur, P.; Férey, G.; Morris, R. E.; Serre, C. *Chem. Rev.* **2012**, *112*, 1232–68.

(11) Li, H.; Eddaoudi, M.; O'Keeffe, M.; Yaghi, O. M. *Nature* **1999**, *402*, 276–279.

(12) Eddaoudi, M.; Kim, J.; Rosi, N.; Vodak, D.; Wachter, J.; O'Keeffe, M.; Yaghi, O. M. *Science* **2002**, *295*, 469–72.

(13) Chae, H. K.; Siberio-Pérez, D. Y.; Kim, J.; Go, Y.; Eddaoudi, M.; Matzger, A. J.; O'Keeffe, M.; Yaghi, O. M. *Nature* **2004**, *427*, 523–7.

(14) Kondo, M.; Okubo, T.; Asami, A.; Noro, S.; Yoshitomi, T.; Kitagawa, S.; Ishii, T.; Matsuzaka, H.; Seki, K. *Angew. Chemie Int. Ed.* **1999**, *38*, 140–143.

(15) Czaja, A. U.; Trukhan, N.; Müller, U. *Chem. Soc. Rev.* **2009**, *38*, 1284–93.

(16) Baerlocher, C.; McCusker, L. B. Database of Zeolite Structures: http://www.iza-structure.org/databases/ (accessed Jul 10, 2014).

(17) Furukawa, H.; Cordova, K. E.; O'Keeffe, M.; Yaghi, O. M. *Science* **2013**, *341*, 1230444.

(18) Britt, D.; Furukawa, H.; Wang, B.; Glover, T. G.; Yaghi, O. M. *Proc. Natl. Acad. Sci. U. S. A.* **2009**, *106*, 20637–40.

(19) Dietzel, P. D. C.; Blom, R.; Fjellvåg, H. *Eur. J. Inorg. Chem.* **2008**, *2008*, 3624–3632.

(20) Schoenecker, P. M.; Carson, C. G.; Jasuja, H.; Flemming, C. J. J.; Walton, K. S. *Ind. Eng. Chem. Res.* **2012**, *51*, 6513–6519.

(21) Küsgens, P.; Rose, M.; Senkovska, I.; Fröde, H.; Henschel, A.; Siegle, S.; Kaskel, S. *Microporous Mesoporous Mater.* **2009**, *120*, 325–330.

(22) Jasuja, H.; Huang, Y.; Walton, K. S. *Langmuir* **2012**, *28*, 16874–80.

(23) Hamon, L.; Serre, C.; Devic, T.; Loiseau, T.; Millange, F.; Férey, G.; De Weireld, G. *J. Am. Chem. Soc.* **2009**, *131*, 8775–7.

(24) Ding, L.; Yazaydin, a. Ö. *J. Phys. Chem. C* **2012**, *116*, 22987–22991.

(25) Bordiga, S.; Regli, L.; Bonino, F.; Groppo, E.; Lamberti, C.; Xiao, B.; Wheatley, P. S.; Morris, R. E.; Zecchina, a *Phys. Chem. Chem. Phys.* **2007**, *9*, 2676–85.

(26) DeCoste, J. B.; Peterson, G. W.; Jasuja, H.; Glover, T. G.; Huang, Y.; Walton, K. S. *J. Mater. Chem. A* **2013**, *1*, 5642.

(27) Jasuja, H.; Walton, K. S. *Dalton Trans.* **2013**, *42*, 15421–6.

(28) Kim, T. K.; Lee, J. H.; Moon, D.; Moon, H. R. *Inorg. Chem.* **2013**, *52*, 589–95.

(29) Hu, Q.; Yu, J.; Liu, M.; Liu, A.; Dou, Z.; Yang, Y. *J. Med. Chem.* **2014**.

(30) Miller, S. R.; Heurtaux, D.; Baati, T.; Horcajada, P.; Grenèche, J.-M.; Serre, C. *Chem. Commun. (Camb).* **2010**, *46*, 4526–8.

(31) Cui, Y.; Chen, B.; Qian, G. *Coord. Chem. Rev.* **2013**, *273-274*, 76–86.

(32) Deng, H.; Grunder, S.; Cordova, K. E.; Valente, C.; Furukawa, H.; Hmadeh, M.; Gandara, F.; Whalley, a. C.; Liu, Z.; Asahina, S.; Kazumori, H.; O'Keeffe, M.; Terasaki, O.; Stoddart, J. F.; Yaghi, O. M. *Science (80-.).* **2012**, *336*, 1018–1023.

(33) Farha, O. K.; Eryazici, I.; Jeong, N. C.; Hauser, B. G.; Wilmer, C. E.; Sarjeant, A. a; Snurr, R. Q.; Nguyen, S. T.; Yazaydın, a Ö.; Hupp, J. T. *J. Am. Chem. Soc.* **2012**, *134*, 15016–21.

(34) Senkovska, I.; Kaskel, S. *Chem. Commun. (Camb).* **2014**, 7089–7098.

(35) Li, J.-R.; Sculley, J.; Zhou, H.-C. *Chem. Rev.* **2012**, *112*, 869–932.

(36) Férey, G.; Serre, C. *Chem. Soc. Rev.* **2009**, *38*, 1380–99.

(37) Otsubo, K.; Wakabayashi, Y.; Ohara, J.; Yamamoto, S.; Matsuzaki, H.; Okamoto, H.; Nitta, K.; Uruga, T.; Kitagawa, H. *Nat. Mater.* **2011**, *10*, 291–5.

(38) Bradshaw, D.; Garai, A.; Huo, J. *Chem. Soc. Rev.* **2012**, *41*, 2344–81.

(39) Bennett, T. D.; Cheetham, A. K. *Acc. Chem. Res.* **2014**, *47*, 1555–62.

(40) Suh, M. P.; Park, H. J.; Prasad, T. K.; Lim, D.-W. *Chem. Rev.* **2012**, *112*, 782–835.

(41) Makal, T. a; Li, J.-R.; Lu, W.; Zhou, H.-C. *Chem. Soc. Rev.* **2012**, *41*, 7761–79.

(42) Mason, J. a.; Veenstra, M.; Long, J. R. *Chem. Sci.* **2014**, *5*, 32.

(43) Ma, S.; Zhou, H.-C. *Chem. Commun. (Camb).* **2010**, *46*, 44–53.

(44) Furukawa, H.; Ko, N.; Go, Y. B.; Aratani, N.; Choi, S. B.; Choi, E.; Yazaydin, a O.; Snurr, R. Q.; O'Keeffe, M.; Kim, J.; Yaghi, O. M. *Science* **2010**, *329*, 424–8.

(45) Mercedes-Benz F125: http://www.emercedesbenz.com/autos/mercedes-benz/concept-vehicles/mercedes-benz-f125-research-vehicle-technology/ (accessed Jul 9, 2014).

(46) Green Car Congress: "BASF Develops Method for Industrial-Scale MOF Synthesis; Trials Underway in Natural Gas Vehicle Tanks": http://www.greencarcongress.com/2010/10/basf-develops-method-for-industrial-scale-mof-synthesis-trials-underway-in-natural-gas-vehicle-tanks.html (accessed Jul 9, 2014).

(47) Quadrelli, R.; Peterson, S. *Energy Policy* **2007**, *35*, 5938–5952.

(48) Pachauri, R. T.; Reisinger, A. *IPCC Fourth Assessment Report: Climate Change 2007*; Geneva, Switzerland, 2007; p. 104.

(49) Haszeldine, R. S. *Science* **2009**, *325*, 1647–52.

(50) Klara, S. M.; Srivastava, R. D. *Environ. Prog.* **2002**, *21*, 247–253.

(51) Sumida, K.; Rogow, D. L.; Mason, J. a; McDonald, T. M.; Bloch, E. D.; Herm, Z. R.; Bae, T.-H.; Long, J. R. *Chem. Rev.* **2012**, *112*, 724–81.

(52) Mason, J. a.; Sumida, K.; Herm, Z. R.; Krishna, R.; Long, J. R. *Energy Environ. Sci.* **2011**, *4*, 3030.

(53) He, Y.; Zhou, W.; Krishna, R.; Chen, B. *Chem. Commun. (Camb).* **2012**, *48*, 11813–31.

(54) Li, J.-R.; Kuppler, R. J.; Zhou, H.-C. *Chem. Soc. Rev.* **2009**, *38*, 1477–504.

(55) Decoste, J. B.; Peterson, G. W. *Chem. Rev.* **2014**, *114*, 5695–5727.

(56) Mulgundmath, V.; Tezel, F. H. *Adsorption* **2010**, *16*, 587–598.

(57) Loiseau, T.; Lecroq, L.; Volkringer, C.; Marrot, J.; Férey, G.; Haouas, M.; Taulelle, F.; Bourrelly, S.; Llewellyn, P. L.; Latroche, M. *J. Am. Chem. Soc.* **2006**, *128*, 10223–30.

(58) Bae, Y.-S.; Farha, O. K.; Hupp, J. T.; Snurr, R. Q. *J. Mater. Chem.* **2009**, *19*, 2131.

(59) Morris, R. E.; Wheatley, P. S. *Angew. Chem. Int. Ed. Engl.* **2008**, *47*, 4966–81.

(60) Valenzano, L.; Civalleri, B.; Chavan, S.; Palomino, G. T.; Areán, C. O.; Bordiga, S. *J. Phys. Chem. C* **2010**, *114*, 11185–11191.

(61) Dietzel, P. D. C.; Johnsen, R. E.; Fjellvåg, H.; Bordiga, S.; Groppo, E.; Chavan, S.; Blom, R. *Chem. Commun. (Camb).* **2008**, *2*, 5125–7.

(62) Wu, H.; Simmons, J. M.; Srinivas, G.; Zhou, W.; Yildirim, T. *J. Phys. Chem. Lett.* **2010**, *1*, 1946–1951.

(63) Queen, W. L.; Brown, C. M.; Britt, D. K.; Zajdel, P.; Hudson, M. R.; Yaghi, O. M. *J. Phys. Chem. C* **2011**, *115*, 24915–24919.

(64) Sumida, K.; Brown, C. M.; Herm, Z. R.; Chavan, S.; Bordiga, S.; Long, J. R. *Chem. Commun. (Camb).* **2011**, *47*, 1157–9.

(65) Hu, Y.; Liu, Z.; Xu, J.; Huang, Y.; Song, Y. *J. Am. Chem. Soc.* **2013**, *135*, 9287–90.

(66) Jiang, Y.; Huang, J.; Kasumaj, B.; Jeschke, G.; Hunger, M.; Mallat, T.; Baiker, A. *J. Am. Chem. Soc.* **2009**, *131*, 2058–9.

(67) Ashbrook, S. E.; Dawson, D. M.; Seymour, V. R. *Phys. Chem. Chem. Phys.* **2014**, *16*, 8223–42.

(68) Koller, H.; Weiss, M. *Top. Curr. Chem.* **2012**, *306*, 189–227.

(69) Bonhomme, C.; Gervais, C.; Laurencin, D. *Prog. Nucl. Magn. Reson. Spectrosc.* **2014**, *77*, 1–48.

(70) Geppi, M.; Borsacchi, S.; Mollica, G.; Veracini, C. A. *Appl. Spectrosc. Rev.* **2008**, *44*, 1–89.

(71) Sutrisno, A.; Huang, Y. *Solid State Nucl. Magn. Reson.* **2013**, *49-50*, 1–11.

(72) Huang, Y.; Xu, J.; Gul-E-Noor, F.; He, P. In *Metal-Organic Framework Materials*; MacGillivray, L. R.; Lukehart, C. M., Eds.; John Wiley & Sons, 2014; pp. 457–470.

(73) Hoffmann, H.; Debowski, M.; Müller, P.; Paasch, S.; Senkovska, I.; Kaskel, S.; Brunner, E. *Materials (Basel).* **2012**, *5*, 2537–2572.

(74) Comotti, A.; Bracco, S.; Sozzani, P.; Horike, S.; Matsuda, R.; Chen, J.; Takata, M.; Kubota, Y.; Kitagawa, S. *J. Am. Chem. Soc.* **2008**, *130*, 13664–72.

(75) Ooms, K. J.; Wasylishen, R. E. *Microporous Mesoporous Mater.* **2007**, *103*, 341–351.

(76) Pawsey, S.; Moudrakovski, I.; Ripmeester, J.; Wang, L.; Exarhos, G. J.; Rowsell, J. L. C.; Yaghi, O. M. *J. Phys. Chem. C* **2007**, *111*, 6060–6067.

(77) Hoffmann, H. C.; Assfour, B.; Epperlein, F.; Klein, N.; Paasch, S.; Senkovska, I.; Kaskel, S.; Seifert, G.; Brunner, E. *J. Am. Chem. Soc.* **2011**, *133*, 8681–90.

(78) Springuel-Huet, M.-A.; Nossov, A.; Adem, Z.; Guenneau, F.; Volkringer, C.; Loiseau, T.; Férey, G.; Gédéon, A. *J. Am. Chem. Soc.* **2010**, *132*, 11599–607.

(79) Horike, S.; Matsuda, R.; Tanaka, D.; Matsubara, S.; Mizuno, M.; Endo, K.; Kitagawa, S. *Angew. Chem. Int. Ed. Engl.* **2006**, *45*, 7226–30.

(80) Gould, S. L.; Tranchemontagne, D.; Yaghi, O. M.; Garcia-Garibay, M. a *J. Am. Chem. Soc.* **2008**, *130*, 3246–7.

(81) Kolokolov, D. I.; Jobic, H.; Stepanov, A. G.; Guillerm, V.; Devic, T.; Serre, C.; Férey, G. *Angew. Chem. Int. Ed. Engl.* **2010**, *49*, 4791–4.

(82) Mowat, J. P. S.; Miller, S. R.; Griffin, J. M.; Seymour, V. R.; Ashbrook, S. E.; Thompson, S. P.; Fairen-Jimenez, D.; Banu, A.-M.; Düren, T.; Wright, P. a *Inorg. Chem.* **2011**, *50*, 10844–58.

(83) Vukotic, V. N.; Harris, K. J.; Zhu, K.; Schurko, R. W.; Loeb, S. J. *Nat. Chem.* **2012**, *4*, 456–60.

(84) Uemura, T.; Kitagawa, K.; Horike, S.; Kawamura, T.; Kitagawa, S.; Mizuno, M.; Endo, K. *Chem. Commun. (Camb).* **2005**, 5968–70.

(85) Morris, W.; Stevens, C. J.; Taylor, R. E.; Dybowski, C.; Yaghi, O. M.; Garcia-Garibay, M. A. *J. Phys. Chem. C* **2012**, *116*, 13307–13312.

(86) Loiseau, T.; Serre, C.; Huguenard, C.; Fink, G.; Taulelle, F.; Henry, M.; Bataille, T.; Férey, G. *Chemistry* **2004**, *10*, 1373–82.

(87) Morris, W.; Taylor, R. E.; Dybowski, C.; Yaghi, O. M.; Garcia-Garibay, M. a. *J. Mol. Struct.* **2011**, *1004*, 94–101.

(88) Devautour-Vinot, S.; Maurin, G.; Serre, C.; Horcajada, P.; Paula da Cunha, D.; Guillerm, V.; de Souza Costa, E.; Taulelle, F.; Martineau, C. *Chem. Mater.* **2012**, *24*, 2168–2177.

(89) Rossini, A. J.; Zagdoun, A.; Lelli, M.; Canivet, J.; Aguado, S.; Ouari, O.; Tordo, P.; Rosay, M.; Maas, W. E.; Copéret, C.; Farrusseng, D.; Emsley, L.; Lesage, A. *Angew. Chem. Int. Ed. Engl.* **2012**, *51*, 123–7.

(90) Jiang, Y.; Huang, J.; Marx, S.; Kleist, W.; Hunger, M.; Baiker, A. *J. Phys. Chem. Lett.* **2010**, *1*, 2886–2890.

(91) Haouas, M.; Volkringer, C.; Loiseau, T.; Férey, G.; Taulelle, F. *Chemistry* **2009**, *15*, 3139–46.

(92) Horcajada, P.; Serre, C.; Maurin, G.; Ramsahye, N. a; Balas, F.; Vallet-Regí, M.; Sebban, M.; Taulelle, F.; Férey, G. *J. Am. Chem. Soc.* **2008**, *130*, 6774–80.

(93) Stallmach, F.; Gröger, S.; Künzel, V.; Kärger, J.; Yaghi, O. M.; Hesse, M.; Müller, U. *Angew. Chem. Int. Ed. Engl.* **2006**, *45*, 2123–6.

(94) Kong, X.; Scott, E.; Ding, W.; Mason, J. a; Long, J. R.; Reimer, J. a *J. Am. Chem. Soc.* **2012**, *134*, 14341–4.

(95) Lin, L.-C.; Kim, J.; Kong, X.; Scott, E.; McDonald, T. M.; Long, J. R.; Reimer, J. a.; Smit, B. *Angew. Chemie Int. Ed.* **2013**, *52*, 4410–4413.

(96) He, P.; Xu, J.; Terskikh, V. V; Sutrisno, A.; Nie, H.; Huang, Y. *J. Phys. Chem. C* **2013**, 130619124804007.

(97) Lieder, C.; Opelt, S.; Dyballa, M.; Henning, H.; Klemm, E.; Hunger, M. *J. Phys. Chem. C* **2010**, *114*, 16596–16602.

(98) Volkringer, C.; Loiseau, T.; Férey, G.; Morais, C. M.; Taulelle, F.; Montouillout, V.; Massiot, D. *Microporous Mesoporous Mater.* **2007**, *105*, 111–117.

(99) Hajjar, R.; Volkringer, C.; Loiseau, T.; Guillou, N.; Marrot, J.; Férey, G.; Margiolaki, I.; Fink, G.; Morais, C.; Taulelle, F. *Chem. Mater.* **2011**, *23*, 39–47.

(100) Mowat, J. P. S.; Miller, S. R.; Slawin, A. M. Z.; Seymour, V. R.; Ashbrook, S. E.; Wright, P. a. *Microporous Mesoporous Mater.* **2011**, *142*, 322–333.

(101) Sutrisno, A.; Terskikh, V. V; Shi, Q.; Song, Z.; Dong, J.; Ding, S. Y.; Wang, W.; Provost, B. R.; Daff, T. D.; Woo, T. K.; Huang, Y. *Chemistry* **2012**, *18*, 12251–9.

(102) Xu, J.; Terskikh, V. V; Huang, Y. *Chemistry* **2013**, *19*, 4432–6.

(103) Xu, J.; Terskikh, V. V.; Huang, Y. *J. Phys. Chem. Lett.* **2013**, *4*, 7–11.

(104) Taulelle, F.; Bouchevreau, B.; Martineau, C. *CrystEngComm* **2013**, *15*, 8613.

(105) Harris, R. K.; Wasylishen, R. E.; Duer, M. J. *NMR Crystallography*; 1st ed.; Wiley, 2009; p. 520.

(106) *National Research Council. The Physics of Materials: How Science Improves Our Lives*; Washington, DC: The National Academies Press, 1997.

(107) Eberhart, M. E.; Clougherty, D. P. *Nat. Mater.* **2004**, *3*, 659–61.

(108) Yang, Q.; Liu, D.; Zhong, C.; Li, J.-R. *Chem. Rev.* **2013**, *113*, 8261–323.

(109) Liu, B.; Smit, B. *J. Phys. Chem. C* **2010**, *114*, 8515–8522.

(110) Zheng, B.; Yang, Z.; Bai, J.; Li, Y.; Li, S. *Chem. Commun. (Camb).* **2012**, *48*, 7025–7.

(111) Wu, H.; Yildirim, T.; Zhou, W. *J. Phys. Chem. Lett.* **2013**, *4*, 925–930.

(112) Wilmer, C. E.; Leaf, M.; Lee, C. Y.; Farha, O. K.; Hauser, B. G.; Hupp, J. T.; Snurr, R. Q. *Nat. Chem.* **2012**, *4*, 83–9.

(113) Haldoupis, E.; Nair, S.; Sholl, D. S. *J. Am. Chem. Soc.* **2012**, *134*, 4313–23.

(114) Skoulidas, A. I.; Sholl, D. S. *J. Phys. Chem. B* **2005**, *109*, 15760–8.

(115) Canepa, P.; Nijem, N.; Chabal, Y. J.; Thonhauser, T. *Phys. Rev. Lett.* **2013**, *110*, 026102.

(116) Zhang, Z.; Liu, J.; Li, Z.; Li, J. *Dalton Trans.* **2012**, *41*, 4232–8.

(117) Battisti, A.; Taioli, S.; Garberoglio, G. *Microporous Mesoporous Mater.* **2011**, *143*, 46–53.

(118) Gurdal, Y.; Keskin, S. *Ind. Eng. Chem. Res.* **2012**, *51*, 7373–7382.

(119) Vaidhyanathan, R.; Iremonger, S. S.; Shimizu, G. K. H.; Boyd, P. G.; Alavi, S.; Woo, T. K. *Science* **2010**, *330*, 650–3.

(120) Düren, T.; Bae, Y.-S.; Snurr, R. Q. *Chem. Soc. Rev.* **2009**, *38*, 1237–47.

(121) Sarkisov, L.; Düren, T.; Snurr, R. Q. *Mol. Phys.* **2004**, *102*, 211–221.

(122) Volkringer, C.; Meddouri, M.; Loiseau, T.; Guillou, N.; Marrot, J.; Férey, G.; Haouas, M.; Taulelle, F.; Audebrand, N.; Latroche, M. *Inorg. Chem.* **2008**, *47*, 11892–901.

(123) Foo, M. L.; Horike, S.; Inubushi, Y.; Kitagawa, S. *Angew. Chem. Int. Ed. Engl.* **2012**, *51*, 6107–11.

2 – Methods

In this chapter, all major components involved in the calculation of gas adsorption isotherms and other simulation data in MOFs shall be highlighted, and the underlying theory shall be reviewed. All methods presented in this chapter are used throughout this thesis, in both projects presented in Chapter 3 and 4. This chapter does not contain an exhaustive list of all methods and theory used, as certain methods which are specifically used in for work in Chapter 3 or Chapter 4 shall be presented in detail in those chapters.

2.1 Fully Automated Adsorption Analysis in Porous Solids (FA^3PS)

FA^3PS is a software package designed and developed by the Woo group to streamline, automate and facilitate the process necessary for calculation of an uptake isotherm and other molecular-level data in nanoporous materials. Several steps are required to compute gas uptake isotherms and other gas sorption properties, and each step requires specialized input and instructions to run a calculation. Although each MOF is different, members of this class of materials share many similarities (ie. porosity, pore apertures below certain size thresholds, organic and inorganic components, etc.). Because of this, many simulation parameters can be set to in-house determined 'MOF default' parameters. A future goal of this software is to make gas adsorption calculations accessible to people completely unfamiliar with computational materials methods, as it intends to greatly simplify running basic calculations. A schematic for the FA^3PS code is provided below in Figure 2-1, and each step shall be highlighted in sequential order in the following sections. The underlying theory for these methods shall also briefly be addressed.

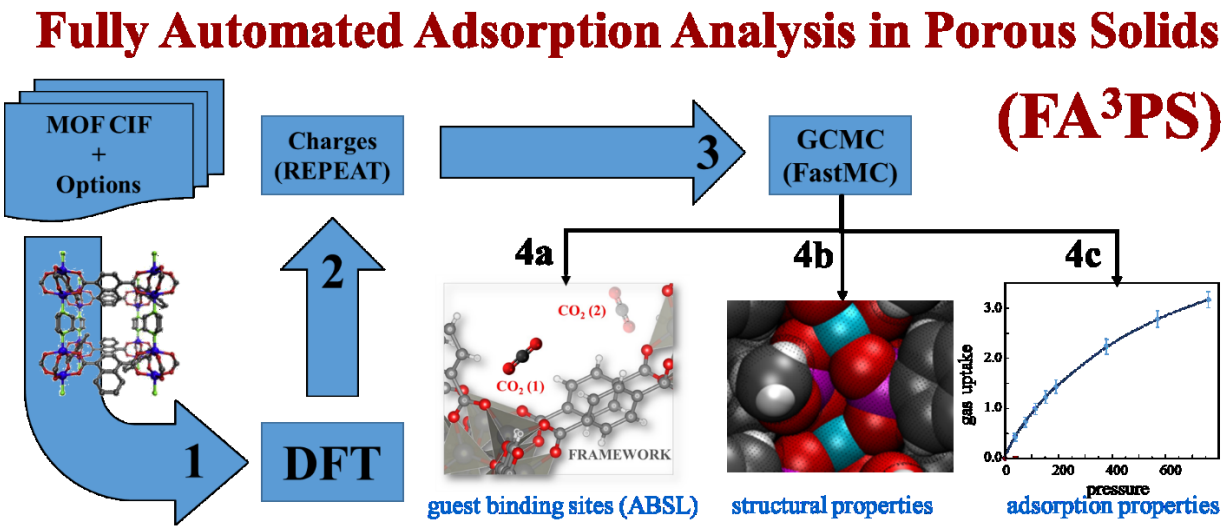

Figure 2-1. *FA³PS Schematic*

2.1.1 Periodic Density Functional Theory (DFT)

DFT is a quantum mechanical (QM) method which is very popular in chemistry, and has made many important contributions to the area in the 30 or so years since its popularization.[1] With recent advances in computing resources and development of DFT implementation accuracy, simulations of several hundreds of atoms are now possible. DFT's novelty compared to wave function methods is that the total electron density is used to calculate the total energy and to describe the complicated interactions between the electrons.[2] In competing QM methods, such as Hartree-Fock or more expensive correlated methods, the electron-electron interactions are calculated by brute force from a complicated many-body wave function that grows in dimensionality as the system size increases and the number of electrons increase. In DFT, the dimensionality of the total electronic density function does not increase with system size and apriori knowledge of how the electrons interact with one another based on the electron density is used, resulting in DFT typically offering significant compute time savings compared to wave function based methods. In modern DFT methods, there are many ways to evaluate the energy from the electron density, or different

approaches to express the energy as a functional of the electron density. There is now quite a proliferation of so-called DFT exchange-correlation functionals, with many of the popular ones used in chemical research being parameterized to experimental results. The so-called B3LYP DFT method, which incorporates a fraction of Hartree-Fock exchange energy into the calculation is by far the most popular functional used in the chemistry community as it offers a very favourable accuracy/cost balance for many organic and inorganic systems.[3–6]

DFT has not only proven its worth for molecular systems, but it has also provided valuable insight in solid state chemistry and physics. In fact, DFT has been widely recognized and accepted by the solid-state physics community for a longer time than by the quantum chemistry community.[6,7] A major difference in the DFT calculations used to study solids compared to those used to study molecules, is the nature of the basis sets used to expand the orbitals and electron density. For molecular systems, atom-centered basis functions are used, such as the popular Gaussian basis sets developed by Pople (i.e. 6-311G(d,p)). In the solid state DFT calculations, delocalized and periodic plane wave basis functions are typically used. These require the use of pseudopotentials, also called effective core potentials (ECPs) which are functions which treat core electrons (the core electrons do not generally participate in important chemical or physical interactions in solids, and using pseudopotentials instead of plane waves for their description significantly reduces computational cost). Additionally, it would be costly and near impossible to analyze infinite materials using DFT; therefore, the translational symmetry of these systems is exploited via periodic boundary conditions to simplify calculations.

The use of periodic DFT as the first step of a FA^{3}PS calculation serves two different purposes. First and foremost, it is a method used to compute the electrostatic potential (ESP),

which is needed for the REPEAT atomic charge calculation (see section 1.1.2 for further details regarding the ESP and this method). The second objective is to refine the positions of the H atoms included as a part of the framework structure, as well as to relax other framework atoms if necessary. This is because light H atoms are generally not observed with X-ray crystallography, the most common method for characterizing the detailed structure of MOFs. Often the crystallographic information files (CIF) provided for MOF structures do not contain H atom positions at all, and their positions must therefore be inferred based on a combination of chemical intuition and information provided in the article in which X-ray structure data was published. With respect to relaxing framework atoms, this is often necessary when the CIF presents crystallographic disorder: that is, when a same atom or group of atoms has several possible positions within the structure. For all work carried out in this thesis, MOF frameworks are kept rigid for gas adsorption to reduce computational costs (this is shown to be a reasonable approximation for many MOFs).[8] To insure a correctly relaxed, rigid framework for adsorption calculations, a favoured configuration is first selected based on occupancy in order to resolve the disorder, then only those positions which were selected are DFT-optimized to insure lowest framework energy. In certain cases where several different disorder-related configurations are equally favourable, all configurations are tested to identify the lowest energy one, and further gas adsorption studies are sometimes carried out on all relaxed structures to verify differences in binding locations and quantitative uptake results.

The Vienna Ab Initio Software Package (VASP)[9–12] as well as the Spanish Initiative for Electronic Simulations with Thousands of Atoms (SIESTA)[13] are two of the periodic DFT implementations included in the FA^{3}PS package, both of which were used for the work

carried out in this thesis. For all work in VASP, the PBE exchange-correlation functional and the default projector augmented wave (PAW) pseudopotentials/projectors were used.[14,15] For SIESTA, the PBE exchange-correlation functional was also used alongside double zeta polarized basis sets, for which parameters were tuned to give the same accuracy as VASP. In terms of the difference between VASP and SIESTA, it was stated earlier in this section that plane wave basis sets are used for DFT calculations in the solid-state (VASP), however localized atom-centered basis sets can also be used for solid-state calculations (SIESTA). Comparable calculations using SIESTA are faster than those run in VASP, which can be especially useful if a MOF's is very large and has a large unit cell. On the other hand, accurate pseudopotentials are available for nearly all elements of the periodic table in VASP, while the pseudopotentials in Siesta are quite limited, and less accurate. Plane wave basis sets are also free of the basis set superposition errors which occur when using localized atomic basis sets. For these reasons, the VASP code was used whenever possible for this thesis.

2.1.2 REPEAT Charge Calculation

The second step FA^{3}PS takes towards calculating a gas adsorption isotherm is the calculation of atomic charges. REPEAT, the Repeating Electrostatic Potential Extracted Atomic charge method, was developed by the Woo group in 2009.[16] This method derives charges for each atom in the solid based on a DFT-derived ESP grid located outside the Van der Waals radii-spheres centered on each atomic site. The electrostatic potential (ESP) is defined as the energy required to bring a unit charge from an infinite distance away from a point r. The REPEAT method was an important advance in derivation of atomic charges for periodic materials, as no one had ever before derived charges from the ESP of a periodic

DFT calculation citing the difficulty in defining the reference state for the ESP in an infinite periodic system.[17] Many researchers have successfully used REPEAT to predict adsorption properties and other physical properties for periodic materials, especially MOFs.[18–22] Indeed, Watanabe *et al.* compared many different charge calculation methods to calculate thermodynamic properties of the MOF ZIF-8, and REPEAT showed the best agreement with experimental data.[23]

2.1.3 GCMC

Once hydrogen atom positions have been determined, framework atoms have been relaxed (if necessary) and atomic charges have been computed, the gas adsorption isotherm can be simulated using a grand canonical Monte Carlo (GCMC) simulation. The "grand canonical" portion of GCMC references the name of the statistical thermodynamic ensemble which one utilizes in the simulation. An ensemble is a collection of a large number of replicas of a system of interest, for example a collection of porous MOF unit cells containing adsorbed gas. In this ensemble, the chemical potential (μ), temperature (T) and the system volume (V) are kept constant. (The chemical potential is a fundamental thermodynamic property of a system, which shows how potential energy changes as a function of the number of particles in a given system.) In a GCMC simulation the number of particles (N) may change, meaning that the number of guests within a host can increase or decrease. Final simulation results which make use of the grand canonical ensemble will display thermal and chemical equilibrium because thermodynamic variables T and μ are held constant.

As for the "Monte Carlo" portion of grand canonical Monte Carlo (GCMC), it makes reference to the propensity for visitors in Monte Carlo, Monaco to gamble. Most forms of gambling are both random and repetitive activities, and this is at the very core of the Monte

Carlo method. Monte Carlo methods have been applied to problems in mathematics, finances, physics, biology, chemistry and even as a means for artificial intelligence to beat world champions at games like chess.[24–27]

In Monte Carlo methods applied to chemical problems, a randomly selected atom or guest molecule is first perturbed in some way through different move types including rotation, translation or conformation change. Once the newly perturbed configuration is created, the potential energy of the entire system is calculated. Three possible scenarios may occur at this point: the potential energy of the new configuration can be lower, slightly higher or significantly higher than that of the configuration prior to the perturbation. If the energy of the new configuration is lower than that of the prior configuration, the configuration is automatically "accepted" and added to the ensemble average. (An ensemble average is the mean of a quantity, such as potential energy in this case, over all configurations accepted in the simulation.) If the energy of the new configuration is slightly higher than that of the previous configuration, it has a chance of being accepted based on Boltzmann-type weighting criteria, which enables sampling to hop over potential energy barriers. Finally, if the potential energy of the new system configuration is much higher than that of the prior configuration, then the new configuration will usually be "rejected", and the prior configuration will be re-added to the ensemble average. In this scenario, it is important for the prior configuration energy to be added to the ensemble average because a more heavily favoured configuration needs to be sampled more. It should be noted that even high energy configurations have a small, non-zero probability of being accepted and added to the ensemble average due to the Boltzmann-type weighting. The process of producing a perturbed configuration, evaluating its potential energy and adding it to the ensemble

average is repeated until the ensemble average has converged, where it is assumed that the macroscopic properties which depend on microstates will also be converged.

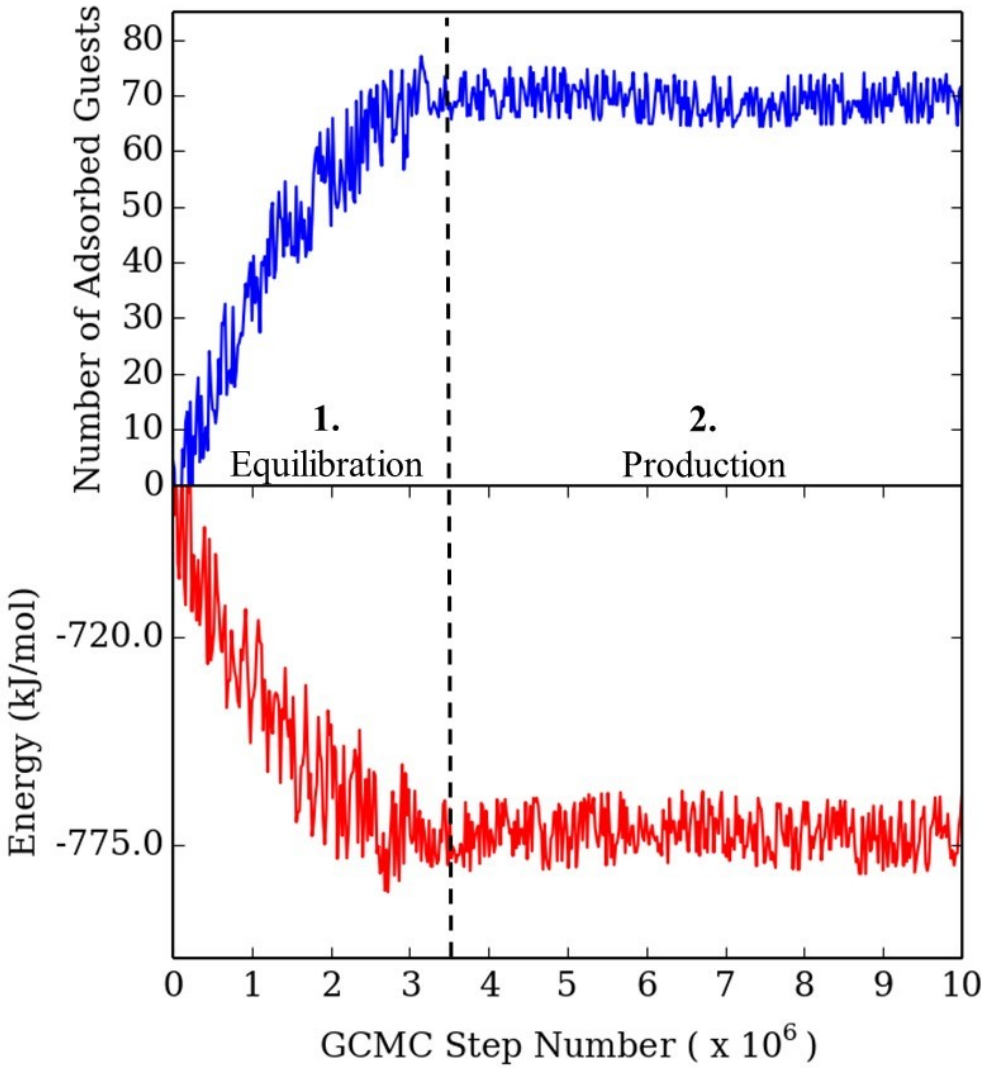

Figure 2-2. *Plots of the number of adsorbed guests in a MOF (top) and total energy (bottom) throughout the course of a GCMC simulation. Equilibration and production phases are indicated on both plots.*

When coupling the grand canonical ensemble with Monte Carlo, one has two additional perturbations that can be performed on the system to generate new configurations: particle insertion and deletion. In this way, inserted guest molecules which interact favourably with the host will produce a lower potential energy configuration, and have a higher chance of being accepted and used as the starting point for next configurations. This highlights one

major difference between GCMC and MC: in a pure MC scheme, acceptance of new configurations is based solely on potential energy, whereas for GCMC it is based on both potential energy and chemical potential (μ). This is why a lower energy configuration is not immediately added to the ensemble average in GCMC. Figure 2-2 above shows a typical plot for the change in the number of guests and the potential energy changes as a function of the number of GCMC steps taken. The two stages which are typical of GCMC adsorption are indicated on the figure: equilibration (1) and production (2). In the equilibration phase, it is more favourable for guest to be adsorbed than deleted, so a sharp increase in guest is noted, as seen until around 3.5 million GCMC steps in Figure 2-2. After many guest insertions are accepted, the MOF pores become more saturated with adsorbate and it is no longer as favourable to add guest to the pore. The rate of insertions becomes equal to that of deletions, as can be seen in Figure 2-2, when the number of guests fluctuates around an average value. This indicates that equilibrium has been reached. Once equilibrium is reached, the chemical potential of adsorbed molecules (μ_{ads}) is equal to that of gaseous molecules ($\mu_{gaseous}$). This is a key conceptual idea of GCMC: since $\mu_{gaseous}$ is known for ideal gases, μ_{ads} is also known at equilibrium, and the expression for ideal gas can be used in the acceptance probability for GCMC simulations. This is why equilibrium phase data from GCMC can be used for calculation of adsorption equilibrium properties such as gas uptake isotherms, heats of adsorption, guest probability density, etc. Because of its ability to efficiently produce equilibrium adsorption properties and relative simplicity, GCMC forms a powerful procedure which has been pivotal in the study of gas adsorption in MOFs to date.[8]

Our group maintains its own GCMC implementation, denoted FastMC. It can also be easily modified to work for other Monte Carlo ensembles, such as the canonical Monte Carlo

ensemble (which has constant number of particles (N), system volume (V) and temperature (T)). As a side-note, canonical Monte Carlo in particular is useful for simulations in which the number of guest molecules is known and does not change, such as might occur in a material containing trapped solvent molecules for example. After a GCMC simulation is completed in FA^{3}PS, final post-processing scripts generate the desired output, notably gas uptake isotherm plots as well as guest probability density plots within the framework. Here, it is useful to introduce the idea of isosurfaces and isovalues. An isosurface is a 3-dimensional contour plot representing points of a constant value, and produces a representation of the probability density. For our simulations, this representation shows the probability per Å^3 associated with a guest being in a certain region of accessible MOF pore volume over the course of the simulation (see Figure 2-3 in section 2.2 for the appearance of a typical probability density plot for CO_2 adsorbed in a MOF). In an isosurface plot, all points that make up the surface have the same value of the function. In this case, the higher the so-called isovalue, the higher the probability of finding the guest molecule. Given that the isosurface values represent probability in this work, they will always be between 0 (low probability) and 1 (high probability). High probability areas indicate probable binding sites. Our group maintains a post-processing package which automatically identifies binding sites from this probability density. Its general functionality will be highlighted in the next section.

2.2 Automatic Binding Site Locator (ABSL)

In addition to providing gas adsorption isotherms, GCMC simulations allow us to identify binding sites of guest molecules inside the MOF based on the probability distributions that are generated from the simulations. ABSL (Automatic Binding Site Locator) is another algorithm developed by the Woo group that is able to automatically

locate the binding sites from the probability distributions. This code interfaces with FA^3PS and is intended to be run following a GCMC calculation.

Although they may be disperse in some materials, the binding sites are generally well localized in most guest/MOF combinations due to electrostatic and dispersion interactions between the guest and the metal ions, functional groups or specific organic groups of the MOF. Finding these binding sites normally requires careful manual inspection of GCMC-derived probability density distributions. This is a time-consuming and tedious process in most cases. ABSL is a robust algorithm which identifies the binding sites automatically from the noisy probability distributions using Gaussian filters to smooth the data. Figure 2-3 shows what a typical, "noisy" probability density plot looks like, and the resulting, Gaussian-smoothed binding sites as identified by ABSL. ABSL also includes functionality for deriving the binding energy of each binding site. The binding site energy is also separated into its electrostatic and van der Waals components, providing further information to analyze the nature of the binding.

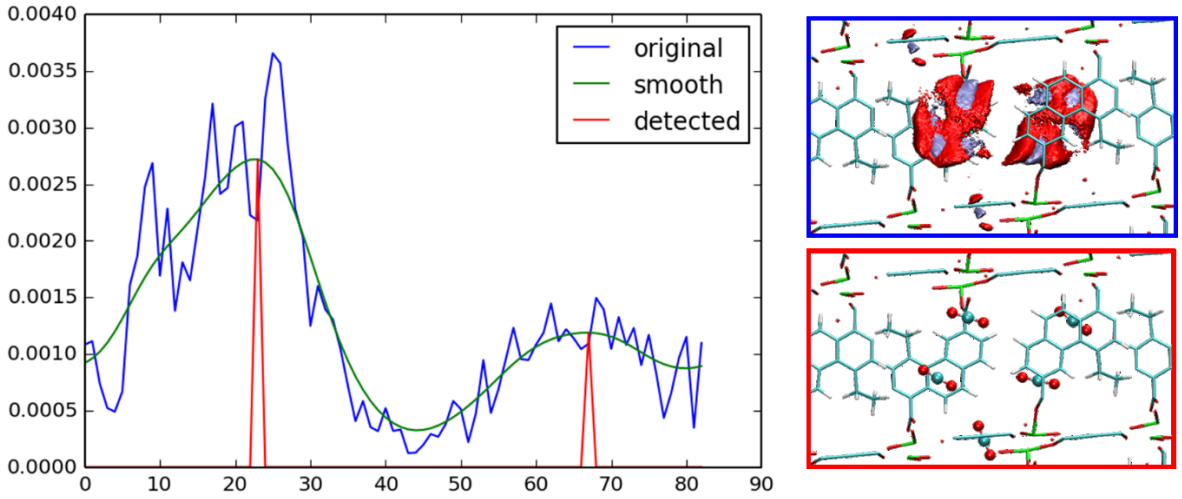

Figure 2-3. *Overview of ABSL function and results. On the left, a probability distribution of CO2 in a MOF is plotted (y = probability of finding guest, x = angular distribution) with the original signal (blue), Gaussian smoothed signal (green) and finally ABSL-detected peaks (red). The image on the top right shows the original CO2 probability density (red = Oxygen atom probability, Grey = Carbon atom probability) which corresponds to the original unsmoothed signal as represented by the blue curve in the graphical plot. On the lower-right is the final, ABSL-detected distribution of CO_2 within the MOF, where distinct CO_2 guests are seen instead of density distributions (red = Oxygen, blue = Carbon).*

2.3 References

(1) Koch, W.; Holthausen, M. C. *A Chemist's Guide to Density Functional Theory*; 2nd ed.; Wiley, 2001; Vol. 3, p. 293.

(2) Dronskowski, R. *Computational Chemistry of Solid State Materials*; 1st ed.; Wiley, 2007; pp. 46–54, 95–101, 117–124.

(3) Tirado-Rives, J.; Jorgensen, W. L. *J. Chem. Theory Comput.* **2008**, *4*, 297–306.

(4) Becke, A. D. *J. Chem. Phys.* **1993**, *98*, 5648.

(5) Lee, C.; Yang, W.; Parr, R. G. *Phys. Rev. B* **1988**, *37*, 785–789.

(6) Cohen, A. J.; Mori-Sánchez, P.; Yang, W. *Chem. Rev.* **2012**, *112*, 289–320.

(7) Dronskowski, R. *Computational Chemistry of Solid State Materials*; 1st ed.; Wiley, 2007; pp. 7–8.

(8) Düren, T.; Bae, Y.-S.; Snurr, R. Q. *Chem. Soc. Rev.* **2009**, *38*, 1237–47.

(9) Kresse, G.; Hafner, J. *Phys. Rev. B* **1993**, *47*, 558–561.

(10) Kresse, G.; Hafner, J. *Phys. Rev. B* **1994**, *49*, 14251–14269.

(11) Kresse, G. *Phys. Rev. B* **1996**, *54*, 11169–11186.

(12) Kresse, G.; Furthmüller, J. *Comput. Mater. Sci.* **1996**, *6*, 15–50.

(13) Soler, J. M.; Artacho, E.; Gale, J. D.; García, A.; Junquera, J.; Ordejón, P.; Sánchez-Portal, D. *J. Phys. Condens. Matter* **2002**, *14*, 2745–2779.

(14) Blöchl, P. E. *Phys. Rev. B* **1994**, *50*, 17953–17979.

(15) Perdew, J. P.; Burke, K.; Ernzerhof, M. *Phys. Rev. Lett.* **1996**, *77*, 3865–3868.

(16) Campañá, C.; Mussard, B.; Woo, T. K. *J. Chem. Theory Comput.* **2009**, *5*, 2866–2878.

(17) Martin, R. M. *Electronic Structure: Basic Theory and Practical Methods*; Cambridge University Press: Cambridge, UK, 2004; pp. 499–502.

(18) Sutrisno, A.; Terskikh, V. V; Shi, Q.; Song, Z.; Dong, J.; Ding, S. Y.; Wang, W.; Provost, B. R.; Daff, T. D.; Woo, T. K.; Huang, Y. *Chemistry* **2012**, *18*, 12251–9.

(19) Morris, W.; He, N.; Ray, K. G.; Klonowski, P.; Furukawa, H.; Daniels, I. N.; Houndonougbo, Y. A.; Asta, M.; Yaghi, O. M.; Laird, B. B. *J. Phys. Chem. C* **2012**, *116*, 24084–24090.

(20) Burtch, N. C.; Jasuja, H.; Dubbeldam, D.; Walton, K. S. *J. Am. Chem. Soc.* **2013**, *135*, 7172–80.

(21) Vaidhyanathan, R.; Iremonger, S. S.; Shimizu, G. K. H.; Boyd, P. G.; Alavi, S.; Woo, T. K. *Science* **2010**, *330*, 650–3.

(22) Iremonger, S. S.; Liang, J.; Vaidhyanathan, R.; Martens, I.; Shimizu, G. K. H.; Daff, T. D.; Aghaji, M. Z.; Yeganegi, S.; Woo, T. K. *J. Am. Chem. Soc.* **2011**, *133*, 20048–51.

(23) Watanabe, T.; Manz, T. a.; Sholl, D. S. *J. Phys. Chem. C* **2011**, *115*, 4824–4836.

(24) Silver, D.; Veness, J. In *24th Advances in Neural Information Processing Systems*; Lafferty, J., Ed.; Neural Information Processing Systems (NIPS): Vancouver, British Columbia, 2010; pp. 2164–2172.

(25) James, F. *Reports Prog. Phys.* **1980**, *43*, 1145–1189.

(26) Binder, K. *Reports Prog. Phys.* **1997**, *60*, 487–559.

(27) Bouzida, D.; Kumar, S.; Swendsen, R. *Phys. Rev. A* **1992**, *45*, 8894–8901.

3 – Parameterization of N_2 TraPPE Model for Improved Simulated CO_2/N_2 and O_2/N_2 Selectivity Predictions in Metal Organic Frameworks

In this chapter, a parameterized N_2 force field fit simultaneously to 28 experimental isotherms for high accuracy uptake isotherms in the pressure and temperature ranges relevant to CO_2/N_2 and O_2/N_2 gas separation is presented. This model, called NIMF (Nitrogen In MoFs), addresses issues we identify with the N_2 TraPPE force field, in common use for generating simulated uptake isotherms in MOFs. We fit the NIMF force field parameters in conjunction with the UFF and ESP-derived charges to calculate electrostatic interactions for framework atoms, as the combination of UFF and ESP-derived charges is the most common strategy employed for MOF simulations.[1] NIMF enables better predictions of N_2 uptake in a wide range of MOFs, and by extension improves the accuracy of CO_2/N_2 and O_2/N_2 adsorption selectivity predictions. The work presented in this chapter has been submitted for publication in *Langmuir*.

3.1 Introduction

Due to record-breaking selectivities, uptakes and relatively low cost, MOFs are being actively developed as solid sorbants for industrial carbon capture applications using temperature and pressure swing adsorption systems.[2] For example, one MOF reported by Bae *et al*., $Zn_2(bttb)(CF_3\text{-}py)_2$, was found to have flue gas CO_2/N_2 selectivity considerably higher (30-37) than that of the best commercial zeolites (19) and activated carbons (15).[3] Since post-combustion flue streams are 73-77% N_2 and 15-16% CO_2, high CO_2/N_2 selectivity is an important property for carbon capture because adsorption of other gases will both reduce the MOF's CO_2 capacity and will result in a lower purity CO_2 stream. The purity

of the post capture CO_2 stream is important since it costs more energy to compress, transport, and store impure gases. Nitrogen adsorption selectivity is also important in other clean energy applications. For example, in oxy-fuel combustion[4], fuel is burned in pure oxygen which generates a post-combustion flue stream which, following condensation of water, is primarily composed of CO_2 which can then be prepared for storage. In oxy-fuel systems, the gas separation occurs before the combustion where oxygen is removed from air to provide pure oxygen. Thus high O_2/N_2 selectivities are required, and MOFs have also shown promise for separating O_2 from N_2. For example, the MOF $Cr_3(BTC)_2$ exhibits an O_2/N_2 selectivity of 22 that is significantly higher than for many other porous sorbents.[5] At present, expensive cryogenic air separation units are used to supply high purity oxygen for coal combustion, and their use accounts for most of the elevated cost of the oxy-fuel combustion process.[6] Because of their great potential in separating O_2 from N_2, MOFs could provide greater efficiency and lower costs than current oxy-fuel combustion solutions.

Molecular simulation and specifically grand canonical Monte Carlo calculations have been successful in quantitatively reproducing experimental adsorption data in MOFs as well as providing atomistic-level information not easily obtained through experimental means.[1,7] In order to reproduce experiment correctly, however, it is critical to select appropriate simulation parameters. For gas adsorption in MOFs, the force fields which are used to reproduce non-bonding interactions between guest molecules and framework atoms are of particular importance, as they dictate gas uptake and binding locations within the framework. Generalized force fields such as the Universal Force Field (UFF)[8] aim to reproduce a wide variety of interactions for most of the periodic elements. More specialized force fields exist for certain gases, for which parameters are typically set to reproduce certain

specific physical properties of the bulk gas. For example, the CO_2 and N_2 TraPPE force fields are fit to reproduce liquid-vapour equilibria.[9] These force fields, which are fit to bulk properties of the molecule, are not always appropriate for use in adsorption, as gas properties will change once adsorbed. In the context of MOFs, the CO_2 force field used for simulating gas adsorption created by Calero *et al.*[10] has been shown to accurately predict CO_2 uptake in MOFs.[11–13] However, N_2 TraPPE[9], a force field commonly used to simulate adsorption in MOFs, over-predicts N_2 uptake consistently in a series of UiO-66 MOF derivatives. This occurs in spite of the DREIDING force field, which was used to define the potential parameters for framework atoms, being rescaled specifically to improve uptake accuracy for a variety of gases.[14] Use of N_2 TraPPE for adsorption in MOFs can be problematic, as evidenced by other simulated N_2 uptake isotherms not matching experimental uptake results when N_2 TraPPE is used (see section 3.3 for further evidence of this).[15–17] For cases in which simulated gas uptake isotherms do not match experimental data, parameterization of the existing force field, for example, training it to reproduce experimental or high accuracy computational adsorption data, can be employed. In fact, adjustment of existing gas force field parameters for adsorption on porous materials is a procedure which has successfully been employed to improve accuracy of simulation in other sorbents[10] as well as MOFs.[18–20]

In this work, we present a three-site N_2 model fit simultaneously to 28 experimental isotherms for high accuracy uptake isotherms in the pressure and temperature ranges relevant to CO_2/N_2 and O_2/N_2 gas separation, henceforth called the NIMF (Nitrogen In MoFs) model. This model aims to address the systematic overestimation of N_2 uptake obtained with the N_2 TraPPE model, which is in common use for generating simulated adsorption isotherms. The NIMF model is conceived for use in conjunction with UFF[8] Lennard-Jones parameters and

ab initio derived electrostatic potential fitted partial atomic charges for the framework atoms, as this combination is most commonly employed for MOF simulations.[1] NIMF enables better predictions of N_2 uptake in a wide range of MOFs, and by extension will improve the accuracy of CO_2/N_2 and O_2/N_2 adsorption selectivity predictions.

3.2 Theory

3.2.1 Force Fields

In Quantum mechanics (QM), various strategies are employed to solve the Schrödinger equation, thereby providing a full description of the chemical system (see Chapter 1 for a more in depth overview of QM's underlying theory). High-level QM calculations are accurate at the expense of efficiency. Because of their elevated costs, only systems containing hundreds of atoms can be analyzed using high-level QM methods. Many chemical problems, for example enzyme chemistry, surface adsorption and polymer growth require treatment of thousands or even millions of atoms for a proper description of the chemistry at play. For many years, Molecular Mechanics (MM) or force field methods have been regularly applied to these large systems. The improved efficiency afforded by MM techniques is a result of opting not to solve the Schrödinger equation explicitly. Instead, parameters which have been fit to experimental data and/or high level computational data are used to describe the system. Another result which stems from not solving the Schrödinger equation is that the atom is the basic unit used for description of MM systems, in sharp contrast to QM systems in which electrons serve as the fundamental unit. The MM atom-based approach relies on the assumption that structurally similar units in different molecules tend to be similar. An example of this would be to assume that an sp^3 hybridized carbon should have approximately the same connecting bond lengths and angles in two different

organic compounds. An sp^3 carbon is an example of an atom *type* which might be included in a force field, the container of all parameters and potential forms necessary for MM simulations. The atom type identity will depend on the atom's periodic element as well as what the atom is bonded to. An important consequence of this is that bonding information must be provided explicitly to make use of MM methods, unlike in QM methods where bonding is determined from the calculation itself. Inclusion of atom typing based on connectivity justifies the CHARMM (Chemistry at HARvard Macromolecular Mechanics) force field having over 20 different carbon atom types.[21] Parameters for each atom type in a force field will include both bonded terms (bond stretching, angle bending, rotational torsion) and non-bonded terms (van der Waals and electrostatic interactions) to describe interactions between different atom types. The force field energy is a sum of the contributions from each of these different components. [22]

An enormous variety of force fields exist today. Some aim to serve as general force fields which work for most chemical systems (UFF[8] and DREIDING[23] are examples) or a subset of chemical systems (MM3 for hydrocarbons[24] or CHARMM for peptides and nucleic acids[21]) and contain many different atom types. Others aim to reproduce the behaviour of a few specific systems, for example many force fields exist specifically for modelling water, which has proven challenging to treat accurately due to its unusual chemistry.[25] Force field parameterization is considered as a kind of art within science. Obtaining accurate parameters even for systems containing few atoms such as water is non-trivial, and more general force fields being used today such as UFF are the products of decades of research.

In all work carried out in this thesis (including work in Chapter 4), framework atoms are always fixed throughout simulations, and all adsorbed guest molecules, although free to

move within the framework, are rigid models. For small guests like N_2 and CO_2, in situations where dispersion forces and weak electrostatic interactions dictate adsorption binding sites, accounting for internal flexibility of the guest is more expensive and cumbersome for small guest molecules as it will mostly account for small guest vibrational motions.[26] For this reason, the work carried out in this chapter places particular emphasis on non-bonded energetic contributions (van der Waals and electrostatic interactions).

3.2.2 Non-bonded interactions

As stated previously, non-bonded interactions included in force fields can be broadly separated into two categories: electrostatic interactions and van der Waals interactions. Generally, these interactions will be calculated for atom pairs which are connected through no less than 2 atoms and are called 1,4 interactions.

Electrostatic interactions represent the effect of internal redistribution of electrons. These effects can be quite strong and can also occur over long distances. They can be separated into four different categories: ion-ion interactions, ion-dipole interactions, dipole-dipole interactions and higher multipole moment interactions (these include quadrupolar and octapolar interactions). The total electrostatic energy will be composed of a sum of all distinct interactions in a system. In order to calculate the interaction energy between ions and/or dipoles, partial atomic charges are assigned to all atoms in the system. For smaller systems, the charges are assigned to correctly reproduce a molecule's net charge or permanent dipole. In larger more complex systems, the atomic charges are typically derived through fitting to the ESP, in an analogous way to the atomic charges derived with the REPEAT method for periodic materials (see Chapter 2).[27] In any event, partial atomic charge is not a physical observable like a permanent dipole or a magnetic moment for example, so

there are several other existing methods to assign charges to atoms, for example Mulliken charges, which are very easy to calculate thanks to their dependence on convenient nuclei-centered basis functions.[28] In cases where partial atomic charges cannot correctly reproduce multipole moments, it is also possible to place charges upon the system which are not centered on atoms (see Figure 3-3, where charges are place on a "dummy" atom for N_2). The electrostatic interactions are especially important in reproducing permanent molecular multipole moments, which are paramount in the description of non-bonded interactions such as hydrogen bonding.

Van der Waals interactions represent the short-range steric repulsions and mid-range dispersive attractions between atoms which are not bonded directly to each other. These are very important, as they serve to capture induced dipole-dipole interactions and London dispersion forces. It is the main interaction between non-polar molecules (eg. Alkanes) and it is the only possible interaction between rare gas atoms. Unlike with electrostatic interactions involving partial atomic charges, there isn't a single, unique parameter which governs this behaviour. To accurately capture these effects, it is only necessary to select a function which presents certain characteristics, including:

- At long interatomic distances (r_{ij}), E_{vdw} tends towards zero (no van der Waals interaction between two very distant particles);
- At short r_{ij}, E_{vdw} should become very positive (due to highly repulsive energy);
- At intermediate r_{ij}, E_{vdw} should achieve a slightly negative minimum. This represents the lowest energy distance which separates two particles at equilibrium.

The most popular function which obeys the general requirements for van der Waals interaction is the Lennard-Jones potential. Others exist, such as the Buckingham potential for example, but the Lennard-Jones form is favoured by many as it only has two parameters and is computationally quite efficient.[29] The latter reason derives directly from the Lennard-Jones equation's form, and will be further discussed in the next section.

3.2.3 Lennard-Jones Potential

Lennard-Jones models reproduce non-bonded interactions using a pairwise-additive Lennard-Jones 12-6 potential function:

$$U(r_{ij}) = 4\varepsilon_{ij}\left[\left(\frac{\sigma_{ij}}{r_{ij}}\right)^{12} - \left(\frac{\sigma_{ij}}{r_{ij}}\right)^{6}\right] \quad (1)$$

Where r_{ij} is the distance between the two interacting particles, ε_{ij} is the potential well depth and σ_{ij} is the separation between the two particles when the potential ($U(r_{ij})$) is zero. The reason the Lennard-Jones potential is more computationally efficient than other potential forms is because of its 12-6 functional form. In computing, calculating exponential functions (needed for the Buckingham potential form) or square roots is around 5 times more expensive than multiplication and additions. In the Lennard-Jones 12-6 form, a 6^{th} power calculation is required, and because of this calculation the 12^{th} power calculation (the square of the 6^{th} power) is not very much more effort. However, with other potentials, such as a higher accuracy Lennard-Jones 12-10 form, calculation of both a 10^{th} and 12^{th} power becomes significantly more expensive.[29]

Interactions between different atom types are calculated using the Lorentz-Berthelot mixing rules, which are:

$$\sigma_{ij} = \frac{\sigma_{ii}+\sigma_{jj}}{2} \quad (2)$$

$$\varepsilon_{ij} = \sqrt{\varepsilon_{ii}\varepsilon_{jj}} \quad (3)$$

In this way, Lennard-Jones parameters can be calculated for all atom pairs in any system, so long as parameters are defined for every individual atom type. An example of Lorentz-Berthelot mixing as well as the shape of the Lennard-Jones potential is shown in Figure 3-1 below.

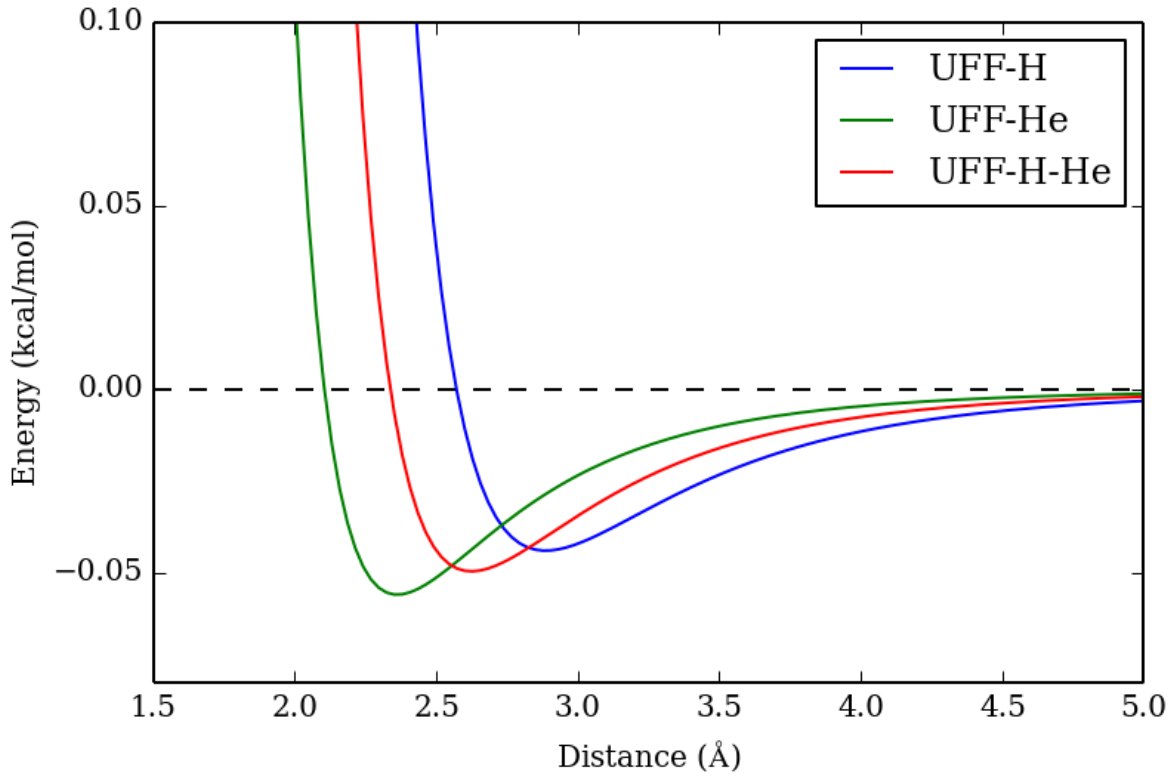

Figure 3-1. *The Lennard-Jones potentials for UFF-derived H---H (blue), He---He (green), and Lorentz-Berthelot mixed H---He (red) van der Waals interactions are shown. The left region of the plot shows the behavior of the potential when the atoms are brought very close together (increase in energy) while the right part of the plot shows the behavior of the potential when the atoms are brought very far apart (the energy tends towards 0).The units for sigma (σ) are Å, the units for epsilon (ε) are kcal/mol.*

3.3 Literature Review

Before beginning to describe any kind of parameterization effort, it is useful to more deeply explore the literature relevant to simulated adsorption of nitrogen gas. In this section, we aim to describe what current models exist for N_2 and other efforts in parameterization.

Previous studies have been performed to compare the accuracy of different N_2 models for adsorption in porous media, which demonstrate that in different sorbents and circumstances, certain nitrogen force fields will be more appropriate.[15,30] In certain cases, MOF scientists have even taken existing N_2 force fields and, due to poor performance, parameterized them for their specific experiment.[31] In fact, a force field for N_2 for adsorption in coordinatively unsaturated MOFs has already been created by Dzubak *et al*.[19], and another for adsorption in ZIFs.[20,32] PHAST-N_2, a polarizable five-site N_2 force field parameterized to reproduce high-level electronic structure calculations, was recently developed by Cioce *et al*. for general material sorption and separation processes.[33] However, a force field for N_2 created using the simple Lennard-Jones potential parameters for specific use in coordinatively saturated MOFs, which compose a major part of the scope of MOFs examined today, has never been explored.

Force fields produced through parameterization fall into two major categories: so-called ab initio-based models which are fit to reproduce expensive high level quantum calculations and empirical models, which are fit to reproduce experimental data. Both methods have advantages and disadvantages, and neither approach is better than the other because both will contain approximations.[34] Several ab initio force fields have been derived for small gases in specific MOFs (CO_2, N_2 and H_2O in open-metal site MOF-74 for different metal SBUs {Mg, Zn and Fe}[18,19,35,36], CH_4 in open-metal site Cu-BTC[18], H_2 in 5 different

MOFs[37] and CO_2 in a variety of MOFs and ZIFs[38]). Other first principles force fields are meant for gas adsorption in adsorbents more generally, such as the recent N2-PHAST[33] and CO2-PHAST[39] models. The polarizable ab initio CO_2 and N_2 force fields derived by Schmidt *et al.,* although not meant explicitly for use in adsorption and with extra parameterization for adsorbate-adsorbent parameters, have been used successfully to model adsorption in ZIFs.[20,40] In terms of experimentally-derived force fields, many exist which reproduce physical properties of the bulk molecule, such as the N_2, CO_2 and alkane TraPPE models, which reproduce experimental liquid-vapor equilibria.[9] However, these gas force fields may be problematic for use in adsorption, as their properties may change once adsorbed. Although experimentally-derived force fields have not been explored much for MOFs specifically, a force field fit to experimental zeolite uptake isotherm inflexion points was developed recently by Garcia-Sanchez et al.[10] In a similar vein, several researchers have re-parameterized the force field parameters which characterize interactions between zeolite framework atoms and gas molecules (the parameters which would normally be determined from mixing rules).[41–43] We are unaware of any N_2 force field which has been fit to reproduce experimental isotherm data, much less to reproduce experimental MOF isotherm data.

The N_2 TraPPE model[9], which is parameterized to reproduce pure gas liquid-vapour equilibria, is frequently used in the literature for simulating nitrogen gas uptake in MOFs[14,16,17,44–49] and in certain related porous sorbents.[50] We find that the TraPPE nitrogen force field overestimates the amount of N_2 adsorbed for all coordinatively saturated MOFs tested, as shown in Figure 3-2 for two MOFs. We also find that although there is always overestimation of uptake of nitrogen gas in MOFs, the proportion by which adsorption is

overestimated is not constant: as can be seen in Figure 3-2, in certain cases, overestimation is around 50% the corresponding experimental value (MOF-177[51] in Figure 3-2) but in other cases, it is well over 100% (TIF-A1[52] in Figure 3-2). It should however be noted that these estimation errors appear only when N_2 is adsorbed at temperatures higher than 77K. This is because N_2-TraPPE was originally designed for liquid simulations, and its boiling point is 77.355K. Therefore, simulated uptake isotherms used for BET method calculations, which makes use of 77K N_2 gas adsorbed at pressures up to 1 bar, should be accurate.[33,48,53]

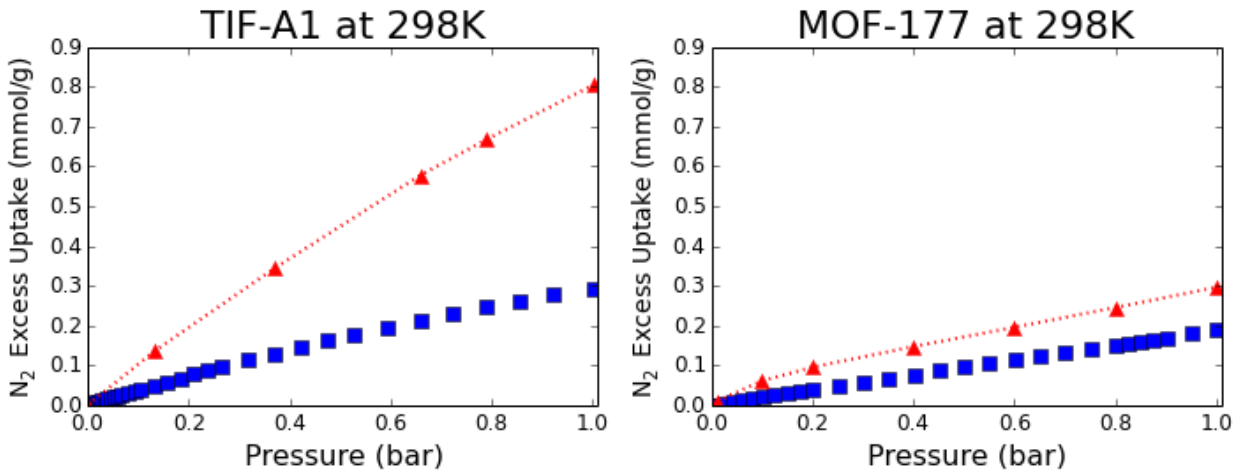

Figure 3-2. *Test isotherms for performance of N2-TraPPE model (red triangles) in MOFs TIF-A1 and MOF-177 at 298K show overestimation of experimental N2 uptake (blue squares). Experimental isotherm data is obtained from references 34 and 33 respectively.*

The atomic and COM charges found on N_2 TraPPE were not subjected to the parameterization carried out in this work. Prior computational studies by Liu and Smit[16] as well as by Karra and Walton[45] on coordinatively saturated MOFs, namely MIL-47(V) and IRMOFs-1, 3, 11, 12, 13 and 14 show that the effect of electrostatic interactions on N_2 adsorption in the MOFs tested was negligible. Indeed, single-component adsorption of gases in MOFs can in certain cases be accurately modelled using a force field without charge, as is sometimes done with the model developed by Murthy *et al.*[54–56] Although the charges on N_2 TraPPE don't significantly affect gas uptake, the quadrupole-derived charge sites are

important and should be maintained for a general N_2 force field destined for adsorption in MOFs, especially if binary gas adsorption studies with CO_2 or O_2 are to be performed. As experimental multi-component gas adsorption is rather challenging, the effect of gas co-adsorption is often calculated based on experimental single component adsorption using the Ideal Adsorbed Solution Theory (IAST) method, for example.[57] It is relatively simple to model multi-component gas adsorption, therefore simulations can provide very valuable data on the effect of adsorbing gas in the presence of other guests. For this reason, N_2 charges were maintained in our force field.

Initial testing of the Lennard-Jones parameters (σ and ε) showed that a change in the N_2 parameters yielded different changes in the simulated isotherms for different MOFs. This is shown for MOFs CALF-15[12,58] and UMCM-1[59] in Figure 3-3 below. Models in which the TraPPE Lennard-Jones σ and ε parameters were modified either by adding or subtracting 10% of their value were tested to observe the effect of changing parameters on uptake. In Figure 3-3 below, this is particularly obvious in the case of the TraPPE parameters in which the σ value is 10% higher and the ε value is 10% lower: the excess uptake (see section 3.5.1 for an explanation of excess/non-excess uptake) becomes lower than that predicted by TraPPE for CALF-15 and higher than that predicted by TraPPE for UMCM-1. This is evidence that the search space for parameters is complex, which is why search space optimization must be performed to identify a better parameterization set.

The normalized least squares grid search approach was taken to identify the best set of Lennard-Jones parameters for our N_2 force field. Other search space methods exist such as the genetic algorithm (GA), inspired by natural evolution, which has been used to determine the ideal force field parameters for MOF framework atom force fields and for gas models

meant for adsorption in MOFs.[18,60] We chose the normalized least squares approach over others for several reasons. Namely, it was important to find the best possible solution to our problem, while other techniques will identify a "good" solution, but not necessarily the best; because of the weighting factors for each MOF included in the parameterization (see section 3.4.3 for details), it was necessary to select an optimization technique for which it wouldn't be necessary to repeat calculations each time the weighting was changed; finally, although the search space is quite large, it is not impossible to explore a great deal of it using "brute force", meaning that optimization techniques which are made to explore large portions of space very quickly are unwarranted.

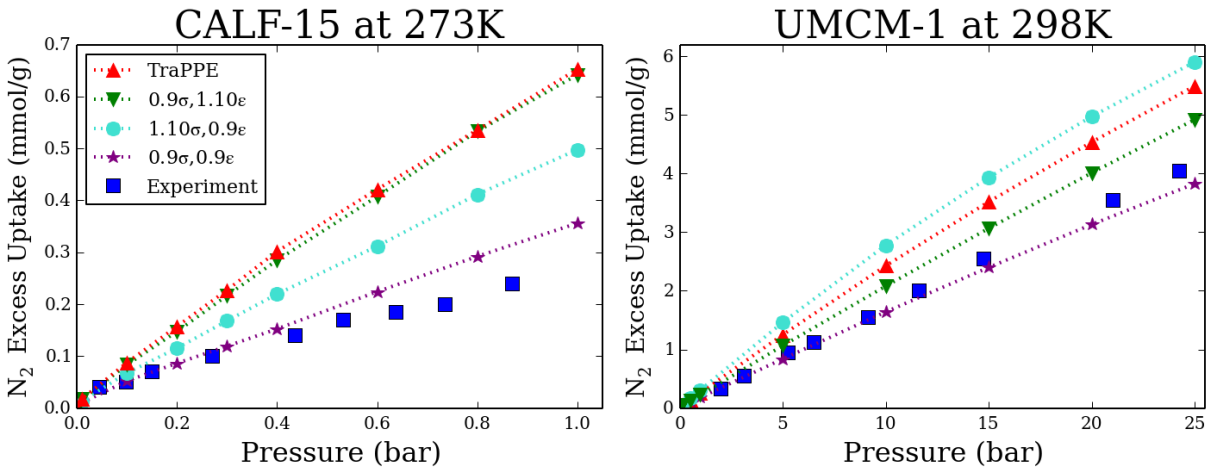

Figure 3-3. *Effect of change in sigma and epsilon parameters upon adsorption isotherms for CALF-15(273K, up to 1 bar) and UMCM-1 (298K, up to 25 bar). These tests show that the same change in Lennard-Jones parameters do not have the same effect on how the isotherm changes with respect to the TraPPE isotherm, for example when using the modified version of TraPPE with (1.10σ, 0.9ε), for CALF-15 excess uptake decreases with respect to TraPPE uptake but increases with respect to TraPPE uptake for UMCM-1.*

3.4 Methods

3.4.1 N_2 TraPPE Model

The existing TraPPE N_2 force field, which is frequently employed for simulated nitrogen adsorption in MOFs[14,17,44–49], was used as a starting point for our parameterization.[9] This model has three charge sites, two of which are centered on each N atom and one of which is found on the COM. The two N atom sites each have a charge of -0.482 and the COM site has a charge of +0.964, which account for N_2's experimental quadrupole moment ($Q = -1.4 \times 10^{-26}$ esu).[61] It is important that the nitrogen model we produce retain its quadrupole moment, as it has been shown that important interactions between the gas can be attributed to electrostatics.[12,62] We use the experimental nitrogen – nitrogen bond length of 1.10 Å, which is the same as that of TraPPE N_2.[9] A schematic diagram including details of the N_2 TraPPE model is shown below in Figure 3-4.

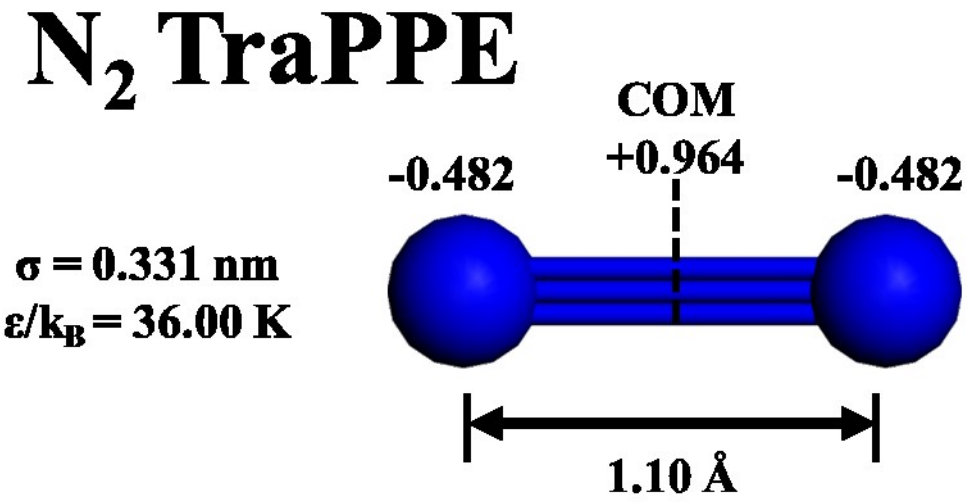

Figure 3-4. *Characteristics and relevant values for the N_2-TraPPE force field, in common use for simulating N_2 uptake isotherms in MOFs*

3.4.2 Parameterization Procedure

Parameterization is performed to improve the N_2 TraPPE potential parameters by fitting simulated GCMC isotherms to experimental isotherms. This is achieved by testing a large number of Lennard-Jones parameter combinations. To evaluate how well given Lennard-Jones parameter sets perform, a normalized least squares fitting approach was employed. Every σ and ε combination for the search space is tested, allowing for identification of the best Lennard-Jones parameter set. In this work, for each isotherm and for each ε and σ combination we calculate the average squared residual to determine how closely the simulated isotherm matches the experimental isotherm. The following equation describes how this single number, S_{ave}, is generated:

$$S_{ave_{(\varepsilon_i,\sigma_i,MOF,T)}} = \frac{1}{n}\sum n \left(\frac{U_{sim}-U_{exp}}{U_{exp}}\right)^2 \quad (4)$$

Where U_{sim} is the simulated uptake at a given pressure, U_{exp} is the experimentally determined uptake at a given pressure, n is the number of points (or different pressures) selected on the isotherm and S_{ave}, the average squared residual, serves as a metric for a given set of LJ parameters' (σ_i, ε_i) performance for that isotherm. In addition to the Lennard-Jones parameters, S_{ave} also depends on MOF identity and isotherm temperature. The closer S_{ave} is to 0, the better the performance of the given LJ parameters for a specific isotherm.

Performance for a given set of σ_k and ε_k values is determined by summing up over all isotherms for a MOF at a given temperature and all MOFs in the parameterization set. To avoid over accounting for similar features (structural, metal center type and temperatures) or less relevant features (very high or low temperature isotherms, very high pressures),

weighting factors (ω_{ij}) were used in the summation. The following equation expresses evaluation of fitness:

$$fitness(\sigma_k, \varepsilon_k) = \sum_i^{MOF} \sum_j^{T} \omega_{ij} S_{ave\,ij}(\sigma_k, \varepsilon_k) \quad (5)$$

For details regarding the weighting scheme used for parameterization, see the next section (3.4.3).

Simulation was only performed at points for which there is an experimental value, i.e. there is no interpolation. 10 pressure points (n in equation 4) were selected from the data provided for each experimental isotherm. In cases where fewer experimental isotherm data points were collected, 7 or 8 points were selected for parameterization. The pressure points are selected above 0.1 bar. Due to the shape of the isotherm curve being fairly different below 0.1 bar, inclusion of these points would have made obtaining an optimal parameterization very challenging. Points were selected to give slightly better coverage within the 0.75 – 0.8 bar range. This is done to account for the need for highly accurate uptake in this region, as it is the pressure region used for separation of CO_2 (carbon capture) or O_2 (oxy-fuel separation) from a flue stream containing mostly N_2.[63] A series of Python scripts were written to perform data generation, collection and analysis in a mostly automated fashion for the large amounts of data generated. The group-owned Wooki cluster as well as the Shared Hierarchical Academic Research Computing Network (SHARCNET) were both used to run the large number of calculations necessary for this work. A scheme showing the name, purpose and run order each of these codes is available in Appendix A.

20 σ values (1.64 Å ≤ σ ≤ 3.73 Å) and 20 ε values (6.04 K ≤ ε ≤ 51.33 K) were used for a total of 400 parameter combinations as initial search space. Once the 400 S_{ave} were obtained for each isotherm, fitness was calculated for each parameter set using the weighting

factors discussed in the next section (3.4.3). Once this initial search had been performed and a minimum fitness was identified (i.e. the best parameter set), a refined parameter set with another 400 σ and ε (2.393 Å ≤ σ ≤ 2.629 Å and 36.00 K ≤ ε ≤ 41.79 K) weighted combinations was used to identify a high precision best parameter set.

3.4.3 Parameterization Weighting Scheme

A rationally determined weighting scheme for the parameterization set was created so as not to over-account for common features (see Appendix B for a summary of the numerical weighing factors). In the weighting scheme used, five factors are used to determine the overall weight for each isotherm in the parameterization set:

Metal Center Type (1 in Table 2)

This factor is used in order to account for the different metal center types present in MOFs equally. For example, many MOFs are made with Zn secondary building units and our parameterization set reflects this, as it contains isotherm data for several Zn containing MOFs. For this reason, the contribution of Zn-containing MOFs to the final parameterization was reduced slightly from a factor of 1 (fully contributing) to 0.75 for all MOFs.

Organic Secondary Building Unit (SBU) Type (2 in Table 2)

If different MOFs had similar or the same organic SBUs, their organic SBU weighting factor was reduced.

MOF Similarity (3 in Table 2)

In several cases, we received experimental N_2 uptake isotherms at different temperatures/pressures for a same MOF. It was important not to over-account for a MOF because it had several data sets, as this would skew the best parameterization in favour of

that MOF. As an example, we used 4 different data sets for ZIF-8 in the parameterization, and for this reason we reduced its MOF Similarity factor to 0.45 from unity.

Temperature (4 in Table 2)

Uptake temperatures significantly higher or lower than 298 K were penalized, as they are of lesser relevance to CO_2 capture from a flue stream.

Pressure Range (5 in Table 2)

Adsorption of N_2 from a flue gas stream takes place at around 0.8 bar. For this reason, all data sets in which uptake of N_2 was measured up to 1 bar were accounted for fully. Data sets where adsorption takes place at much higher pressures (for example, up to 20 bar) were accounted for to a lesser extent.

The final weighting factor ω_{ij} consists of a multiplication of all five weighting factors. For our parameterization set, the final weighting factors range from low (0.135) to high (0.8) depending on the MOF and relevance of uptake conditions. It should be stressed here that the weighting scheme aims not to over-account for any features so the force field which is generated, although preferentially fit to highly accurately reproduce experimental data at 0.75 bar and 298K, is still widely applicable (Note: Generally, post-combustion CO_2 capture will occur at around 313-333 K, so ideally the range fit for highest accuracy should be 1bar, 323K.[63] A limitation of this work is that most experimental N_2 isotherms are measured at 273K – 298K, near room temperature. We find that it is a reasonable approximation to parameterize according to these limits instead, as air separation (O_2/N_2 separation) necessary for oxy-fuel combustion takes place closer to room temperature. Therefore, this compromise is necessary and reasonable). Isotherms included in the parameterization range from temperatures of 195K – 350K and pressures of 0.1 bar – 40 bar.

3.4.4 Molecular Simulation

Underlying theory and selected implementations of the molecular simulation techniques used throughout this thesis (including periodic DFT, the REPEAT charge calculation method, GCMC and ABSL) have been presented in detail in Chapter 2. Section 3.4.4 serves only to present certain details specific to the project which were omitted from that chapter.

The interaction potential between N_2 molecules and the MOF framework was modelled using UFF Lennard-Jones parameters and partial atomic charges for the framework atoms.[8] Lennard-Jones parameters for the framework atoms were taken from the UFF force field, using the Lorentz-Berthelot combination rules. A full list of the Lennard-Jones parameters used for simulation is given below in Table 3-1.

Table 3-1*.UFF Lennard-Jones parameters for all MOF atom types used in parameterization set*

Atom Type	ε/k_b (K)	σ (Å)
Zn	62.4	2.4616
Cr	7.5	2.6932
Mo	28.2	2.719
Ni	7.5	2.5248
Cu	2.5	3.1137
Co	7.0	2.5587
H	22.1	2.5711
C	52.8	3.4309
O	30.2	3.1181
N	34.7	3.2607
Si	202.3	3.8264
F	25.2	2.997

GCMC simulations were performed with the in-house code FastMC, in which all framework atoms were kept rigid for simulations. GCMC-cycles were employed (a cycle consists of N number of trial steps, where N is the number of guest molecules present at any given time). This is a useful strategy for determining equilibration and production phases of GCMC simulations on a wide range of different MOFs without resorting to imposing a strict number of steps for each phase. This strategy has been employed successfully by others for gas adsorption in MOFs.[64,65] For the refined screening, 25,000 cycles for equilibration and 25,000 cycles for production were used for each MOF.

3.5 Parameterization Results

3.5.1 Parameters

14 distinct experimentally observed MOFs were used in the Lennard-Jones parameterization set: CALF-15[12,58], [Co(HL)]2H_2O[66], CPF-6[67], CROFOUR-1-Ni[68], $_\infty$[Cu(Me-4py-trz-ia)][69], Cu(bpy-1)$_2$(SiF_6)[70], Cu(bpy-2)$_2$(SiF_6)[70], MOF-177[51], MOOFOUR-1-Ni[68], NiDABCO[71], NJU-Bai3[72], PCN-26[47], TIF-A1[52] and ZIF-8[73]. (See Figure 3-5 below for structures and linkers used in these MOFs). This set contains 6 different metal centers, most of them commonly found in experimental MOFs (Zn, Cu, Cr, Ni, Mo, and Co). Figure 2 depicts several MOFs and their organic SBUs that we used to parameterize the force field. Nitrogen adsorption had been measured experimentally at multiple temperatures of interest for several of the 14 MOFs. Isotherms collected at very different temperatures were also used in the parameterization giving a total of 28 experimental isotherms.

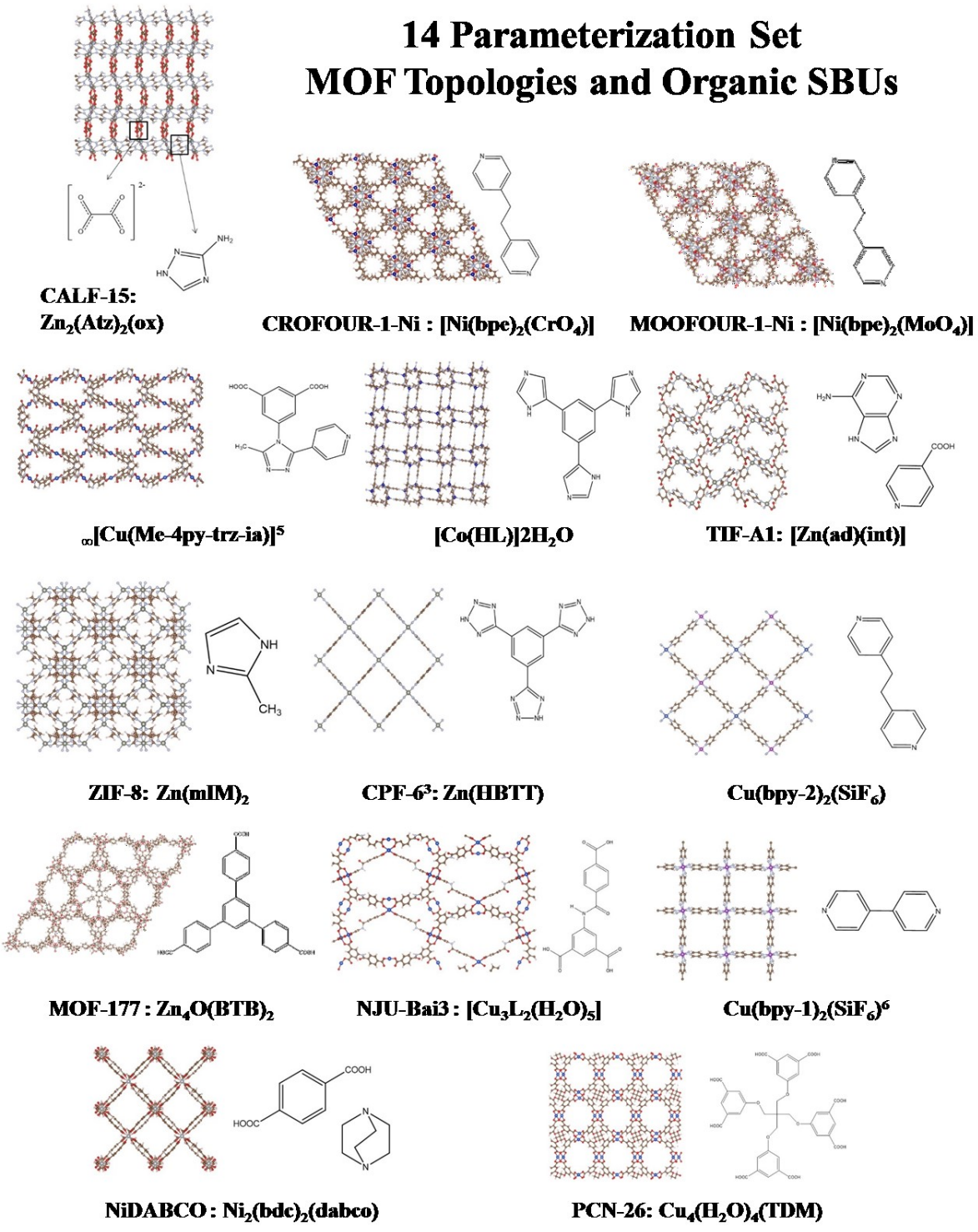

Figure 3-5. *Parameterization set MOF names & chemical formulae, corresponding topology and organic SBUs.*

Almost all adsorption data obtained was for low nitrogen uptake at ambient temperatures. This arises because the gas separation applications involving N_2 (i.e. air separation for oxyfuel combustion and carbon capture) require that MOFs capture little nitrogen gas compared to the other gas of interest (CO_2 or O_2), meaning MOFs with low N_2 uptake are considered more promising and therefore most common in the literature. We were, however, fortunate to obtain data at higher pressures (and therefore with comparatively high N_2 uptakes), which improved the diversity of our parameterization set.

To properly treat the experimental data, it is important to distinguish between excess and absolute adsorption. Excess adsorption represents the fraction of guest molecules in the pore which are in excess of those which would be present at a given pressure without adsorption at the density of the bulk gas. When no corrections are applied, GCMC measures absolute adsorption, whereas modern instrumentation (usually volumetric instruments) will measure excess adsorption by default.[74] Experimentalists can directly measure absolute adsorption using more expensive gravimetric instruments, which monitor the change in mass of a sample under isobaric conditions. The buoyancy effect incurred by the gravimetric experimental setup requires correction of absolute adsorption by He gas adsorption, resulting in an "excess" adsorption. Although use of this He-derived correction appears to be relatively standard procedure when working with gravimetric instruments in the literature, there has been discussion regarding the validity of using He as a non-adsorbing gas.[75,76] In any event, a correction must be applied theoretically when comparing with experimental volumetric excess adsorption (or He-corrected gravimetric adsorption) in order to accurately compare simulated and experimentally-derived "excess" isotherms. At low pressures and in situations in which pore volumes are negligible compared to the adsorption second virial

coefficient, the difference between excess and absolute adsorption is usually not very significant, but for the purposes of this study, these small differences become significant for the calculation of S_{ave}.[74] We observed that even the small change generated from the correction applied could make an important difference for the S_{ave} even at low pressures. For this reason, we were careful to convert our calculated absolute uptakes to excess uptakes (using either a N_2 or He probe depending on the experimental data collection technique to calculate void volume in the pore) in order to make accurate comparisons with experimental excess uptake. Conversely, in cases where gravimetric absolute adsorption was measured experimentally, we compared with our own uncorrected absolute uptakes. Table 3-2 below gives information about the type of isotherm data collected based on the instrument used for collection as well as communication with the researchers.

Table 3-2. *Parameterization Set MOFs, Isotherm Experiment Instruments and Corresponding Isotherm Types (Gravimetric/Volumetric, Excess/Non-Excess)*

MOF name	***Apparatus Used***	***Isotherm Type***	***Excess?***	***Probe Type Used***
CALF-15	Micromeritics ASAP 2020	Volumetric	Yes	N_2
CPF-6	Micromeritics ASAP 2020	Volumetric	Yes	N_2
CROFOUR-1-Ni	Micromeritics ASAP 2020	Volumetric	Yes	N_2
MOF-177	Micromeritics ASAP 2020	Volumetric	Yes	N_2
MOOFOUR-1-Ni	Micromeritics ASAP 2020	Volumetric	Yes	N_2
NJU-Bai3	IGA-003 gravimetric adsorption instrument (Hiden-Isochema, UK)	Gravimetric	No	N_2
PCN-26	Micromeritics ASAP 2020	Volumetric	Yes	N_2
TIF-A1	Micromeritics ASAP 2020	Volumetric	Yes	N_2
CoHLH2O2	Belsorp-max volumetric gas instrument	Volumetric	Yes	N_2
Cubpy1-SiF6	Micromeritics ASAP 2020	Volumetric	Yes	N_2
Cubpy2-SiF6	Micromeritics ASAP 2020	Volumetric	Yes	N_2
NiDABCO	Rubotherm Magnetic Suspension Balance	Gravimetric with He Excess Correction	Yes	He
Cu-1,2,4-triazolyl-isophthalate	Rubotherm Magnetic Suspension Balance	Gravimetric with He Excess Correction	Yes	He
ZIF-8	Rubotherm Magnetic Suspension Balance	Gravimetric with He Excess Correction	Yes	He

Using the procedure described in the Methods section, the parameter scan was performed for the 28 isotherms in the parameterization set. The results of the scans used to identify the overall best parameter set are shown in Figure 3-6. It is found that for both the coarse and refined scans (both included in Figure 3-6), the area in which the global minimum occurs is very flat, meaning that σ and ε values close to those corresponding to the global minimum will produce similarly accurate uptake results. Also of particular note in the coarse screening graphical plot (top of Figure 3-6) are the red regions, which indicate S_{ave} values much greater than 10. Although the area where the minimum is found is quite flat, the areas searched immediately adjacent to the flat region quickly have very high S_{ave} values, and near the limits of the parameter sets tested, S_{ave} values become increasingly large, indicating undesirable parameter sets for reproduction of uptake isotherms.

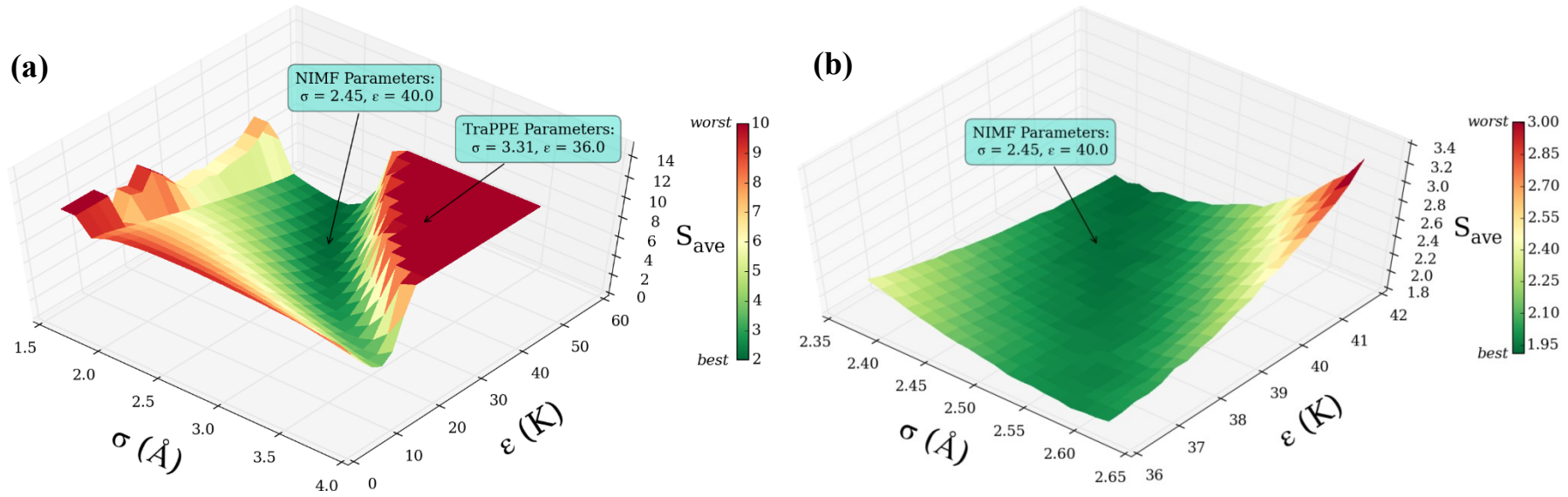

Figure 3-6. *Graphical result of least squares analysis of an initial coarse screening (a) and final refined screening (b) of 400 sigma and epsilon combinations for 28 isotherms. The arrows on the figure indicate the performance of NIMF and TraPPE parameter sets. Green areas indicate low S_{ave} values, which translates to good parameter performance. In the case of the coarse screening performed, the worst results shown in this figure are capped at a value of S_{ave} =10. This was done in order to provide a clearer picture of the good parameter sets, as many parameter sets (those in the dark red region) have a S_{ave} >> 10. For example, the S_{ave} for the TraPPE model parameters is 42.2.*

The final parameters obtained from this work for an N_2 model for specialized use in MOFs, NIMF, are shown below in Table 3-3, along with the parameters for the original force field used for parameterization, N_2 TraPPE. As can be seen, the ε value is larger and the σ value is smaller compared to the N_2 TraPPE model. When compared to the force field parameters derived from N_2 TraPPE for specific use in CuBTC by Calero *et al*, for both NIMF and their parameters, ε increases and σ decreases compared to the TraPPE value.[31] A comparison of NIMF and Calero's parameters show the NIMF value for ε is larger and that identified for σ much smaller, however it should be noted that Calero's parameters were to be applied to a single open metal site MOF, in which N_2 may behave differently than for coordinatively saturated MOFs, which were exclusively used for this parameterization set.

Table 3-3. *Lennard-Jones Parameters, Bond Distances and Charges of Nitrogen and Center of Mass (COM) for Various Parameterized N_2 models Used for Adsorption in MOFs*

Model Name	ε/k_b [K]	σ [Å]	N-N bond distance (Å)	Charge (e)		refs
				N	COM	
This work (NIMF)	40.000	2.450	1.10	-0.482	+0.964	-
N_2 TraPPE	36.000	3.310	1.10	-0.482	+0.964	9
N_2 (in CuBTC)	38.298	3.306	1.10	-0.405	+0.810	31

3.5.2 Parameterization Set MOF Uptakes

Figure 3-7 shows experimental and simulated isotherms for a variety of MOFs in the parameterization set. The comparison of TraPPE and NIMF simulated isotherms are shown, and in all instances, the NIMF force field better reproduces experimental uptake. For certain MOFs, the NIMF force field does a better job of reproducing the isotherm than for other MOFs. This arises because it is being fitted to all isotherms simultaneously and due to the use of the weighting scheme for the parameterization set. As an example, the experimental data provided for adsorption in ZIF-8 was measured at high pressure (up to 25 bar), a

pressure range which is not truly representative of oxyfuel or carbon capture applications. In addition, three experimental isotherms at different temperatures were available for ZIF-8, which translates to a decrease in weighting of each isotherm for this MOF. Finally, ZIF-8 has Zn metal centers, which are very common in this work's parameterization set (and in MOFs in general), so a weighting factor for metal center type further reduces the contribution of this specific isotherm to the determination of an overall best parameter set. Overall, the NIMF force field is successful at reproducing the parameterization set experimental isotherms.

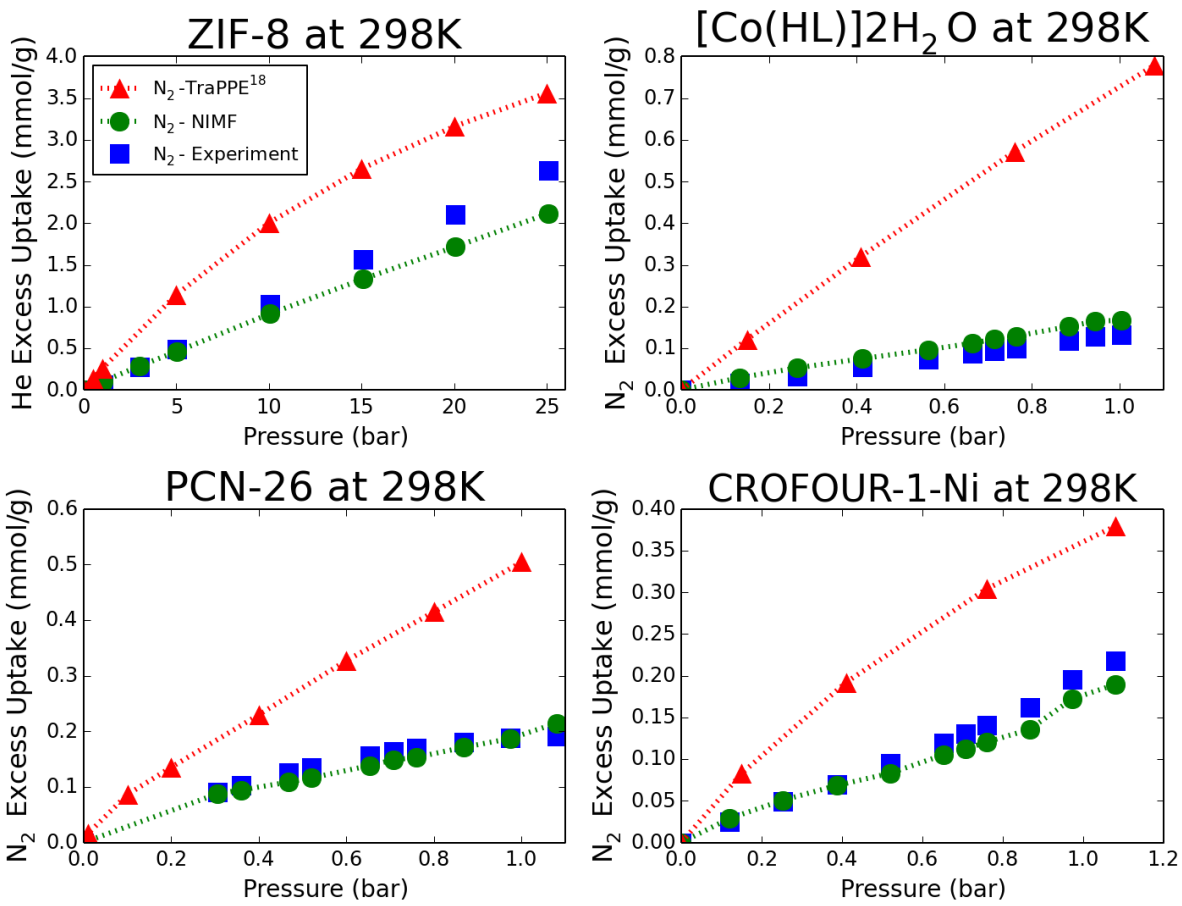

Figure 3-7. *Comparison of experimental uptake isotherms (blue), N2 TraPPE-simulated isotherms (red triangles) and NIMF uptake (green circles) for four MOFs in the parameterization set. Experimental data for ZIF-8, [Co(HL)]2H2O, PCN-26 and CROFOUR-1-Ni is taken from references 73, 66, 47 and 68 respectively. "He Excess Uptake (mmol/g)" reflects use of a He probe to determine void volume for excess calculations, as a gravimetric instrument with He buoyancy correction was used for collection of the ZIF-8 N_2 isotherm data. In all other cases, a N_2 probe was used to determine void volume.*

3.5.3 Beyond Selected Parameterization Region

Near the lower limit of sigma and upper limit of epsilon parameters shown in the coarse screening plot in Figure 3-6 (this corresponds to σ = 2.35 Å and ε/k_b = 51.33 K), where the minimum occurs, it appears as though the calculated S_{ave} may continue to decrease as the σ and ε values become more distant (i.e. σ decreases while ε increases). In fact, the overall weighted surface attains a global minimum at the indicated point, and the S_{ave}

becomes larger as σ decreases/ε increases. The following is an account of work carried out to confirm that a global minimum was attained where the NIMF parameters were determined to lie.

For the initial coarse screening (results shown graphically in Figure 3-6 in section 3.5.1) we selected a 400 combination parameter space which roughly placed the N_2 TraPPE parameters in the center of our search area. Coarse screening analysis of S_{ave} values across all MOFs showed certain interesting trends. First, S_{ave} increases with increasing σ value (while ε is kept constant). When exploring S_{ave} values along a diagonal line in the search space (ie. Increasing ε while decreasing σ) are approximately constant. One of these "diagonal lines" has the lowest S_{ave} values, even up to very low σ and very high ε values in our coarse parameterization search space. For this reason, we searched a separate, extended space with ultra-low σ and ultra-high ε values for four equally weighted isotherms from the parameterization set (CALF-15 at 293K {up to 1 bar}, TIF-A1 at 273K {up to 1 bar}, TIF-A1 at 298K {up to 1 bar} and $_{\infty}$[Cu(Me-4py-trz-ia)] at 298K {up to 40 bar}). The results from this screening are shown in Figure 3-8 below.

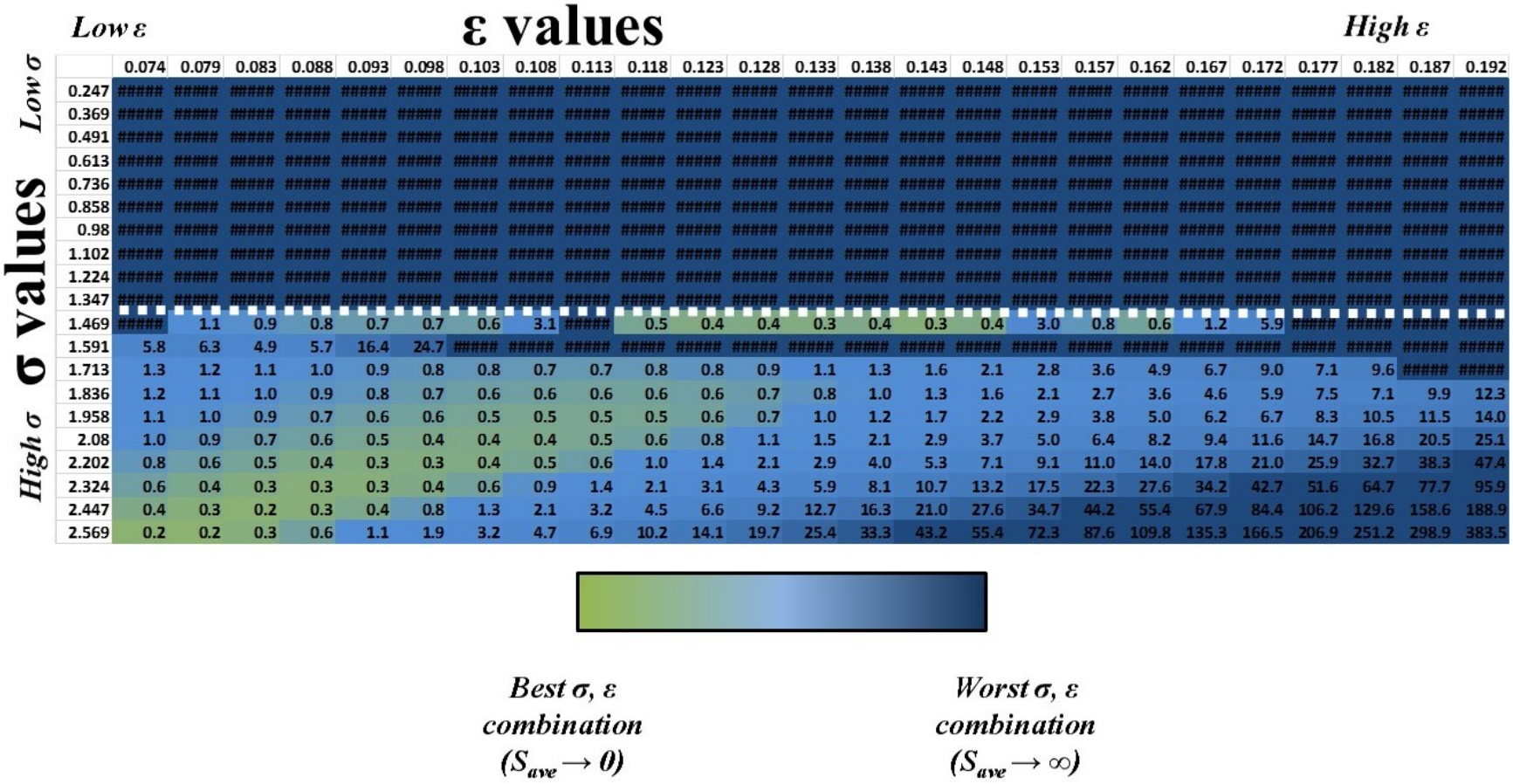

	0.074	0.079	0.083	0.088	0.093	0.098	0.103	0.108	0.113	0.118	0.123	0.128	0.133	0.138	0.143	0.148	0.153	0.157	0.162	0.167	0.172	0.177	0.182	0.187	0.192
0.247	#####	#####	#####	#####	#####	#####	#####	#####	#####	#####	#####	#####	#####	#####	#####	#####	#####	#####	#####	#####	#####	#####	#####	#####	#####
0.369	#####	#####	#####	#####	#####	#####	#####	#####	#####	#####	#####	#####	#####	#####	#####	#####	#####	#####	#####	#####	#####	#####	#####	#####	#####
0.491	#####	#####	#####	#####	#####	#####	#####	#####	#####	#####	#####	#####	#####	#####	#####	#####	#####	#####	#####	#####	#####	#####	#####	#####	#####
0.613	#####	#####	#####	#####	#####	#####	#####	#####	#####	#####	#####	#####	#####	#####	#####	#####	#####	#####	#####	#####	#####	#####	#####	#####	#####
0.736	#####	#####	#####	#####	#####	#####	#####	#####	#####	#####	#####	#####	#####	#####	#####	#####	#####	#####	#####	#####	#####	#####	#####	#####	#####
0.858	#####	#####	#####	#####	#####	#####	#####	#####	#####	#####	#####	#####	#####	#####	#####	#####	#####	#####	#####	#####	#####	#####	#####	#####	#####
0.98	#####	#####	#####	#####	#####	#####	#####	#####	#####	#####	#####	#####	#####	#####	#####	#####	#####	#####	#####	#####	#####	#####	#####	#####	#####
1.102	#####	#####	#####	#####	#####	#####	#####	#####	#####	#####	#####	#####	#####	#####	#####	#####	#####	#####	#####	#####	#####	#####	#####	#####	#####
1.224	#####	#####	#####	#####	#####	#####	#####	#####	#####	#####	#####	#####	#####	#####	#####	#####	#####	#####	#####	#####	#####	#####	#####	#####	#####
1.347	#####	#####	#####	#####	#####	#####	#####	#####	#####	#####	#####	#####	#####	#####	#####	#####	#####	#####	#####	#####	#####	#####	#####	#####	#####
1.469	#####	1.1	0.9	0.8	0.7	0.7	0.6	3.1	#####	0.5	0.4	0.4	0.3	0.4	0.3	0.4	3.0	0.8	0.6	1.2	5.9	#####	#####	#####	#####
1.591	5.8	6.3	4.9	5.7	16.4	24.7	#####	#####	#####	#####	#####	#####	#####	#####	#####	#####	#####	#####	#####	#####	#####	#####	#####	#####	#####
1.713	1.3	1.2	1.1	1.0	0.9	0.8	0.8	0.7	0.7	0.8	0.8	0.9	1.1	1.3	1.6	2.1	2.8	3.6	4.9	6.7	9.0	7.1	9.6	#####	#####
1.836	1.2	1.1	1.0	0.9	0.8	0.7	0.6	0.6	0.6	0.6	0.6	0.7	0.8	1.0	1.3	1.6	2.1	2.7	3.6	4.6	5.9	7.5	7.1	9.9	12.3
1.958	1.1	1.0	0.9	0.7	0.6	0.6	0.5	0.5	0.5	0.5	0.6	0.7	1.0	1.2	1.7	2.2	2.9	3.8	5.0	6.2	6.7	8.3	10.5	11.5	14.0
2.08	1.0	0.9	0.7	0.6	0.5	0.4	0.4	0.4	0.5	0.6	0.8	1.1	1.5	2.1	2.9	3.7	5.0	6.4	8.2	9.4	11.6	14.7	16.8	20.5	25.1
2.202	0.8	0.6	0.5	0.4	0.3	0.3	0.4	0.5	0.6	1.0	1.4	2.1	2.9	4.0	5.3	7.1	9.1	11.0	14.0	17.8	21.0	25.9	32.7	38.3	47.4
2.324	0.6	0.4	0.3	0.3	0.3	0.4	0.6	0.9	1.4	2.1	3.1	4.3	5.9	8.1	10.7	13.2	17.5	22.3	27.6	34.2	42.7	51.6	64.7	77.7	95.9
2.447	0.4	0.3	0.2	0.3	0.4	0.8	1.3	2.1	3.2	4.5	6.6	9.2	12.7	16.3	21.0	27.6	34.7	44.2	55.4	67.9	84.4	106.2	129.6	158.6	188.9
2.569	0.2	0.2	0.3	0.6	1.1	1.9	3.2	4.7	6.9	10.2	14.1	19.7	25.4	33.3	43.2	55.4	72.3	87.6	109.8	135.3	166.5	206.9	251.2	298.9	383.5

Figure 3-8. *Result of exploration of parameter search beyond that of the coarse screening search space. The search was performed for 500 parameter sets (20 sigma and 25 epsilon values) for 4 equally weighted isotherms (3 different MOFs). The threshold value of σ = 1.469 Å is indicated in the figure by a dotted white line (see text for discussion of this limit).*

From this search, we can make certain observations regarding screening at ultra-high ε and ultra-low σ. First, below values of σ = 1.46, S_{ave} values become extremely large. It is interesting to note that our search presents no such threshold value for ε). Second, when σ is kept constant, S_{ave} increases as a function of increasing ε. From screening ultra-high ε and ultra-low σ parameter combinations, the overall lowest S_{ave} value is identified at (σ, ε) = (2.56889, 43.9).

The best parameter set selected from our refined scan (NIMF) was identified to be (σ, ε) = (2.45, 40.0). The NIMF Lennard-Jones parameters (σ=2.45, ε=40.0) are similar to the best parameter set identified from the extended search (σ=2.56889, ε=43.9). It is preferable to select a parameter set which more closely resembles the N_2 TraPPE force field parameters, as do the NIMF parameters compared to this extended-search parameter set. This is because N_2 TraPPE is fit to reproduce physical properties of N_2, and the new force field we generate should preferably be able to reproduce those physical properties. In fact, in the future we hope to test the NIMF model's performance against nitrogen force fields fit to reproduce bulk phase nitrogen properties. (see Chapter 5 for more on these future directions).

For these reasons, a refined scan was performed on the top performing parameter set from the coarse screening and not from this extended screening.

3.5.4 Experimental MOF Data not Used in Parameterization

A significantly larger amount of data than that used in the parameterization set for this work was obtained. The 10 MOFs (20 isotherms, see Table 3-4 below for further details regarding temperature and pressure conditions) for which data was obtained but not used in parameterization are as follow: bio-MOF-11[77], FIR-2[78], MOF-5[79], ZIF-67[80], TIF-A1-NH_2[81],

CoHLDMFH_2O[66], {[Ni(L)2]4H2O}n and {[Co(L)2]4H2O}n[82], MIL-53(Al) (Basolite ® A100)[69] and CuDABCO[71]. In all these cases, the corresponding numerical data was not included in the parameterization set because it was not possible to modify the original N_2 TraPPE parameters in such a way to reproduce this experimental data with high accuracy. In other words, in order to correctly reproduce these experimental uptake isotherms, it would have been necessary to make a much greater change to the original N_2 TraPPE parameters than the change made in this work. As it is important for the NIMF parameters to remain somewhat close to the TraPPE parameters in order for the force field to correctly reproduce interactions between N_2 molecules *as well* as with the adsorbent, large changes to the TraPPE parameters are not desirable.

The reasons why this occur are varied, but a few of the common reasons shall be covered here. The first relates to experimental measurement of the N_2 isotherm. As has been discussed earlier, in the overwhelming majority of the data acquired in this study, N_2 uptake is quite low. This is due to the fact that CO_2/N_2 and O_2/N_2 selectivity should be as high as possible for real applications, because N_2 is not a harmful gas and should be released into the atmosphere, not captured by a sorbent. It follows that research groups would only publish data which demonstrates this. Unfortunately, because very low N_2 uptake occurs, if all solvent or other impurities present in the MOF are not degassed properly prior to adsorption of a new gas, this may have a more important impact on the uptake than if the target gas interacts strongly with the framework being studied. An example of this is shown in Figure 3-9 below, which shows the experimental N_2 isotherm at 273K up to 1 bar for bio-MOF-11, which we received from Rosi *et al.*[77] As can be seen from the plot, negative uptake occurs at low pressures up until 0.15 bar. Using this to fit the Lennard-Jones force field parameters

results in errors, as it is impossible to obtain negative uptake. The initial shape of the curve suggest that something else may have been adsorbed on the framework prior to exposing bio-MOF-11 to N_2, and that the amount of gas adsorbed at higher pressures may in reality be higher than what was registered by the instrument due to the initial negative adsorption.

Another problem which may affect the isotherm's quality is the crystallinity of the synthesized sorbent. Liu *et al.* published an article in 2007 which demonstrated that open metal site MOF Cu-BTC could display differences in uptake of 100% depending on the synthetic route employed to synthesize the same material.[62] A related issue has to do with the model chosen for simulation: a perfect, infinite repeating unit cell MOF model is used but in reality MOFs will contain defects and imperfections, and will possibly even have some amorphous character. In order to insure that this was not the main reason for N_2 TraPPE overestimating uptake in the MOFs used in our parameterization set, we compared the experimental BET surface areas, a technique for surface characterization which has been validated for use in MOFs, and calculated accessible internal surface area (using a 1.8 Å N_2 probe radius) for parameterization set MOFs.[48] As can be seen from the data in Table 3-5, these surface areas are very similar, indicating that there is little disorder in the MOF crystal, and that using a perfect, infinite model is a reasonable approximation. Further evidence that the data we acquired from many different groups is accurate is demonstrated in the near identical uptake isotherms for MOF-177 which were sent to us separately by Deng *et al.*[79] and Long *et al*.[51].

Table 3-4. *Collected Experimental Isotherms which were not included in parameterization set along with temperatures and maximum pressures of adsorption experiments.*

MOF Name	***T (K)***	***Max P (bar)***	***Ref***
Bio-MOF-11	273	1	77
Bio-MOF-11	298	1	77
FIR-2	273	1	78
FIR-2	298	1	78
MOF-5	298	1.07	79
ZIF-67	273	1	80
TIF-A1-NH_2	273	1	81
TIF-A1-NH_2	298	1	81
CoHLDMFH2O	273	1	66
CoHLDMFH2O	298	1	66
{[Ni(L)2]4H2O}n	273	1	82
{[Ni(L)2]4H2O}n	298	1	82
{[Co(L)24H2O}n	273	1	82
{[Co(L)24H2O}n	298	1	82
MIL-53-Al	273	50	69
MIL-53-Al	298	50	69
MIL-53-Al	323	50	69
CuDABCO	294	25	71
CuDABCO	314	25	71
CuDABCO	350	25	71

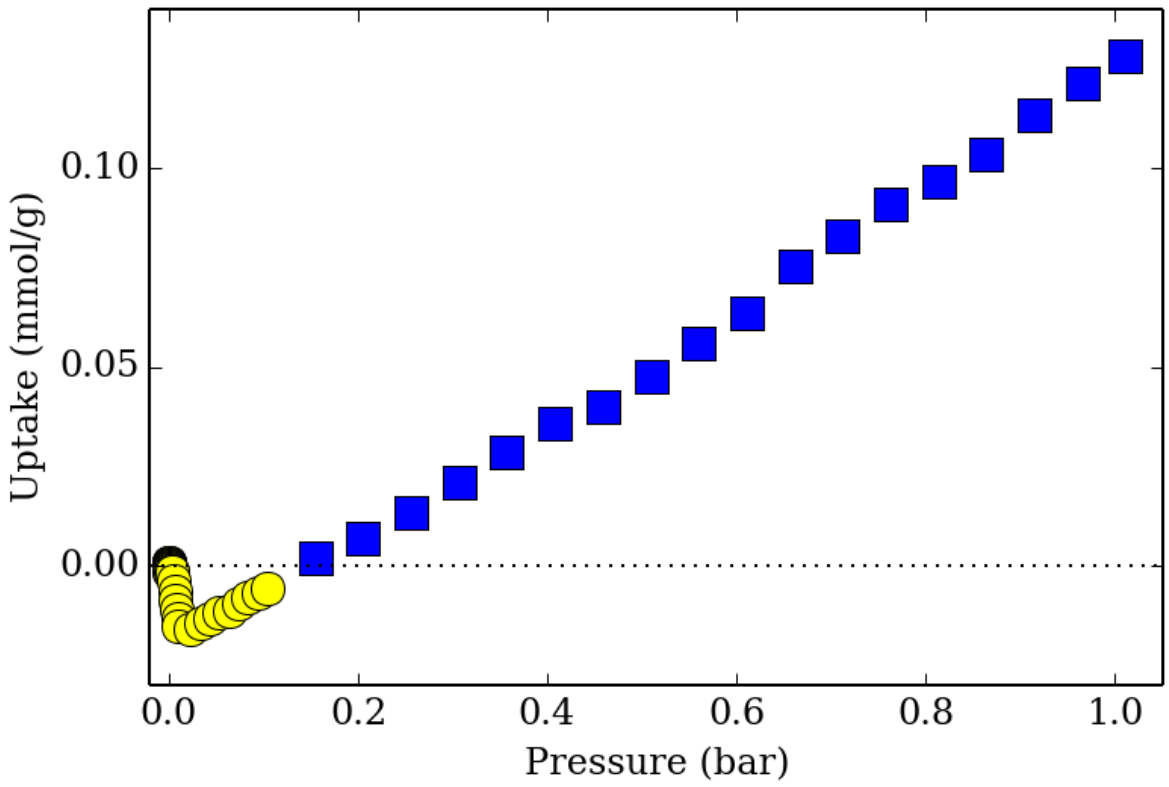

Figure 3-9. *Experimental isotherm data collected by Rosi et al. for N_2 adsorption on bio-MOF-11 at 298K up to 1 bar (data presented in reference 77). Problematic negative uptake is indicated by yellow circles.*

Table 3-5. *Experimental BET and calculated Internal Surface Areas for MOFs in Parameterization set*

MOF Name	***BET Surface Area ($m^2 g^{-1}$)***	***Calculated Surface Area ($m^2 g^{-1}$)***
NiDABCO	1904[71]	1925
Cubpy2SiF6	2718[70]	2627
ZIF-8	1273[83]	1336
TIF-A1	493[52]	436
MOF-177	4690[51]	4761

Finally, a comment should be made regarding the number of isotherms used in the parameterization set. In section 3.3, a comparison of experimental data for the MOF UMCM-1 (at 298K, up to 25 bar) was shown, however this data does not appear in the parameterization set or in the rejected data set presented in this section. This is because numerical data was not received for a large amount of MOFs which were identified as promising for parameterization. This includes several well-known MOFs which are of interest in the literature for their interesting sorption properties: UMCM-1[59]; NJU-Bai7, NJU-Bai8 and SYSU[84]; CAU-1[85] and a large number of ZIFs, including ZIF-68-70,78,79,81 and 82.[86] It is unfortunate that data was not received for these MOFs, as it would have contributed to better performace of NIMF in accounting for a wider variety of MOFs (namely, ZIFs would have had better representation in the parameterization set). In spite of this, especially because the amount of experimental data existing for N_2 uptake in MOFs ranging from 273-400K is not very common in the literature, the 28 isotherms we were able to obtain for our parameterization still form an excellent basis for fitting.

3.6 Validation of Parameterization

3.6.1 NIMF Uptake Predictions

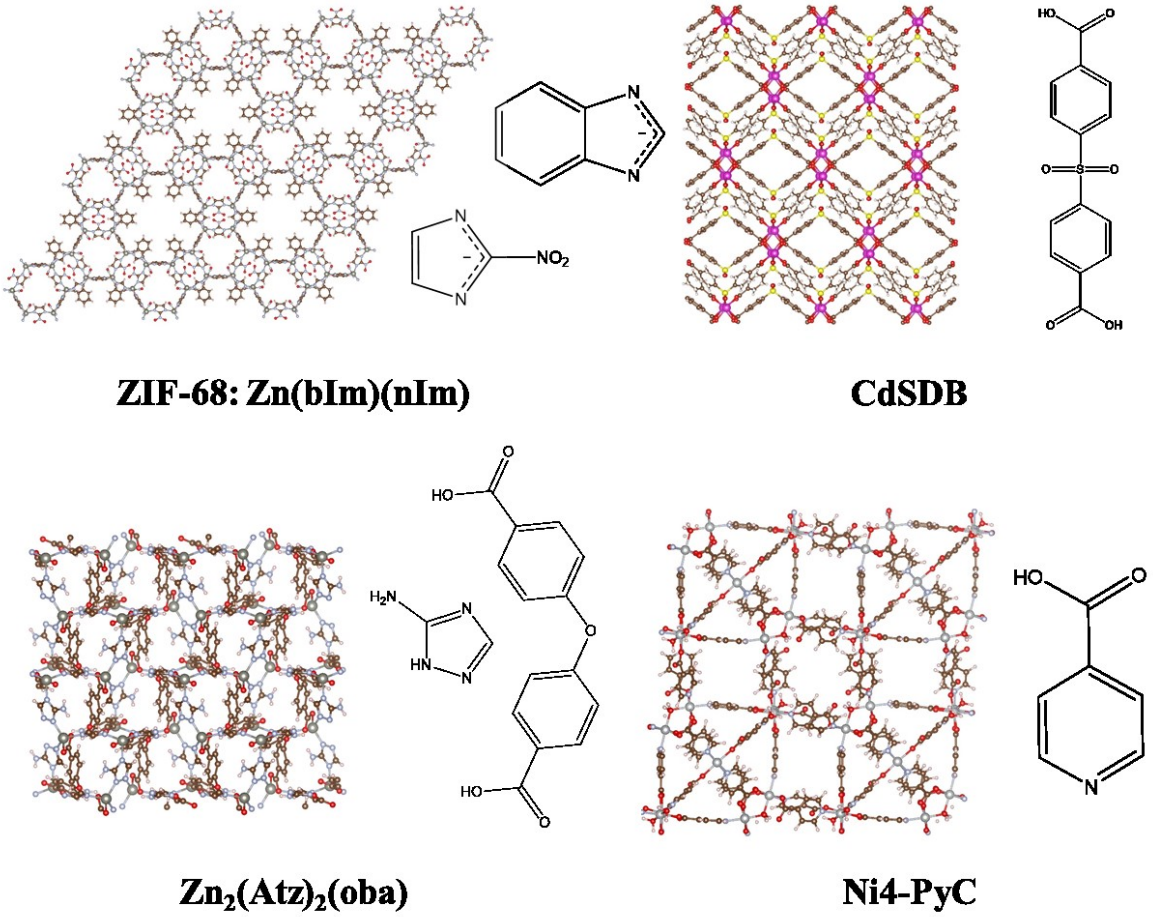

Figure 3-10. *Topologies and organic linkers for MOFs in NIMF Validation Set*

It was important to include as much experimental isotherm data in the parameterization set as possible to obtain a highly transferable set of parameters. It is also important to verify how well this parameter set predicts N_2 isotherms for a set of MOFs not used for parameterization of the force field. The NIMF force field was used to evaluate N_2 uptake predictions on a test set of four structurally distinct MOFs not included in the parameterization set: ZIF-68[86], $[Zn_2(atz)_2(oba)]$[87], CdSDB (SDB = 4,4'-sulfonyldibenzoate)[88] and Ni4-PyC[89]. As is shown in Figure 5, the NIMF force field predictions are much closer to the experimental uptakes than the N_2-TraPPE simulated

uptake predictions. Table 2 shows the uptake overprediction errors associated with use of N_2 TraPPE, as well as the higher accuracy prediction afforded using the model developed in this work. In particular, for the MOF CdSDB, the improvement in uptake prediction using NIMF is of around 700%. This is accomplished in spite of the MOF containing Cd, which is not a metal center which was included in the parameterization set. In addition, CdSDB has a V-shaped bent organic SBU, which does not resemble any of the organic linkers used in the parameterization set. From computational study with N_2 TraPPE alone, it is likely that this MOF would have been identified as a low performer due to lowered selectivity. Indeed, calculated simulated selectivities for the three test set MOFs show that use of TraPPE will lead to underprediction of selectivity by factors ranging from 3 to 6. Table 3-7 in section 3.6.2 shows the difference in simulated selectivity using both TraPPE and NIMF force fields.

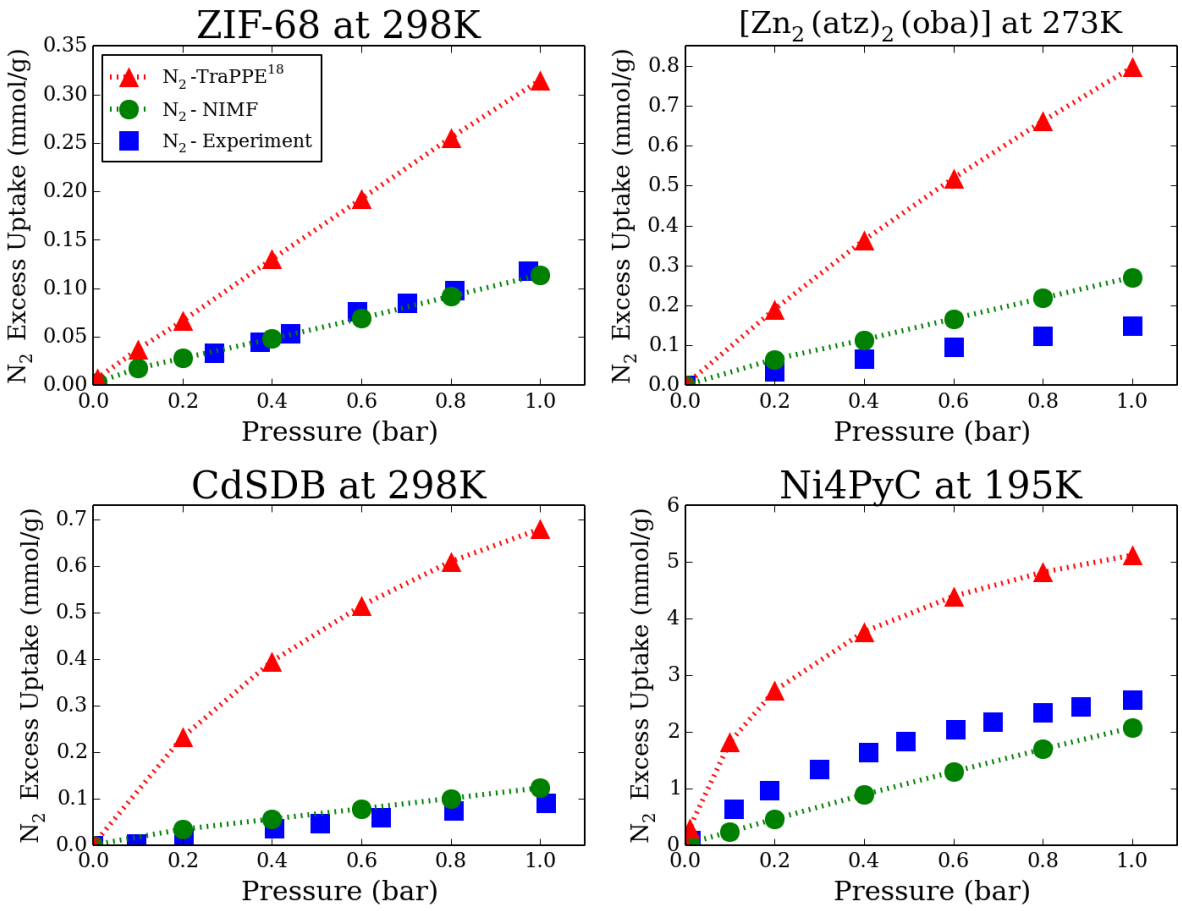

Figure 3-11. *Comparison of experimental uptake isotherms (blue squares), N2-TraPPE simulation isotherms (red triangles) and new N2 FF (green circles) for MOFs not contained in the parameterization set. Experimental data for ZIF-68, [Zn2(atz)2(oba)], CdSDB and NiPyC is taken from references 86, 87, 88 and 89 respectively. In all other cases, a N_2 probe was used to determine void volume for excess calculations.*

Table 3-6. *Error in uptake for TraPPE and NIMF Nitrogen force fields compared to experimental data at 0.8 bar for the four MOFs included in the test set.*

MOF Name	***Absolute Error in Uptake Prediction using TraPPE (mmol/g (%))***	***Absolute Error in Uptake Prediction using NIMF (mmol/g (%))***
ZIF-68	0.157 (160)	0.006 (-7)
[$Zn_2(atz)_2(oba)$]	0.538 (437)	0.095 (77)
CdSDB	0.535 (721)	0.026 (34)
Ni4-PyC	2.485 (106)	0.643 (28)

3.6.2 NIMF Selectivity Predictions

To estimate selectivity from single component GCMC isotherms, the following relationship can be used:

$$Selectivity = \frac{{}^{q_{CO_2}}/_{p_{CO_2}}}{{}^{q_{N_2}}/_{p_{N_2}}} \tag{6}$$

Where p_{CO_2} and p_{N_2} are the partial pressures of CO_2 and N_2 respectively, and q_{CO_2} and q_{N_2} are the uptakes of CO_2 and N_2 at their respective partial pressure conditions. As we wish to identify the improvement in selectivity afforded when using NIMF instead of TraPPE (Overestimation Selectivity Ratio), the following equation can be used:

$$Overestimation\ Selectivity\ Ratio = \left(\frac{{}^{q_{CO_2}}/_{p_{CO_2}}}{{}^{q_{N_2}}/_{p_{N_2}}}\right)_{NIMF} \Bigg/ \left(\frac{{}^{q_{CO_2}}/_{p_{CO_2}}}{{}^{q_{N_2}}/_{p_{N_2}}}\right)_{TraPPE} \tag{7}$$

In equation 7, the uptake and partial pressure for CO_2 can be removed entirely (these will be the same, ideal CO_2 uptakes for both TraPPE and NIMF cases). Additionally, the partial pressure for N_2 will be the same, as we aim to compare selectivity at the same conditions for TraPPE and NIMF. Expression 2 therefore reduces to equation 3 below:

$$Overestimation\ Selectivity\ Ratio = \frac{(q_{N_2})_{TraPPE}}{(q_{N_2})_{NIMF}} \tag{8}$$

Equation 8 directly shows the effect of N_2 force field type on selectivity. In all cases shown in Table 3-7 below, selectivity is underpredicted using the TraPPE model and better predictions are afforded using the NIMF force field.

Table 3-7. *Overestimation Selectivity Ratios for CO_2/N_2 selectivity in three test set MOFs when using the N_2 TraPPE force field against the NIMF force field (all N_2 simulation uptake data taken at 0.8 bar)*

MOF Name	*TraPPE N_2 Uptake (mmol/g)*	*NIMF N_2 Uptake (mmol/g)*	*Overestimation Selectivity Ratio (Eq.3)*
ZIF-68	0.255317	0.091767	2.8
$[Zn_2(atz)_2(oba)]$	0.661507	0.218336	3.0
CdSDB	0.609548	0.100163	6.1
Ni4-PyC	4.820493	1.692508	2.8

3.7 Summary

We have developed a force field for simulated adsorption of N_2 in coordinatively saturated MOFs, the Nitrogen In MoFs (NIMF) model. We used the N_2-TraPPE force field parameters designed to reproduce liquid vapour equilibria for pure N_2 gas as the starting point for modification. This force field, combined with UFF and ESP charges for the framework atoms, is in current widespread use for simulating gas adsorption in MOFs, and we have found that it significantly overestimates experimental N_2 uptake. The NIMF force field parameters are fitted to a wide variety of experimental isotherm data from literature, and further validated with experimental isotherm data. Our tests show this force field to be transferable for any coordinatively saturated MOF, and its use results in much higher accuracy uptake isotherms. This force field can therefore be used to predict uptake in MOFs which have not yet been synthesized. This work will enable computational studies to more accurately predict CO_2/N_2 and O_2/N_2 selectivities, which will greatly benefit the development of emerging carbon capture and oxyfuel-combustion technologies.

3.8 References

(1) Yang, Q.; Liu, D.; Zhong, C.; Li, J.-R. *Chem. Rev.* **2013**, *113*, 8261–323.

(2) Czaja, A. U.; Trukhan, N.; Müller, U. *Chem. Soc. Rev.* **2009**, *38*, 1284–93.

(3) Bae, Y.-S.; Farha, O. K.; Hupp, J. T.; Snurr, R. Q. *J. Mater. Chem.* **2009**, *19*, 2131.

(4) Buhre, B. J. P.; Elliott, L. K.; Sheng, C. D.; Gupta, R. P.; Wall, T. F. *Prog. Energy Combust. Sci.* **2005**, *31*, 283–307.

(5) Murray, L. J.; Dinca, M.; Yano, J.; Chavan, S.; Bordiga, S.; Brown, C. M.; Long, J. R. *J. Am. Chem. Soc.* **2010**, *132*, 7856–7.

(6) Figueroa, J. D.; Fout, T.; Plasynski, S.; McIlvried, H.; Srivastava, R. D. *Int. J. Greenh. Gas Control* **2008**, *2*, 9–20.

(7) Düren, T.; Bae, Y.-S.; Snurr, R. Q. *Chem. Soc. Rev.* **2009**, *38*, 1237–47.

(8) Rappe, A. K.; Casewit, C. J.; Colwell, K. S.; Goddard, W. A.; Skiff, W. M. *J. Am. Chem. Soc.* **1992**, *114*, 10024–10035.

(9) Potoff, J. J.; Siepmann, J. I. *AIChE J.* **2001**, *47*, 1676–1682.

(10) García-Sánchez, A.; Ania, C. O.; Parra, J. B.; Dubbeldam, D.; Vlugt, T. J. H.; Krishna, R.; Calero, S. *J. Phys. Chem. C* **2009**, *113*, 8814–8820.

(11) Vaidhyanathan, R.; Iremonger, S. S.; Shimizu, G. K. H.; Boyd, P. G.; Alavi, S.; Woo, T. K. *Angew. Chem. Int. Ed. Engl.* **2012**, *51*, 1826–9.

(12) Vaidhyanathan, R.; Iremonger, S. S.; Shimizu, G. K. H.; Boyd, P. G.; Alavi, S.; Woo, T. K. *Science* **2010**, *330*, 650–3.

(13) Iremonger, S. S.; Liang, J.; Vaidhyanathan, R.; Martens, I.; Shimizu, G. K. H.; Daff, T. D.; Aghaji, M. Z.; Yeganegi, S.; Woo, T. K. *J. Am. Chem. Soc.* **2011**, *133*, 20048–51.

(14) Zhang, W.; Huang, H.; Zhong, C.; Liu, D. *Phys. Chem. Chem. Phys.* **2012**, *14*, 2317–25.

(15) Peng, X.; Cheng, X.; Cao, D. *J. Mater. Chem.* **2011**, *21*, 11259.

(16) Liu, B.; Smit, B. *Langmuir* **2009**, *25*, 5918–26.

(17) Li, B.; Wei, S.; Chen, L. *Mol. Simul.* **2011**, *37*, 1131–1142.

(18) Chen, L.; Morrison, C. A.; Düren, T. *J. Phys. Chem. C* **2012**, *116*, 18899–18909.

(19) Dzubak, A. L.; Lin, L.; Kim, J.; Swisher, J. A.; Poloni, R.; Maximoff, S. N.; Smit, B.; Gagliardi, L. *Nat. Chem.* **2012**, *4*, 810–6.

(20) McDaniel, J. G.; Schmidt, J. R. *J. Phys. Chem. C* **2012**, *116*, 14031–14039.

(21) MacKerell, a D.; Bashford, D.; Bellott, M.; Dunbrack, R. L.; Evanseck, J. D.; Field, M. J.; Fischer, S.; Gao, J.; Guo, H.; Ha, S.; Joseph-McCarthy, D.; Kuchnir, L.; Kuczera, K.; Lau, F. T.; Mattos, C.; Michnick, S.; Ngo, T.; Nguyen, D. T.; Prodhom, B.; Reiher, W. E.; Roux, B.; Schlenkrich, M.; Smith, J. C.; Stote, R.; Straub, J.; Watanabe, M.; Wiórkiewicz-Kuczera, J.; Yin, D.; Karplus, M. *J. Phys. Chem. B* **1998**, *102*, 3586–616.

(22) Jensen, F. *Introduction to Computational Chemistry*; 2nd ed.; John Wiley & Sons, 2007; pp. 22–69.

(23) Mayo, S. L.; Olafson, B. D.; Goddard, W. A. *J. Phys. Chem.* **1990**, *94*, 8897–8909.

(24) Allinger, N. L.; Yuh, Y. H.; Lii, J. H. *J. Am. Chem. Soc.* **1989**, *111*, 8551–8566.

(25) Vega, C.; Abascal, J. L. F. *Phys. Chem. Chem. Phys.* **2011**, *13*, 19663–88.

(26) Frenkel, D.; Smit, B. *Understanding Molecular Simulation: From Algorithms to Applications*; 2nd ed.; Elsevier Ltd, 2002; pp. 23–61.

(27) Campañá, C.; Mussard, B.; Woo, T. K. *J. Chem. Theory Comput.* **2009**, *5*, 2866–2878.

(28) Mulliken, R. S. *J. Chem. Phys.* **1955**, *23*, 1833.

(29) Jensen, F. *Introduction to Computational Chemistry*; 2nd ed.; John Wiley & Sons, 2007; pp. 35–40.

(30) Makrodimitris, K.; Papadopoulos, G. K.; Theodorou, D. N. *J. Phys. Chem. B* **2001**, *105*, 777–788.

(31) Martín-Calvo, A.; García-Pérez, E.; García-Sánchez, A.; Bueno-Pérez, R.; Hamad, S.; Calero, S. *Phys. Chem. Chem. Phys.* **2011**, *13*, 11165–74.

(32) Yu, K.; McDaniel, J. G.; Schmidt, J. R. *J. Phys. Chem. B* **2011**, *115*, 10054–63.

(33) Cioce, C. R.; McLaughlin, K.; Belof, J. L.; Space, B. *J. Chem. Theory Comput.* **2013**, *9*, 5550–5557.

(34) Jensen, F. *Introduction to Computational Chemistry*; 2nd ed.; John Wiley & Sons, 2007; pp. 52–70.

(35) Borycz, J.; Lin, L.; Bloch, E. D.; Kim, J.; Dzubak, A. L.; Maurice, R.; Semrouni, D.; Lee, K.; Smit, B.; Gagliardi, L. *J. Phys. Chem. C* **2014**, *118*, 12230–12240.

(36) Lin, L.-C.; Lee, K.; Gagliardi, L.; Neaton, J. B.; Smit, B. *J. Chem. Theory Comput.* **2014**, *10*, 1477–1488.

(37) Getman, R. B.; Miller, J. H.; Wang, K.; Snurr, R. Q. *J. Phys. Chem. C* **2011**, *115*, 2066–2075.

(38) Han, S. S.; Kim, D.; Jung, D. H.; Cho, S.; Choi, S.; Jung, Y. *J. Phys. Chem. C* **2012**, *116*, 20254–20261.

(39) Mullen, A. L.; Pham, T.; Forrest, K. A.; Cioce, C. R.; McLaughlin, K.; Space, B. *J. Chem. Theory Comput.* **2013**, *9*, 5421–5429.

(40) Yu, K.; McDaniel, J. G.; Schmidt, J. R. *J. Phys. Chem. B* **2011**, *115*, 10054–63.

(41) Bai, P.; Tsapatsis, M.; Siepmann, J. I. *J. Phys. Chem. C* **2013**, *117*, 24375–24387.

(42) Pascual, P.; Ungerer, P.; Tavitian, B.; Pernot, P.; Boutin, A. *Phys. Chem. Chem. Phys.* **2003**, *5*, 3684.

(43) Dubbeldam, D.; Calero, S.; Vlugt, T.; Krishna, R.; Maesen, T.; Beerdsen, E.; Smit, B. *Phys. Rev. Lett.* **2004**, *93*, 1–4.

(44) Haldoupis, E.; Nair, S.; Sholl, D. S. *J. Am. Chem. Soc.* **2012**, *134*, 4313–23.

(45) Karra, J. R.; Walton, K. S. *J. Phys. Chem. C* **2010**, *114*, 15735–15740.

(46) Zhang, Z.; Liu, J.; Li, Z.; Li, J. *Dalton Trans.* **2012**, *41*, 4232–8.

(47) Zhuang, W.; Yuan, D.; Liu, D.; Zhong, C.; Li, J.; Zhou, H. *Chem. Mater.* **2012**, *24*, 18–25.

(48) Walton, K. S.; Snurr, R. Q. *J. Am. Chem. Soc.* **2007**, *129*, 8552–6.

(49) Yang, Q.; Vaesen, S.; Vishnuvarthan, M.; Ragon, F.; Serre, C.; Vimont, A.; Daturi, M.; De Weireld, G.; Maurin, G. *J. Mater. Chem.* **2012**, *22*, 10210.

(50) Goj, A.; Sholl, D. S.; Akten, E. D.; Kohen, D. *J. Phys. Chem. B* **2002**, *106*, 8367–8375.

(51) Mason, J. a.; Sumida, K.; Herm, Z. R.; Krishna, R.; Long, J. R. *Energy Environ. Sci.* **2011**, *4*, 3030.

(52) Wang, F.; Tan, Y.-X.; Yang, H.; Zhang, H.-X.; Kang, Y.; Zhang, J. *Chem. Commun. (Camb).* **2011**, *47*, 5828–30.

(53) Brunauer, S.; Emmett, P. H.; Teller, E. *J. Am. Chem. Soc.* **1938**, *60*, 309–319.

(54) Murthy, C. S.; Singer, K.; Klein, M. L.; McDonald, I. R. *Mol. Phys.* **1980**, *41*, 1387–1399.

(55) Chen, Y.; Jiang, J. *ChemSusChem* **2010**, *3*, 982–8.

(56) Babarao, R.; Jiang, J. *J. Am. Chem. Soc.* **2009**, *131*, 11417–25.

(57) Myers, A. L.; Prausnitz, J. M. *AIChE J.* **1965**, *11*, 121–127.

(58) Vaidhyanathan, R.; Iremonger, S. S.; Dawson, K. W.; Shimizu, G. K. H. *Chem. Commun. (Camb).* **2009**, 5230–2.

(59) Mu, B.; Schoenecker, P. M.; Walton, K. S. *J. Phys. Chem. C* **2010**, *114*, 6464–6471.

(60) Tafipolsky, M.; Schmid, R. *J. Phys. Chem. B* **2009**, *113*, 1341–52.

(61) Gray, C. G.; Gubbins, K. E. *Theory of molecular fluids, Vol:1, Fundamentals*; Oxford University Press: New York, 1984; p. 626.

(62) Liu, J.; Culp, J. T.; Natesakhawat, S.; Bockrath, B. C.; Zande, B.; Sankar, S. G.; Garberoglio, G.; Johnson, J. K. *J. Phys. Chem. C* **2007**, *111*, 9305–9313.

(63) Sumida, K.; Rogow, D. L.; Mason, J. a; McDonald, T. M.; Bloch, E. D.; Herm, Z. R.; Bae, T.-H.; Long, J. R. *Chem. Rev.* **2012**, *112*, 724–81.

(64) Wilmer, C. E.; Leaf, M.; Lee, C. Y.; Farha, O. K.; Hauser, B. G.; Hupp, J. T.; Snurr, R. Q. *Nat. Chem.* **2012**, *4*, 83–9.

(65) Farrusseng, D.; Daniel, C.; Gaudillère, C.; Ravon, U.; Schuurman, Y.; Mirodatos, C.; Dubbeldam, D.; Frost, H.; Snurr, R. Q. *Langmuir* **2009**, *25*, 7383–8.

(66) Chen, S.-S.; Chen, M.; Takamizawa, S.; Wang, P.; Lv, G.-C.; Sun, W.-Y. *Chem. Commun. (Camb).* **2011**, *47*, 4902–4.

(67) Lin, Q.; Wu, T.; Zheng, S.-T.; Bu, X.; Feng, P. *J. Am. Chem. Soc.* **2012**, *134*, 784–7.

(68) Mohamed, M. H.; Elsaidi, S. K.; Wojtas, L.; Pham, T.; Forrest, K. a; Tudor, B.; Space, B.; Zaworotko, M. J. *J. Am. Chem. Soc.* **2012**, *134*, 19556–9.

(69) Möllmer, J.; Lange, M.; Möller, A.; Patzschke, C.; Stein, K.; Lässig, D.; Lincke, J.; Gläser, R.; Krautscheid, H.; Staudt, R. *J. Mater. Chem.* **2012**, *22*, 10274.

(70) Burd, S. D.; Ma, S.; Perman, J. A.; Sikora, B. J.; Snurr, R. Q.; Thallapally, P. K.; Tian, J.; Wojtas, L.; Zaworotko, M. J. *J. Am. Chem. Soc.* **2012**, *134*, 3663–6.

(71) Mishra, P.; Edubilli, S.; Mandal, B.; Gumma, S. *Microporous Mesoporous Mater.* **2013**, *169*, 75–80.

(72) Duan, J.; Yang, Z.; Bai, J.; Zheng, B.; Li, Y.; Li, S. *Chem. Commun. (Camb).* **2012**, *48*, 3058–60.

(73) Zhang, Z.; Xian, S.; Xia, Q.; Wang, H.; Li, Z.; Li, J. *AIChE J.* **2013**, *59*, 2195–2206.

(74) Myers, A. L.; Calles, J. A.; Calleja, G. **1997**, *115*, 107–115.

(75) Herrera, L.; Fan, C.; Do , D. D.; Nicholson, D. *Adsorption* **2011**, *17*, 955–965.

(76) Gumma, S.; Talu, O. *Adsorption* **2003**, *9*, 17–28.

(77) An, J.; Geib, S. J.; Rosi, N. L. *J. Am. Chem. Soc.* **2010**, *132*, 38–9.

(78) Tan, Y.; He, Y.; Zhang, J. *Cryst. Growth Des.* **2012**, *12*, 2468–2471.

(79) Saha, D.; Bao, Z.; Jia, F.; Deng, S. *Environ. Sci. Technol.* **2010**, *44*, 1820–6.

(80) Zhang, J.; Yang, H.; Wang, F. *J. Mater. Chem.* **2012**.

(81) Yang, E.; Li, H.-Y.; Wang, F.; Yang, H.; Zhang, J. *CrystEngComm* **2013**, *15*, 658.

(82) Hou, C.; Liu, Q.; Wang, P.; Sun, W.-Y. *Microporous Mesoporous Mater.* **2013**, *172*, 61–66.

(83) Mu, L.; Liu, B.; Liu, H.; Yang, Y.; Sun, C.; Chen, G. *J. Mater. Chem.* **2012**, *22*, 12246.

(84) Du, L.; Lu, Z.; Zheng, K.; Wang, J.; Zheng, X.; Pan, Y.; You, X.; Bai, J. *J. Am. Chem. Soc.* **2013**, *135*, 562–5.

(85) Si, X.; Jiao, C.; Li, F.; Zhang, J.; Wang, S.; Liu, S.; Li, Z.; Sun, L.; Xu, F.; Gabelica, Z.; Schick, C. *Energy Environ. Sci.* **2011**, *4*, 4522.

(86) Banerjee, R.; Furukawa, H.; Britt, D.; Knobler, C.; O'Keeffe, M.; Yaghi, O. M. *J. Am. Chem. Soc.* **2009**, *131*, 3875–7.

(87) Chen, K.-J.; Lin, R.-B.; Liao, P.-Q.; He, C.-T.; Lin, J.-B.; Xue, W.; Zhang, Y.-B.; Zhang, J.-P.; Chen, X.-M. *Cryst. Growth Des.* **2013**, *13*, 2118–2123.

(88) Plonka, A. M.; Banerjee, D.; Woerner, W. R.; Zhang, Z.; Li, J.; Parise, J. B. *Chem. Commun. (Camb).* **2013**, 7055–7057.

(89) Vaidhyanathan, R.; De Luna, P.; Daff, T. D.; Woo, T. K. (unpublished results).

4 – Using Molecular Simulation to Aid in the Interpretation of Solid-State NMR spectra of Metal-Organic Frameworks

Through prior collaborative work[1], we have found that coupling molecular simulation with solid-state nuclear magnetic resonance (SSNMR) results in deep insight into behaviour of guest molecules in MOFs. Our simulations enable findings that complement the SSNMR results such as charge transfer interactions, the number and distribution of guest binding sites within a MOF, guest binding energies and dynamic behaviour of guest molecules within MOF pores. The techniques we have successfully used include force field-based molecular dynamics (MD) coupled with a spatial distribution function[1], grand canonical Monte Carlo simulation, energy decomposition, DFT studies, ab initio MD and Bader charge analysis. In addition to an overview of how the simulations are used to elucidate sometimes complex or unusual spectral data, we present the results we derive in support of ^{13}C, ^{115}In and ^{137}Ba SSNMR spectra measured for a variety of MOFs. In this Chapter, we examine the guest-host interactions in two MOFs, $Ba_2TMA(NO_3)$ and MIL-68(In) in collaboration with Professor Huang's group.*

4.1 Introduction

The use and development of analytical tools to characterize microporous materials is important, as finding links between desirable performance for a given application and structure is crucial to the development of new materials as well as the optimization of existing materials.

NMR crystallography is an emerging field in which a combination of NMR studies, powder XRD and simulations are coupled to elucidate structural information.[2,3] These types

* *Two manuscripts are in preparation in collaboration with Professor Huang's group for the two MOFs explored in this work, $Ba_2TMA(NO_3)$ and MIL-68(In).*

of multi-component studies are being carried out presently in MOFs as well as other porous materials, and constitute an especially promising complement and supplement to pure diffraction studies.[1,4,5] For a full review of experimental techniques used in the study of MOFs (including SSNMR), the reader is referred to section 1.3 of Chapter 1.

The work carried out in this chapter represents two distinct efforts in the NMR crystallography realm aimed at better understanding host-guest interactions in MOFs. Our molecular simulation studies on MOFs MIL-68(In) and $Ba_2TMA(NO_3)$ aim to shed light on the interactions of CO_2 and N,N-dimethylformamide (DMF) with these two frameworks, as well as to supplement experimental SSNMR studies carried out by Professor Yining Huang (Western University).

4.2 Theory

4.2.1 Solid-state NMR Theory

This section aims to familiarize the reader with some fundamental concepts of SSNMR, as well as background necessary for understanding the spectral data presented in this work. It is not intended to be a thorough review of SSNMR theory or practical considerations. Several comprehensive resources which outline practical considerations, underlying theory and detailed background have been produced, and should be consulted for further knowledge on this analytical technique.[6,7] As well, some reviews exist which outline the SSNMR techniques used specifically for study of microporous materials including MOFs.[8]

Nuclear Magnetic Resonance (NMR) spectroscopy is a type of analytical tool which probes interactions between spin, an intrinsic property of atomic nuclei, and an external oscillating magnetic field (B_0). It finds application in many areas and there are many different "flavours" such as one-dimensional techniques (traditional spectra which give

insight on structure), two-dimensional techniques (correlation diagrams which are used in the study of complex molecular systems), time domain NMR (studies the dynamics of probe molecules in solution) and solid-state NMR (SSNMR), the main focus of this section, which is used in the study of the molecular structure of solids. In all cases, the chemical shift (δ) obtained will be characteristic of the NMR-active nucleus within a given system, and will provide information on molecular structure.

SSNMR gained a steady following over the last forty years, and took much longer to gain wide use compared to solution-state NMR because of the comparatively low spectral resolution it affords. The broad spectral lines which are characteristic of unaltered or static SSNMR analysis arise due to orientation-specific (anisotropic) NMR interactions, which include chemical shift anisotropy (CSA), dipole-dipole coupling and quadrupole coupling. In solution-state NMR, these effects are rarely present due to rapid random tumbling of molecules, which averages all these interactions to 0. However, in solids such as crystals, powders and molecular aggregates, Brownian motion is not present, which is why orientation-dependant interactions have a strong influence on the spectrum.

SSNMR has distinct advantages over other popular characterization techniques (for example, XRD is limited to the study of crystalline lattices whereas SSNMR can provide analogous information for amorphous or inhomogeneous systems), and because of this significant efforts have been invested in the development of methods to provide improved spectral resolution. One such technique called Magic Angle Spinning (MAS), where artificial motions are introduced to the solid by spinning the sample about a “magic angle” axis of 54.74^{o} with respect to the external magnetic field, is now routinely used. Other enhancement techniques exist and are frequently used, such as cross-polarization (CP), in

which systems containing protons will transfer the magnetization associated with the protons to a dilute (isotopically or chemically) nucleus X (X=^{13}C) during a contact time to enhance signal. Different resolution enhancement approaches can also be used in combination, as is done in cross-polarization magic angle spinning (CPMAS) SSNMR. It is important to note however that experiments conducted without techniques for improved spectral resolution are also valuable, as this very broadness can provide information on molecular/electronic structure not easily provided by other means. For example, dipole-dipole coupling can be used to determine internuclear distances with relatively high accuracy.

In addition to chemical shift (δ), there are other parameters which are important in characterization of all SSNMR spectral data. Because chemical shielding is anisotropic, one of the parameters called the Chemical Shift Anisotropy (CSA), is a diagonalized chemical shift tensor with principal components δ_{11}, δ_{22} and δ_{33}. From these principal components, three parameters are derived and often used to describe SSNMR spectra. These are the isotropic chemical shift (δ_{iso}) which is the average of the three principal compoents; the skew (κ) which represents the asymmetry of the powder pattern and the span (Ω) which defines the breadth of the CSA powder pattern.

This particular work includes spectral data acquired using quadrupolar nuclei, meaning atomic nuclei having spin greater than ½. (The nuclei present in this work are ^{115}In (spin 9/2), $^{135/137}$Ba (spin 3/2) and ^{13}C which is a spin ½ nucleus.) Compared to spin ½ nuclei, they have non-spherical distribution of positive electric charge. There are two additional parameters used to characterize quadrupolar coupling, which are the nuclear quadrupole coupling constant (C_Q) which defines the magnitude of the quadrupolar interaction and the asymmetry parameter (η). Quadrupolar nuclei are more challenging to treat than spin ½

nuclei, and the effect of changing C_Q and η upon data can depend significantly upon the system. Research on systems containing quadrupolar nuclei is ongoing, and advanced technology is being actively developed to better deconvolute broad, complex lineshapes.

4.2.2 Molecular Dynamics (MD)

Molecular Dynamics (MD) is a simulation technique which is able to probe the dynamic (i.e. Time-dependant) behaviour of systems at the atomistic level. This technique, based on classical Newtonian mechanics, evaluates how positions, velocities and forces upon a collection of particles changes through time. A *trajectory* refers to the positions, velocities and forces of all particles of interest over time.

To run an MD calculation, a configuration of initial positions must be generated. The forces upon the particles in the system are then calculated. Based on the forces, the velocities and accelerations can be determined. Once the velocity and acceleration have been determined, the system can be propagated through time using classical equations of motion for one user-defined timestep (Δt). At the end of the timestep, the forces acting upon the particles are re-evaluated and resulting velocities and accelerations are computed. With these new results, the system is once again propagated through time for another Δt timestep. This cycle continues as long as desired, but in order to determine meaningful thermodynamic data, the simulation should continue until the thermodynamic values of interest have converged. This is but an overview of the general procedure in existing MD simulation codes. Modern MD simulation software will contain other components, such as for example the application of thermostats and barostats for temperature and pressure control of the system.

To run MD simulations, we have made use of the DL_POLY code.[9] The chosen timestep for simulations was 1 femtosecond. It is important to select a timestep which is short enough to observe molecular motion, but not so short that computational expense goes to waste. NVT dynamics, described as MD run with a constant number of particles, constant volume (achieved through use of a rigid framework) and constant temperature (achieved through use of a thermostat), were used exclusively throughout this thesis. In terms of the force fields used for simulation, they are identical to those used for the GCMC simulations. More information on force fields used are available in Chapter 2.

4.2.3 Binding energy calculation

Calculation of binding energy and decomposition of binding energy into its dispersive and electrostatic components for GCMC-determined binding sites is included within the ABSL code which is included within FA^{3}PS (See chapter 2 for descriptions of ABSL and FA^{3}PS). The GCMC-based energy calculation and decomposition functionality is provided by the DL_POLY code.[9]

After having obtained the binding sites and energies from the GCMC simulation, we can gain new insight on these binding sites using DFT calculations (the electronic structure code VASP is used for all DFT calculations throughout this thesis, see Chapter 2 for details). This is not to say that studying binding sites using GCMC is less valid or somehow incorrect: both approaches have their advantages and disadvantages in this context. With GCMC, temperature effects are taken into account, whereas in DFT, the optimized geometry obtained will resemble a zero temperature structure. As well, DFT is able to capture strong charge transfer interactions, whereas GCMC simulations with the classical force fields used will not feature this type of interaction.

In any event, the underlying principle used to calculate binding energy is similar in both GCMC and DFT. Binding energy of a guest to a host should include only the interaction between these two entities. It is not possible to evaluate this quantity independently, therefore three different configurations must be evaluated separately in order to calculate the energy associated with binding. The first configuration which must be evaluated is the guest within a void volume with comparable dimensions to that of the host (Note: throughout this work, there were cases in which the host void volume allows interaction of the guest with its own periodic image which leads to an erroneous energy value. In such cases, it is necessary to make use of different cell dimensions for guest optimization.). The second configuration is that of the host which does not contain the guest of interest. The final third configuration which must be evaluated is the host and bound guest configuration for which binding energy is desired. Once energy is evaluated for all three configurations, binding site energy (BSE) can be evaluated according to the following equation:

$$BSE = E_{host+guest} - E_{host} - E_{guest}$$

By subtracting the energy of the host and the energy of the guest from the combined energy calculated for guest and host, all that should remain is the energy associated with the interaction between the host and guest.

4.3 MIL-68(In)

In this section, GCMC and MD simulations in addition to DFT calculations are performed to better understand the interactions of CO_2 and N,N-dimethylformamide (DMF) with MIL-68(In) (chemical formula: $In(OH)(O_2C\text{-}C_6H_4\text{-}CO_2)$), a MOF with non-equivalent octahedral In units and two different channel types. Temperature-dependant canonical MC

simulations are also performed to understand the effect of temperature on CO_2 binding sites. The CO_2 binding sites in MIL-68(In) are compared to those of an isostructural MOF, MIL-68(Al)[10]. Throughout this section, simulation results are compared to the SSNMR spectral data acquired by the Huang group when possible.

4.3.1 Structure and SSNMR Analysis

MIL-68(In) (chemical formula: $In(OH)(O_2C\text{-}C_6H_4\text{-}CO_2)$, built up from infinite chains of octahedral metal units $\{MO_4(OH)_2\}$ linked through terephthalate or benzenedicarboxylate (BDC) linkers) is a three-dimensional MOF first made and characterized by a group at the Insitut Lavoisier Porous Solids Group responsible for the MIL (Materials Insitute Lavoisier) MOF series.[11] It has a Kagomé-type lattice, which presents two different types of one-dimensional channels: larger hexagonal channels (aperture diameter: ~ 17 Å) as well as smaller triangular channels (aperture diameter: ~ 6 Å). MIL-68(In) presents a respectable BET surface area of 746 $m^2\ g^{-1}$, can be fully evacuated of solvent by heating up to 150°C under vacuum and shows reversible H_2 uptake of 1.98 wt% at 77K and 40 bar pressure. Additionally, a study was carried out more recently in which MIL-68(In) was functionalized with amino groups, and this provided some improvement of H_2 and CO_2 uptake capacity in the MOF.[12]

The different channel-types, which run parallel to infinite chains of the inorganic units, arise due to the existence of non-equivalent metal SBUs, which we will refer to throughout this work as In1 and In2. The octahedral In SBU of In1 and In2 differ in their different In-O bond lengths (as seen from the XRD determined structure): in the case of In1, In-O bond lengths may be 2.10 Å and 2.16 Å for In-O and In-OH bonds, respectively, whereas In2 lengths are 2.02 Å and 2.15 Å for In-O and In-OH bonds, respectively. This is

confirmed through unpublished ^{115}In SSNMR performed by Professor Huang's group. Figures 4-1 and 4-2b) below show the different $InO_4(OH)_2$ octahedral arrangements in the lattice, resulting MOF lattice and SSNMR spectra for the activated MOF. ^{115}In SSNMR experiments were also carried out on the solvent-loaded and CO_2-loaded MOF (see Figure 4-2a) and c)). The results of these studies show that CO_2 loading has little impact on the ^{115}In signal, but the solvent, DMF, has a significant impact on the ^{115}In NMR signal, specifically on the In1 signal.

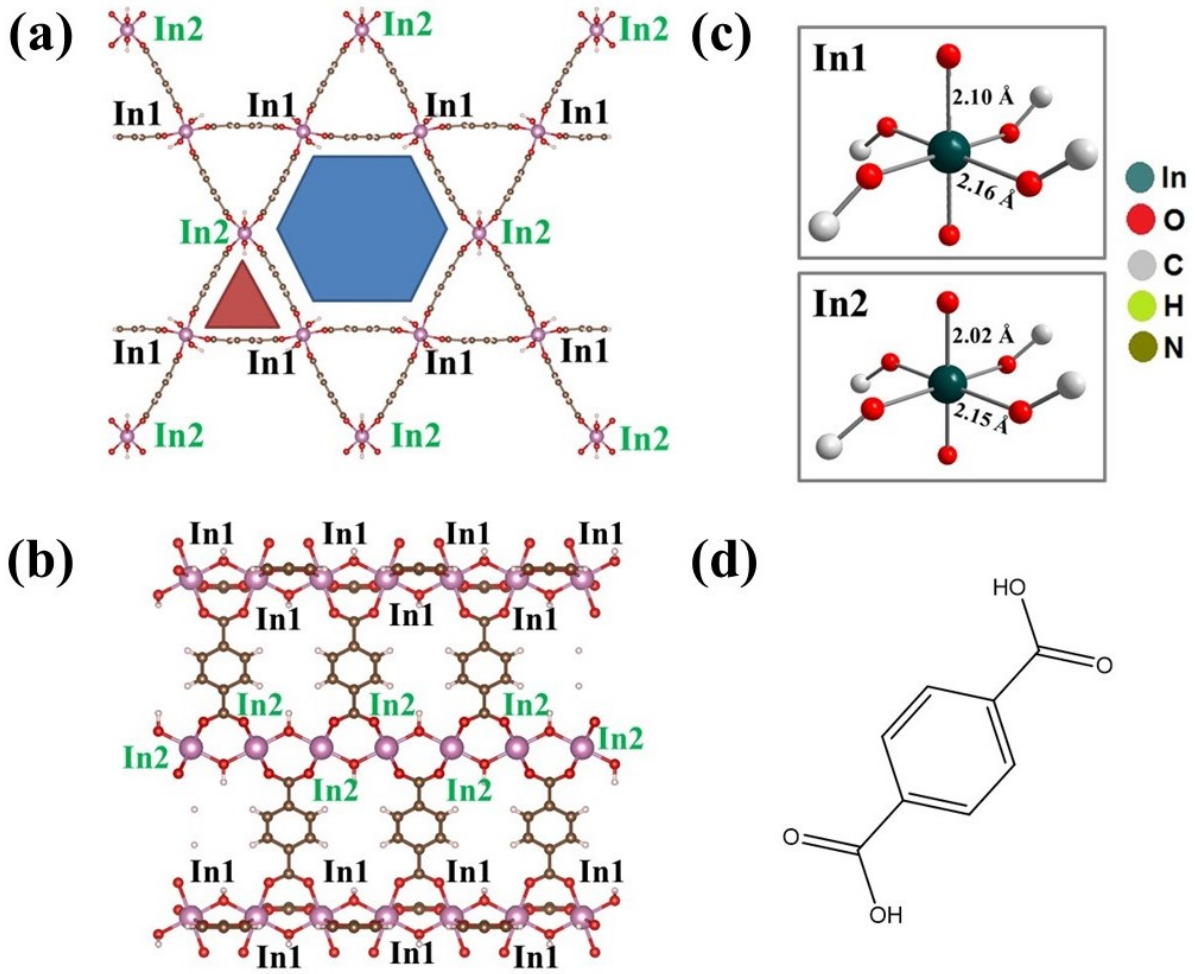

Figure 4-1. *View of the MIL-68(In) MOF 3D lattice along the c axis showing both triangular (red) and hexagonal (blue) channels formed (a). A view of the MIL-68(In) MOF 3D lattice along the a axis shows the infinite chains on the metal SBU (b). The two $InO_4(OH)_2$ octahedral units In1 and In2 are shown and distinguished (c). Finally, the organic SBU, BDC (benzenedicarboxylate) is shown (d). In1 and In2 centers are indicated within the 3D structures.*

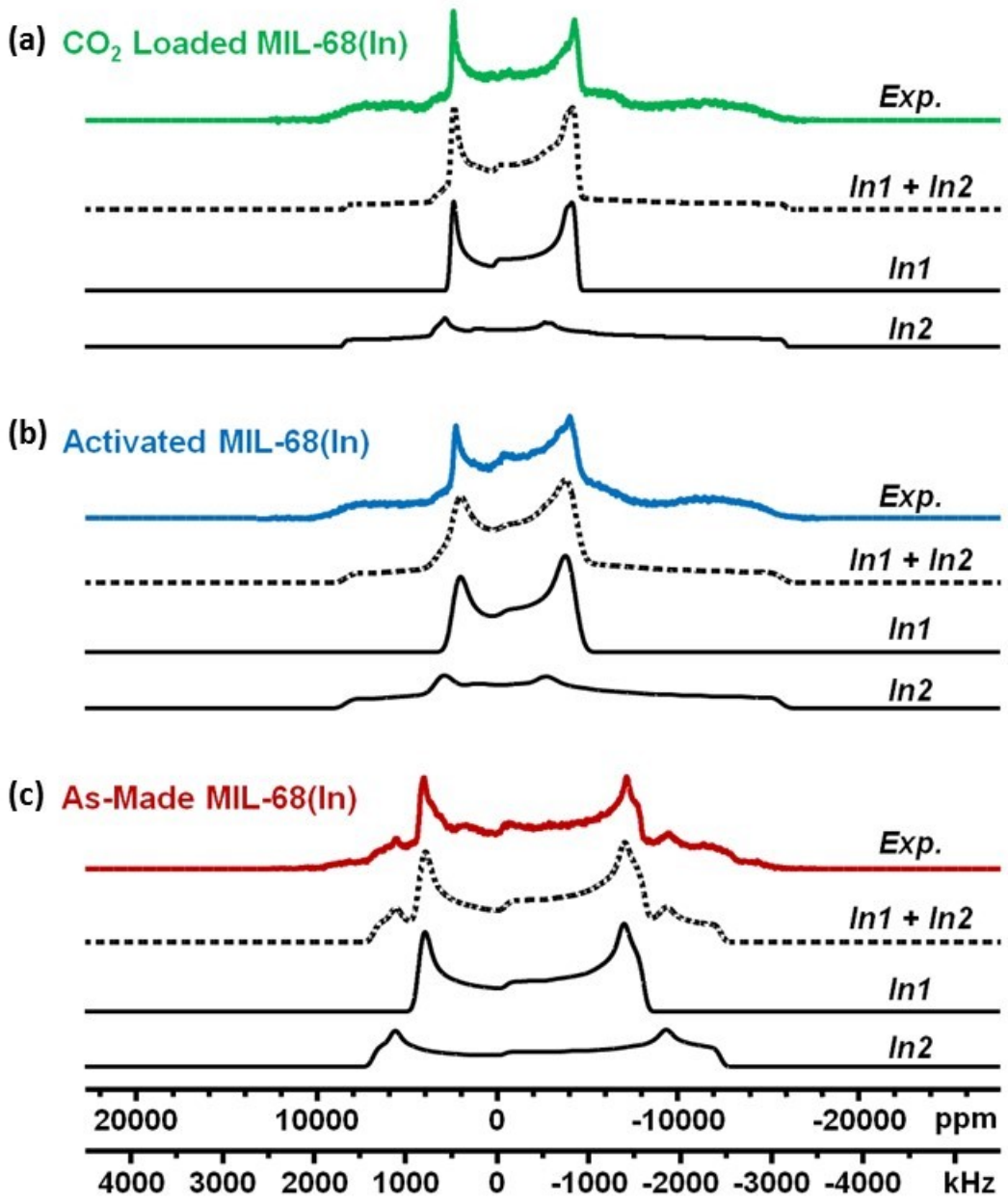

Figure 4-2. *^{115}In SSNMR spectra for MIL-68(In) loaded with CO_2 (a), activated MIL-68(In) (b) and as-made MIL-68(In), which retains some of the DMF solvent (c). For each series of spectra, simulated spectra are indicated in black for In1 signal, In2 signal as well the combination of both In1 and In2 signals. In colour, the experimental ^{115}In SSNMR spectra are shown. The assignment of In1 and In2 signals can be made based on the higher symmetry of the In1 octahedron, which presents sharper peaks. Simulated and experimental spectra acquired and provided by Professor Yining Huang (Western University)*

In addition to ^{115}In SSNMR, Professor's Huang group inspected CO_2 adsorption in MIL-68(In) using ^{13}C SSNMR. These results showed the following: first, in SSNMR ^{13}C

experiments with a low loading of CO_2 (0.1 CO_2/In), static SSNMR results showed there were at least two different CO_2 binding environments; second, in SSNMR ^{13}C experiments with a higher loading of CO_2 (0.4 CO_2/In), SSNMR results showed there were three different CO_2 binding environments. Figure 4-3 below depicts the ^{13}C SSNMR spectra acquired by Professor Huang's group. The SSNMR experiments provide some very interesting information about CO_2 binding sites, such as the number of unique binding sites and their influence on the metal atom environment, but other information which would be of interest is not available using this technique. For example, the exact location of the binding sites within the MOF (whether binding sites are found in the hexagonal space or triangular space), whether certain channels are preferred for different gas loadings, and how binding sites change as a function of temperature (although temperature dependant SSNMR spectra were acquired, they are not a simple tool for ascertaining the effect it has on number of localization of binding sites. See section 4.3.2 and Figure 4-8 for information about temperature dependant spectra).

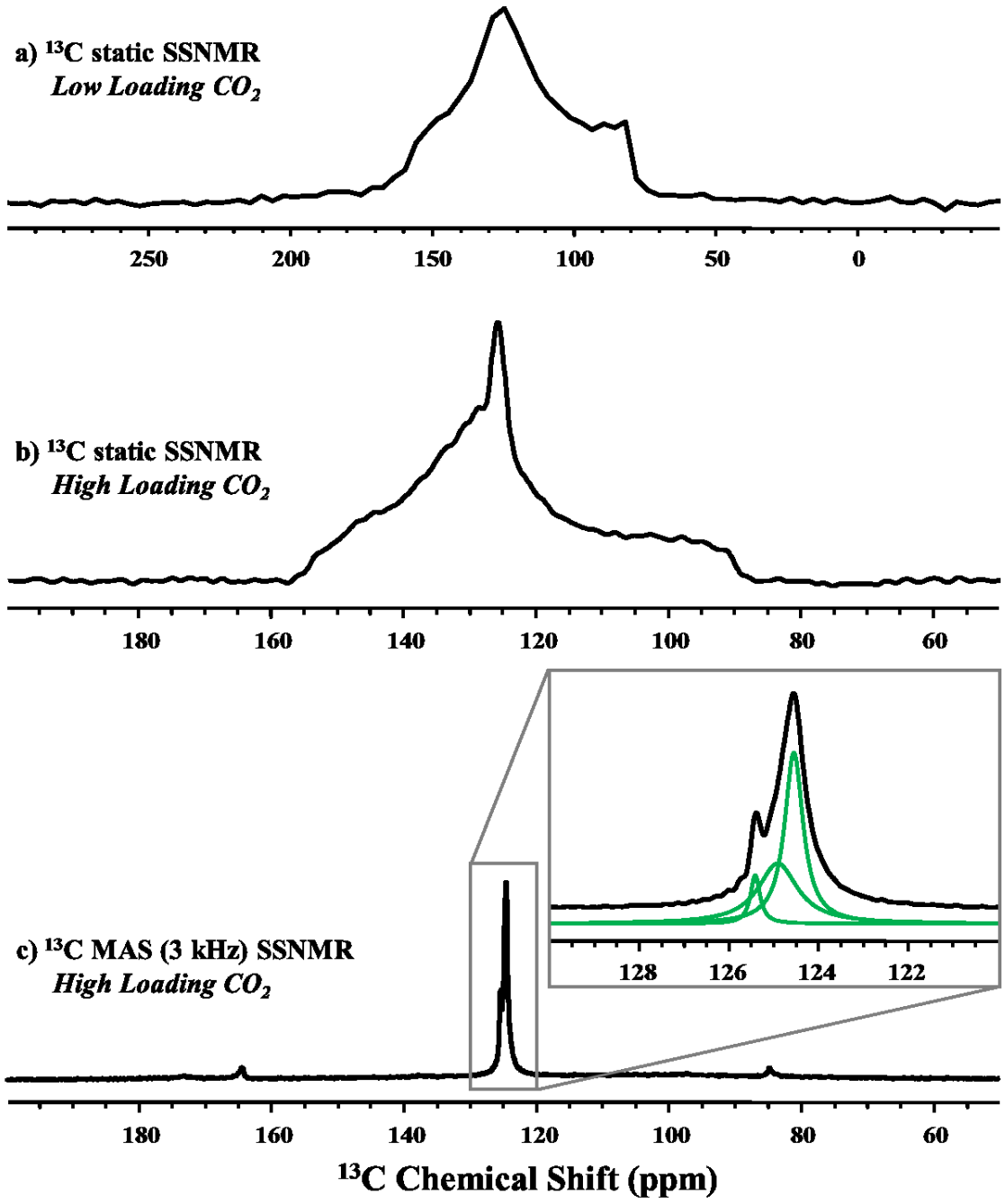

Figure 4-3. *Spectral data in a) shows static ^{13}C SSNMR data for low CO_2 loading in MIL-68(In) (0.1 CO_2/In). The static spectrum in a) shows at least two binding sites. ^{13}C SSNMR static (b) and MAS (c) data for high loading of CO_2 adsorbed in MIL-68(In) are also shown (0.4 CO_2/In). Deconvolution of the NMR peak shown in green in c) shows that the peak is in reality the sum of three overlapping peaks, indicating three different binding environments for CO_2. Note: ^{13}C signal is not shown for organic SBU contributions. ^{13}C-enriched CO_2 gas was loaded into the activated framework to increase the CO_2 signal. Data acquired and provided by Professor Yining Huang (Western University).*

In addition to analysis of the interactions of CO_2 with the framework, it can also be of interest to study how other gases interact with the framework. Not only can this provide insight on the interaction of different guest molecules with the same framework, but our conclusions can further validate the combined use of SSNMR and calculations for investigation of the behaviour of gases within MOFs. N,N-dimethylformamide (DMF) is an interesting molecule to study in this context, as it is used as a solvent for the published synthesis of MIL-68(In).[11] Often, traces of solvent can be found even within evacuated MOFs, so it is relevant to discover where the DMF coordination sites are within the MOF, including how the DMF interacts with the two In centers. In order to validate the combined use of theory and SSNMR as a tool for analysis of gas adsorbed in MOF, we carried out calculations to probe binding of DMF within MIL-68(In).

Our computational investigation of MIL-68(In) aims to elucidate the following:

- The number and localization of CO_2 binding sites within MIL-68(In);
- The temperature dependence of CO_2 binding site number and localization within MIL-68(In);
- The number and localization of DMF binding sites within MIL-68(In);
- A comparison of our binding site analysis and that obtained for an isostructural MOF[10];
- A qualitative picture of the dynamic behaviour of CO_2 binding sites within MIL-68(In).

4.3.2 CO_2 Results

4.3.2.1 Binding site analysis

Figure 4-4 presents the probability distributions resulting from the GCMC simulation of CO_2 in MIL-68(In) at 298 K and 1 bar. Four general binding sites are identified. Tables 4-1 and 4-2 show all relevant binding distances and binding energies for these binding sites. In this section, the four binding sites will be discussed individually in order of decreasing binding energy (from strongest to weakest).

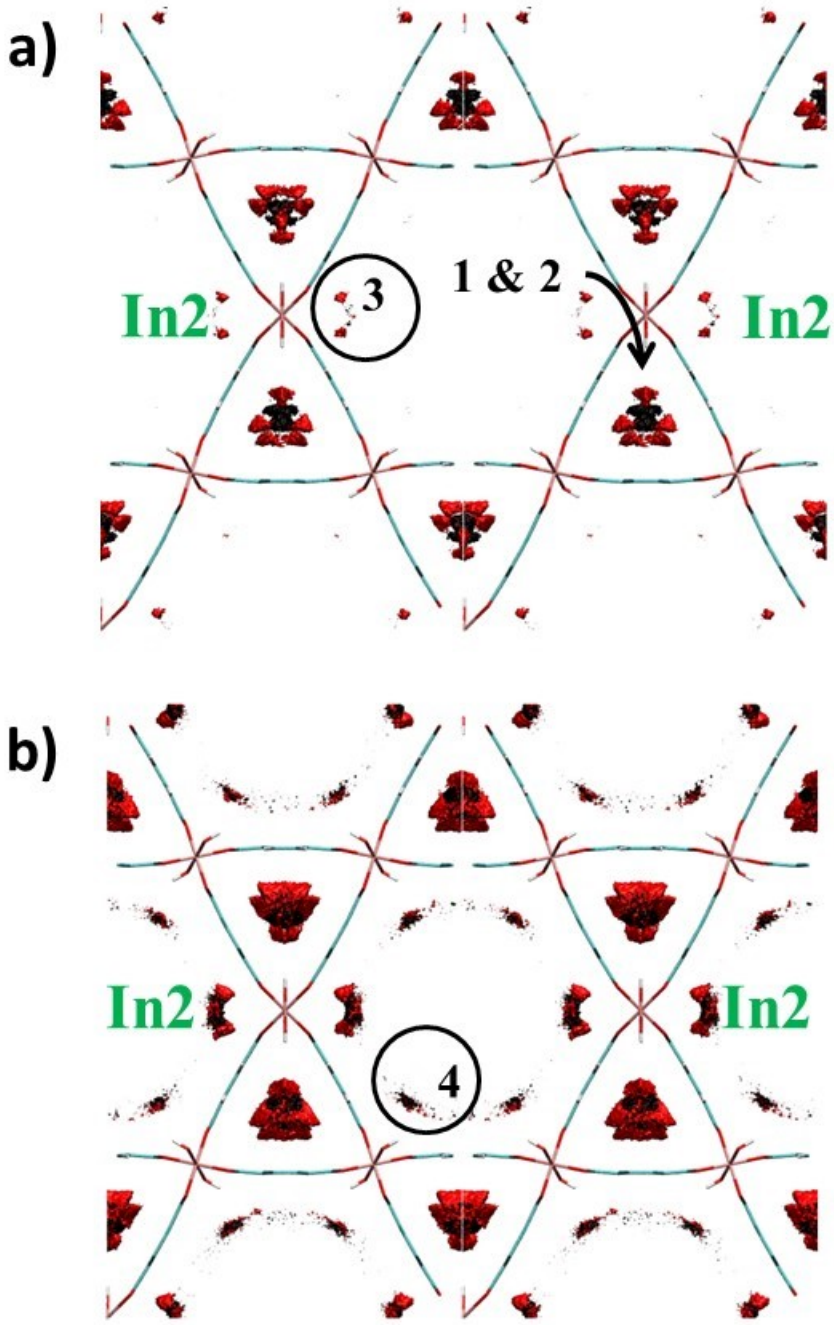

Figure 4-4. *Isosurface plots of the probability density showing CO_2 binding sites in activated MIL-68(In) at higher probability isovalue (0.02) (a) and slightly lower isovalue (0.01) (b). T = 298 K, P = 1.0 bar.Black: CO_2 - C, Red: O, Pink: In, Light blue: MOF C, White: H. In2 are indicated on the figure, and all other unmarked pink In atoms are In1.*

The first and second binding sites (**B1-CO_2** and **B2-CO_2**) are found within the triangular channel, and are shown in Figure 4-5. Before proceeding with analysis of these binding sites, it should be noted that these binding sites are better described as "binding regions". As will be discussed, although there are two distinct "regions" of binding, a few favourable CO_2 orientations can be identified within the regions.

In Figure 4-5, a side-view of the triangular channel shows that **B2-CO_2** (yellow) is found in the interstices formed by the linkers, whereas **B1-CO_2** (purple) is found directly under the linkers. All DFT-optimized binding sites within binding regions **B1-CO_2** (1.1 and 1.2) and **B2-CO_2** (2.1 and 2.2) are shown. For both binding regions, the closest atoms to the CO_2 binding site are the benzene ring (from the BDC linker) hydrogens. The DFT-optimized binding site energy values are all close, except binding site 2.2 which appears to be distinctly more favourable, likely due to the H-bonding taking place between the CO_2 oxygen and In2-OH along with the aforementioned interaction with benzene H atoms.

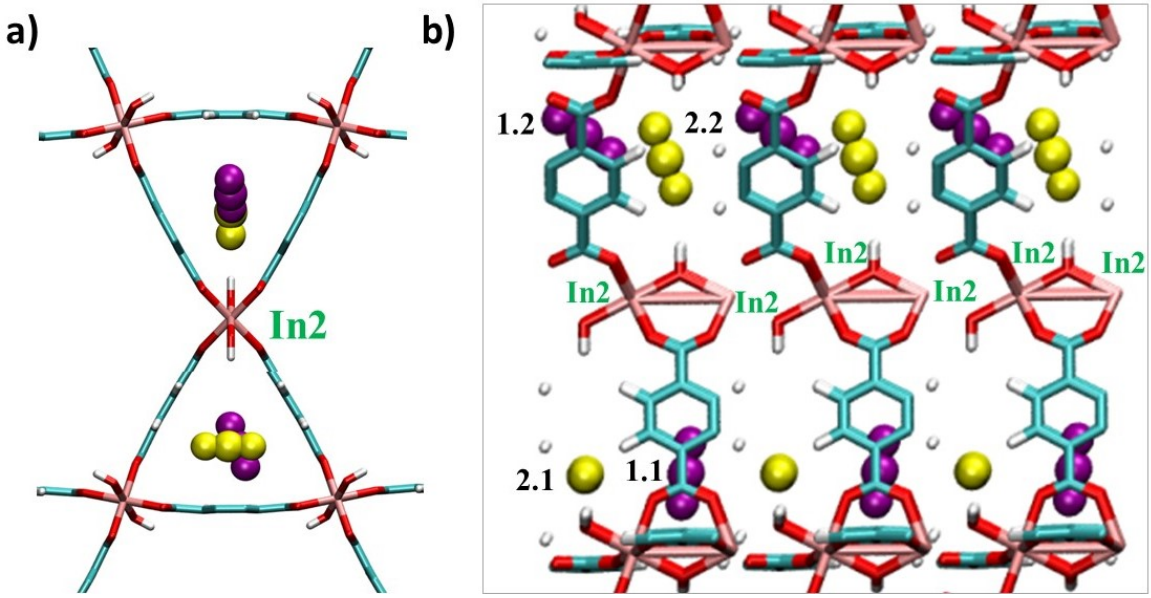

Figure 4-5. *Front view of GCMC-derived binding sites* ***B1-CO₂*** *(purple) and* ***B2-CO₂*** *(yellow) in activated MIL-68(In) (left), and side view of GCMC-derived binding sites 1.1 and 1.2 (purple) and 2.1 and 2.2 (yellow) (right), showing how the binding sites are different in their localization with respect to the linkers. T = 298 K, P = 1.0 bar. Black: CO_2 - C, Red: O, Green: In, Light blue: MOF C, White: H. In2 are indicated on the figure, and all other unmarked In atoms are In1.*

The next strongest binding site, **B3-CO₂**, appears within the hexagonal channel nearest to In2. As shown in an enhanced view in Figure 4-6, the CO_2 binding site is well localized, and is oriented parallel to the In2-OH-In2 chains. A few interactions contribute to the binding strength: notably, an H-bond from CO_2 oxygen to the In2-O<u>H</u>, H-bonds from CO_2 oxygen to the benzene-H atoms (from the BDC linkers) and CO_2-carbon interactions with the BDC linker carboxylate-O atoms. (Note: throughout this text, <u>underlined atoms</u> indicate the atom with which that in question is interacting. The reason this nomenclature is used is because there are several unique O, H and C species within the MOF, and underlining the atom involved in the interaction as a part of its immediate connecting atoms allows for easier understanding of the interacting species.)

The final binding site, **B4-CO_2**, is the weakest of all binding sites identified within MIL-68-In. It is located within the hexagonal channel closest to In1 centers (see Figure 4-7). The key interaction involved in this binding site is the H-bond formed between a CO_2 oxygen and an In1-OH. Because this binding site is weaker, it will only appear at higher pressures (ie. Higher CO_2 loading) compared to the other three binding sites.

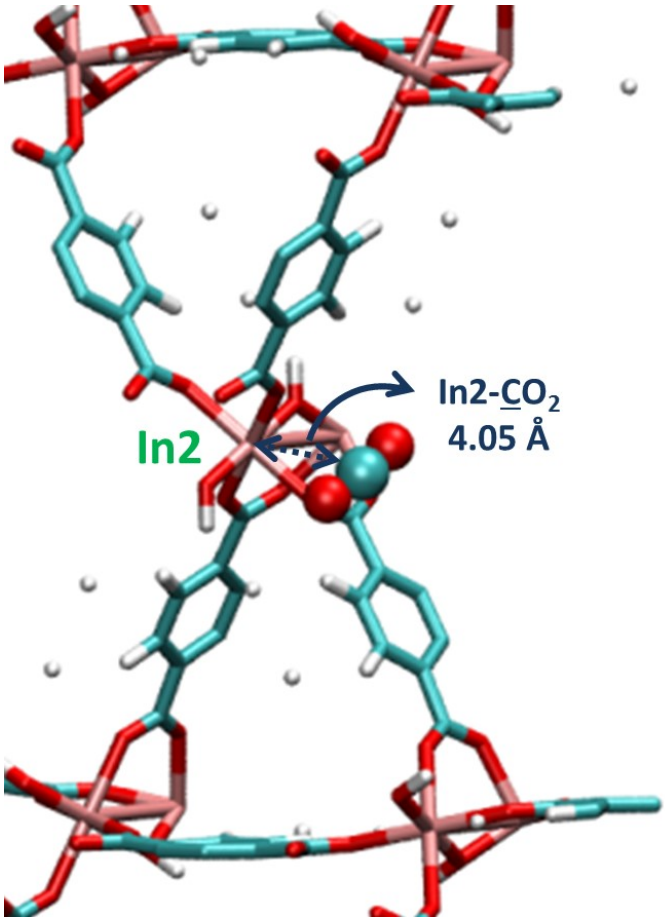

Figure 4-6. *DFT optimized* ***B3-CO_2*** *in MIL-68(In) with the In2-CO_2 distance noted (all other relevant interatomic distances are given in Table 4-2). T = 298 K, P = 1.0 bar. Black: CO_2 - C, Red: O, Green: In, Light blue: MOF C, White: H. In2 is indicated on the figure, and all other unmarked In atoms are In1.*

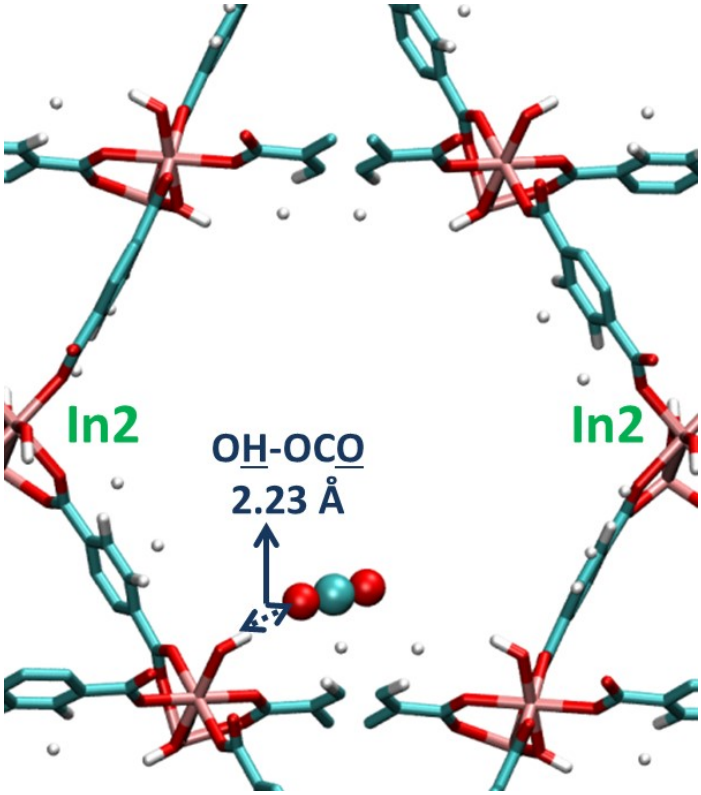

Figure 4-7. *DFT optimized* ***B4-CO₂*** *in MIL-68(In) with the OH-CO_2 distance noted (all other relevant interatomic distances are given in Table 4-2). T = 298 K, P = 1.0 bar. Black: CO_2 - C, Red: O, Green: In, Light blue: MOF C, White: H. In2 are indicated on the figure, and all other unmarked In atoms are In1.*

Table 4-1 shows relevant binding distances and energies for **B1-CO₂** and **B2-CO₂**, and Table 4-2 shows analogous information for binding sites **B3-CO₂** and **B4-CO₂**. It is of interest to note the difference in the composition of binding energy between different binding sites. For **B1-CO₂** and **B2-CO₂** found in the triangular pore, the electrostatic component of the total binding energy is less than 10%, meaning physisorption is mostly dictated by dispersion interactions. However, in the case of **B3-CO₂** and especially **B4-CO₂**, the electrostatic component accounts for 10% and 13% of total binding energy respectively. (Note: it was only possible to obtain energy decomposition for GCMC-derived binding sites, meaning that the binding energy electrostatic/noncovalent contributions will change after DFT optimization.) In terms of comparison with the SSNMR results obtained for ^{115}In and

^{13}C in Figures 4-2a) and 4-3, our results agree well with the experimental finding that CO_2 does not interact directly with the In centers. Indeed, adsorption of CO_2 has little effect on the ^{115}In spectrum as shown in Figure 4-2a) compared to the ^{115}In NMR spectrum obtained for the activated framework (Figure 4-2b)) because we find that all CO_2 binding sites identified interact mainly with nearby hydrogen atoms, whether from the BDC linker or the hydroxy groups connecting the infinite In1 or In2 chains.

Table 4-1. *Binding energy and distances to framework atoms for CO_2 binding sites found in MIL-68(In). Note that In1-OH is not accessible to CO_2 in the triangular pore. * Energy decomposition values from non-optimized GCMC results.*

B1-CO_2 (under linkers in Δ pore)	**GCMC 1.1**	**GCMC 1.2**	**DFT 1.1 (VASP)**	**DFT 1.2 (VASP)**
Shortest Distance of CO_2 Oxygen to In2-OH (Å)	4.93	4.58	4.88	4.37
Shortest Distance of CO_2 Oxygen to linker-benzene H (Å)	2.77	3.58	2.72	3.44
Shortest Distance of CO_2 atom to In1 (Å)	5.26	6.18	5.29	6.07
Shortest Distance of CO_2 atom to In2 (Å)	5.74	5.78	5.66	5.46
Total Binding Energy (kJ/mol)	33.2	33.2	25.1	22.4
Electrostatic Component of Binding Energy (%)*	9	9	-	-
Noncovalent Component of Binding Energy (%)*	91	91	-	-
B2-CO_2 (interstices formed in Δ pore)	**GCMC 2.1**	**GCMC 2.2**	**DFT 2.1 (VASP)**	**DFT 2.2 (VASP)**
Shortest Distance of CO_2 to In2-OH (Å)	4.77	3.24	4.69	2.21
Shortest Distance of CO_2 Oxygen to linker-benzene H (Å)	3.19	4.87	3.15	3.98
Shortest Distance of CO_2 atom to In1 (Å)	5.33	6.87	5.39	6.33
Shortest Distance of CO_2 atom to In2 (Å)	6.83	5.79	6.81	4.41
Total Binding Energy (kJ/mol)	32.4	32.4	22.7	29.2
Electrostatic Component of Binding Energy (%)*	7	7	-	-
Noncovalent Component of Binding Energy (%)*	93	93	-	-

Table 4-2. *Binding energy and distances to framework atoms for CO_2 binding sites found in MIL-68(In).*

B3-CO_2 (near In2)	**GCMC**	**DFT (VASP)**
Shortest Distance of CO_2 atom to In1 (Å)	8.61	8.51
Shortest Distance of CO_2 atom to In2 (Å)	4.43	4.05
Shortest Distance of CO_2 Oxygen to In2-OH (Å)	3.87	3.65
Shortest Distance of CO_2 Oxygen to linker-benzene H (Å)	2.86	2.66
Shortest Distance of CO_2 Carbon to linker-carboxylate O (Å)	3.48	3.22
Total Binding Energy (kJ/mol)	26.7	22.2
Electrostatic Component of Binding Energy (%)*	10	-
Noncovalent component of Binding Energy (%)*	90	-
B4-CO_2 (near In1)	**GCMC**	**DFT (VASP)**
Shortest Distance of CO_2 atom to In1 (Å)	5.05	4.57
Shortest Distance of CO_2 atom to In2 (Å)	11.15	11.16
Shortest Distance of CO_2 Oxygen to In1-OH (Å)	2.83	2.23
Shortest Distance of CO_2 to linker-benzene H (Å)	3.56	2.88
Total Binding Energy (kJ/mol)	24.5	19.9
Electrostatic Component of Binding Energy (%)*	13	-
Noncovalent component of Binding Energy (%)*	87	-
$C_{\text{binding site 2}}$ to $C_{\text{binding site 3}}$ Average Distance (Å)	-	8

4.3.2.2 Temperature dependant binding site analysis

Variable-temperature (VT) ^{13}C SSNMR experiments were carried out by the Huang group to study the temperature-dependance of CO_2 binding in MIL-68(In) (spectral data shown in Figure 4-8 below). VT SSNMR experiments are used to detect dynamic processes occurring on the NMR timescale. The experimental results show that with increasing temperature, the breadth (Ω) decreases gradually owing to enhanced motional averaging effects. The spectral data also show that at higher temperature such as 403 K (see Figure 4-8(c)), a peak which closely resembles that of free CO_2 (see Figure 4-8(d) for free CO_2 ^{13}C

SSNMR spectrum) dominates the spectrum, but the broad lineshape observed at lower temperatures (see Figure 4-8(a)) still shows a contribution to the full spectrum. To validate and shed further light on these observations, we carried out canonical MC simulations for CO_2 in MIL-68(In) at three different temperatures. For details on the canonical MC technique and MC techniques more generally, the reader is referred to section 2.1.3 found in Chapter 2.

The canonical MC-derived probability density plots shown in Figure 4-8 agree well with the findings provided by the VT ^{13}C SSNMR spectra for CO_2 adsorbed in MIL-68(In). At 150K, the spectral peak corresponding to CO_2 least resembles that of free CO_2 gas (also shown in Figure 4-8). This suggests that very little or no CO_2 is "free" within the pore, and that essentially all CO_2 molecules within the channel are in a bound state. We observe highly localized CO_2 probability densities at 150K (shown in Figure 4-8(a)) which indicates that CO_2 is in a free or mobile state over the course of the simulation at 150K. At 403K, a sharp ^{13}C peak demonstrates that with higher temperature, the CO_2 within the MOF has become essentially the same as that within the pure gas phase. In the corresponding canonical MC simulation at 403K, we observe almost entirely unrestricted CO_2 movement, as indicated by the diffuse probability density distribution. At 294K, a situation somewhere between that at 150K and 403K occurs for the NMR data as well as the canonical MC density plots.

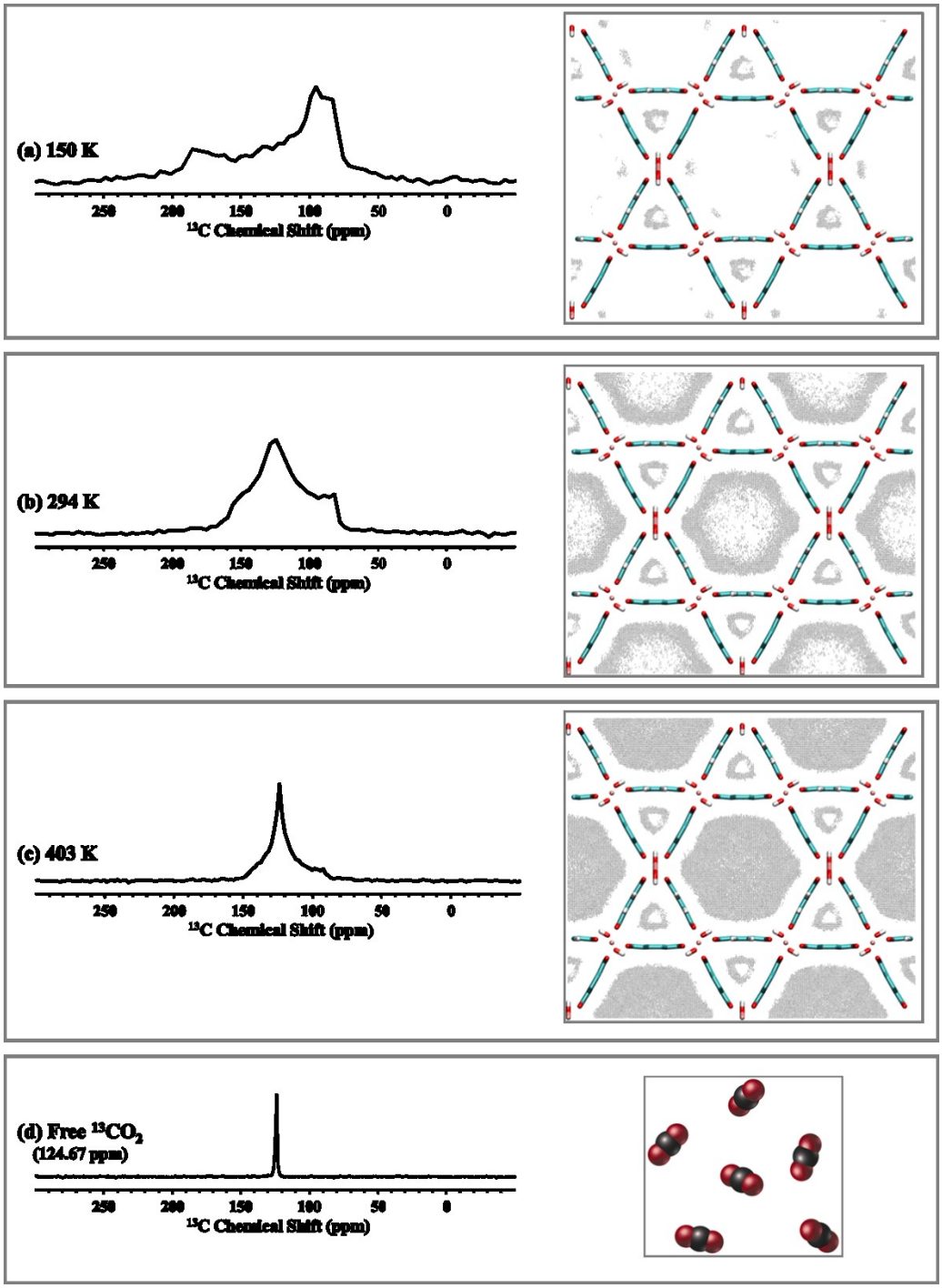

Figure 4-8. *^{13}C static SSNMR spectra for $^{13}CO_2$ in MIL-68(In) (left) and canonical MC isosurface plots of the probability density of the CO_2 center of mass (right) are shown here for simulations run at 150K (a), 294K (b) and 403K (c). The ^{13}C static spectrum for free CO_2 is shown for comparison in (d). All SSNMR and canonical MC data is based on the low loading of CO_2 in MIL-68(In) (1:0.1 In:CO_2). The same isovalue was used in order to compare the probability density plots on equal footing. All SSNMR and simulation data is collected at 1 bar.*

It should be noted here that, strictly speaking, although the SSNMR experiments were run with a fixed CO_2 loading for the different temperatures (0.1 CO_2/In), the quantity of CO_2 within the framework is in reality *not* fixed. Although the amount of CO_2 supplied to the MOF environment is the same at all temperatures, at lower temperatures (150K) gas uptake will be higher and at higher temperatures (403K) gas uptake will be lower. Indeed, GCMC simulations carried out at 150K, 293K and 403K predict loadings of 470, 125 and 24 CO_2 molecules respectively for the same 2x2x2 MIL-68(In) supercell. However, all our canonical MC simulations were run using the same number of CO_2 molecules (125 molecules in all cases). This is due to the fact that using a different loading for every different temperature MC simulation, although in accordance with the reality of the experimental conditions, will affect the probability density not only through greater freedom for CO_2 movement within the pores but also simply through differing concentration of CO_2 within the MOF. As an example, although at 403K CO_2 moves much more freely throughout the MOF channels, there is also nearly 20 times less CO_2 contained within the supercell compared to the 150K case, which will strongly affect the relative intensity of the probability distribution. In other words, the loading-dependant change in the probability distribution would overshadow the motion-dependant changes produced. This is the reason why the same number of CO_2 molecules was used for each one of the canonical MC simulations carried out.

4.3.2.3 Comparison with MIL-68(Al) CO_2 results

A combined experimental-computational study of MIL-68(Al) was conducted by Yang *et al.* in which they investigate CO_2 uptake and binding site localization (among other things) in this MOF, which is isostructural to MIL-68(In).[10] Because these two MOFs differ

essentially only in their metal center type and the analyses performed by Yang are similar to our own, we can draw some insightful comparisons.

The first interesting comparison relates to the position of hydrogens facing inside the hexagonal pore (which are those on the In1-OH-In1 infinite chain). Because hydrogens do not appear in the crystallographic files obtained from XRD, they must be added in before simulation and optimized using DFT. Yang et al. added the hydrogens on the Al1-O-Al1 and performed DFT optimization. They state that "*[…] For the inorganic part, the hydrogen atoms were included such that the O–H bonds were completely perpendicular to the Al–O–Al linkages*."[10] Although this is a chemically intuitive starting point for optimization of the hydrogen positions, with respect to the MIL-68(In) system it turns out not to be the most favourable hydrogen configuration. Optimization of the hydrogen positions at a starting point not entirely perpendicular to the In-O-In linkage provides a different DFT-optimized structure around 6 kJ/mol lower in energy than when the Hs are perpendicular to the In-O-In chain. This tells us that a local minimum energy appears when the hydroxy groups are perpendicular to the In-O-In chain, but the global minimum exists elsewhere. It should be noted that these conclusions were found for the MIL-68(In) system, and so it is possible they are not applicable to the MIL-68(Al) system. However, the authors state that they chose the perpendicular position for H atoms as their starting point, indicating that the most favourable configuration of the framework H atoms was not thoroughly investigated. The difference in energy between the perpendicular and more favourable non-perpendicular configuration of framework H suggests that the H can oscillate relatively easily between these two conformations (and potentially others). Because our calculations require the use of a rigid host, this is not an effect we could include in our simulation. It is likely that any movement

of H does not significantly affect guest adsorption behaviour (see next paragraph), and we are confident that we have selected the lowest energy, best possible configuration for our static model.

The second observation of interest relates to the different binding observed near M1 and M2 (where M=In, Al) in both MOFs. In the paper by Yang *et al.*, little or no distinction is made between non-equivalent sites Al1 and Al2. There is undoubtedly a difference between the two binding sites, as evidenced by the probability distribution shown in Figure 4-9 (taken from reference 43), which they do not comment on in the paper. One can distinguish the probability density of CO_2 center of mass (COM) whether at Al2 (in the center of the figure) or Al1. It appears from Figure 4-9 that CO_2 has a lower probability density near Al2 than near Al1. It is interesting to note that MIL-68(In) shows the opposite trend, as shown in Figure 4-9. We ran a GCMC simulation with a hydrogen DFT-optimized MIL-68(In) where the Hs are perpendicular to the In-O-In chains, and found that the GCMC probability density distribution remains the same. In other words, the perpendicular hydrogens do not significantly affect the probability density distribution of CO_2 in MIL-68(In), and are not the cause for the differences observed between probability density distributions in MIL-68(In) and MIL-68(Al). The difference is therefore likely attributable to the different metal centers in MIL-68(Al) and MIL-68(In). Nonetheless, it is an interesting difference to highlight.

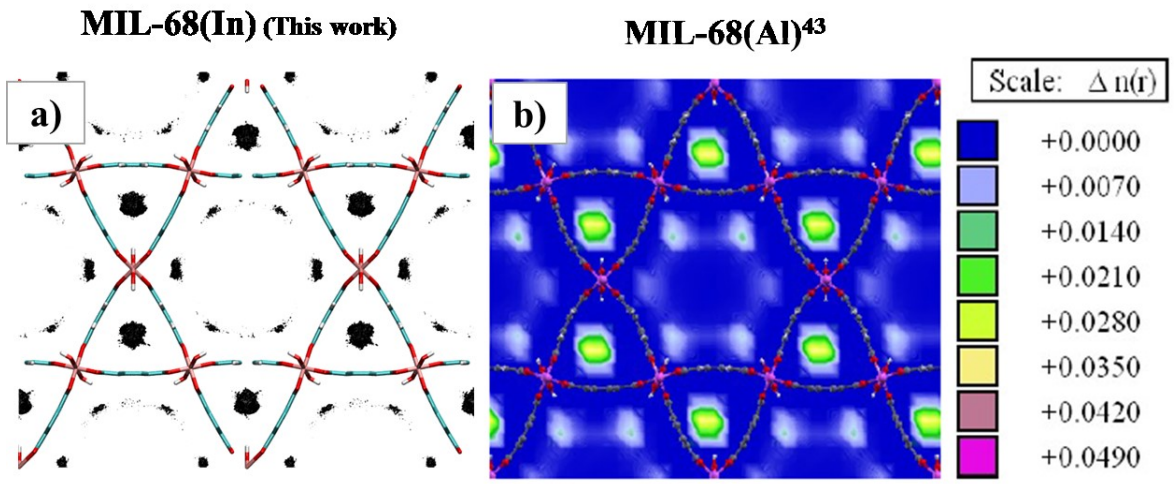

Figure 4-9. *GCMC-derived probability density plots for CO_2-COM adsorption in MIL-68(In) (a) and MIL-68(Al) (b). Both results are obtained at 1 bar, but a) was simulated at 298K and b) was simulated at 303K. Plot b) was taken from the SI of reference 43.*

4.3.2.4 Molecular Dynamics

The dynamical aspects of CO_2 binding within MIL-68(In) was studied using molecular dynamics (MD). GCMC simulations provide information on binding site location and strength within the host, but they do not give any information on how the binding sites interact with the host through time, as they only give equilibrium averaged information. Of particular interest for this MOF would be whether a single CO_2 can switch between binding sites **B1-CO_2** and **B2-CO_2** in the triangular channel, and similarly whether another CO_2 binding site can switch between binding sites **B3-CO_2** and **B4-CO_2** within the larger hexagonal channel.

MD studies were carried out for 40 ns at 293K constant temperature and constant volume (see section 4.2.3 for the default parameters used for all MD simulations throughout this chapter). The loading of CO_2 used for the MD simulation was the loading as determined from an equilibrated GCMC simulation at 293K, 1 bar for the same system (124 molecules

for a 2x2x2 unit cell MD simulation cell size, which corresponds to around 16 CO_2 molecules/unit cell, or 4.36 mmol CO_2/g MIL-68(In)).

Select results from the MD simulation are shown in Figures 4-10,11 and 12. Of note is that when tracking a single CO_2 throughout the course of the simulation, both binding sites **B1-CO_2** and **B2-CO_2** (triangular channel) and binding sites **B3-CO_2** and **B4-CO_2** (hexagonal pore) respectively are visited frequently by the same molecule. (Note: there are no connective channels between the triangular and hexagonal channels, so a single CO_2 will be restricted to either one of the two channel spaces). Here, an analysis of trajectories over 2.5 ns for three CO_2 molecules in the triangular channel (**B1-CO_2** and **B2-CO_2**) and three CO_2 molecules in the hexagonal channel (**B3-CO_2** and **B4-CO_2**) for a total of six CO_2 molecule trajectories will be provided.

In the case of the triangular channel, DFT binding energies as calculated from section 4.3.2.1 show that the binding energy for binding pockets **B1-CO_2** and **B2-CO_2** can vary up to ~ 5 kJ/mol depending on the orientation of the molecule within the pocket. However the ranges for binding pockets **B1-CO_2** (22.4 to 25.1 kJ/mol) and **B2-CO_2** (22.7 to 29.2 kJ/mol) are similar, showing that there is likely not to be a clear preference for one binding pocket over the other. The longest residence time for a CO_2 molecule in **B1-CO_2** was ~ 638.5 ps and ~ 721.5 ps for **B2-CO_2** (residence times illustrated in Figure 4-10). For both **B1-CO_2** and **B2-CO_2**, the shortest residence time for a CO_2 molecules was somewhere between 2.5 – 5 ps, and in such cases the CO_2 is just "passing through" either pocket **B1-CO_2** or **B2-CO_2** to jump from a site **B2-CO_2** to another site **B2-CO_2**/site **B1-CO_2** to another site **B1-CO_2**. For two of the three trajectories which were tracked, the CO_2 molecule regularly spent > 500 ps at either **B1-CO_2** or **B2-CO_2**, but for the other CO_2 molecule which was tracked, the

longest time spent in either binding site is only ~ 66.5 ps. As shown in Figure 4-11, this has to do with the initial loading configuration as determined from GCMC run at 293K and 1 bar of the triangular pore. In the case of the triangular channels with long residence times, the triangular pore loading equals one molecule per site within the simulation cell size used (for the 2x2x2 simulation cell, there are 8 sites per channel,-see Figure 4-11), however in the short residence time-channel, the loading is less than one molecule per site (only 6 molecules loaded). This demonstrates that the loading of the triangular pore has a significant impact on the residence time for a molecule within either **B1-CO_2** or **B2-CO_2**. Incomplete CO_2 loading results in unoccupied sites, which facilitate hopping between different sites for a same CO_2 molecule. It should also be noted that the MD trajectories show no more than one molecule occupying one binding site at one time. In any event, an average over the three trajectories still yields an average residence time of ~84 ps and ~120 ps for **B1-CO_2** and **B2-CO_2** respectively. Given that a more energetically favourable binding conformation was identified for **B2-CO_2** (BE = 29.2 kJ/mol), it is not surprising to find a slightly higher average residence time for **B2-CO_2**, while identifying relatively similar average residence times is also a reasonable finding since a configuration within **B1-CO_2** as well as **B2-CO_2** are very close in energy.

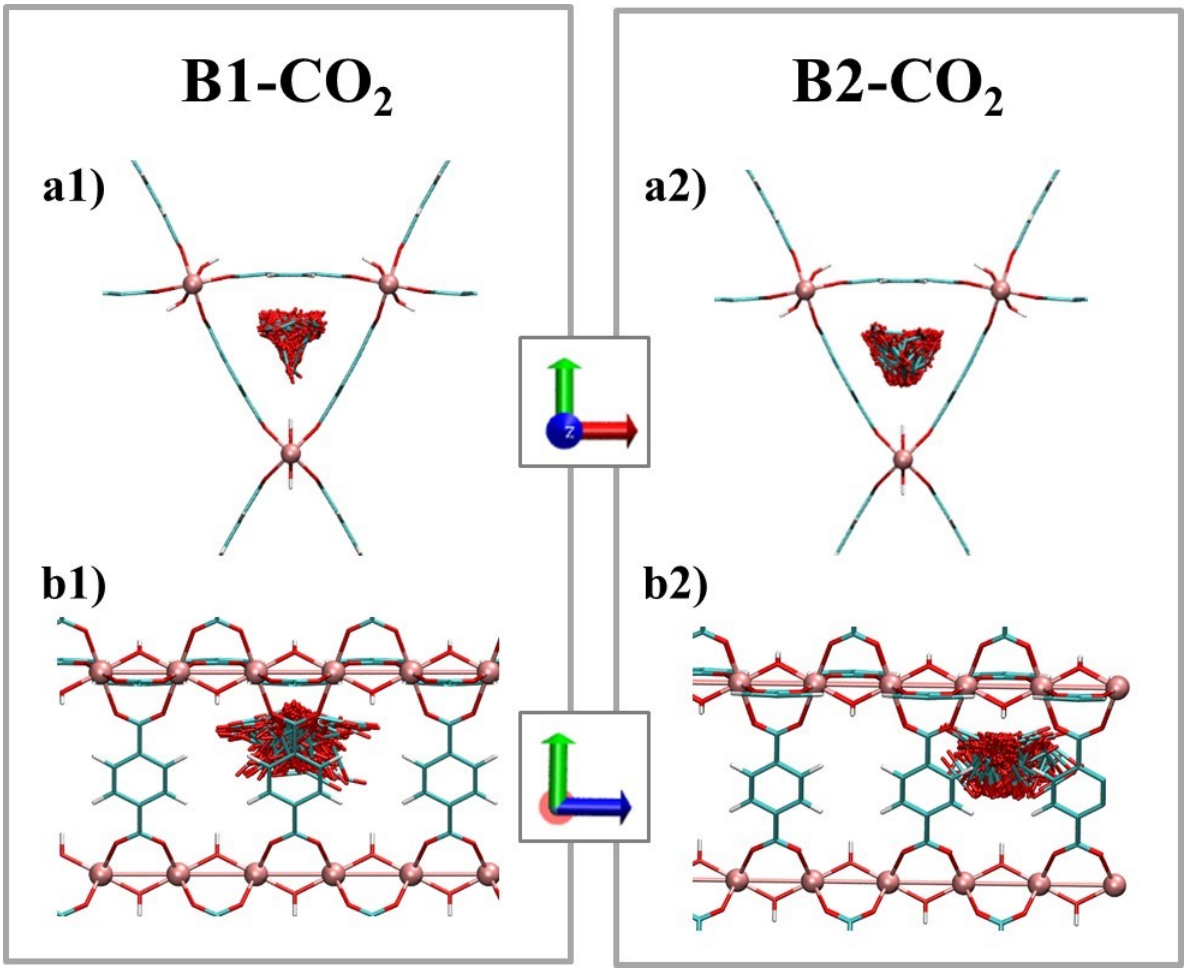

Figure 4-10. *For* ***B1-CO₂*** *and* ***B2-CO₂****, a front view of the triangular channel is shown in a1) and a2) respectively. Within the triangular pore, a portion of the trajectory for a single CO_2 molecule (shown every 0.5 ps) for the longest residence time seen is shown. This corresponds to 638.5 ps for* ***B1-CO₂*** *(a1) and 721.5 ps for* ***B2-CO₂*** *(a2). b1) and b2) show a side-view of the triangular channel including the same portion of the trajectory shown in a1) and a2) for* ***B1-CO₂*** *and* ***B2-CO₂****, respectively. As was found through GCMC binding site analysis,* ***B1-CO₂*** *(b1) remains under the linkers, whereas* ***B2-CO₂*** *(b2) remains within the interstice formed by the linkers.*

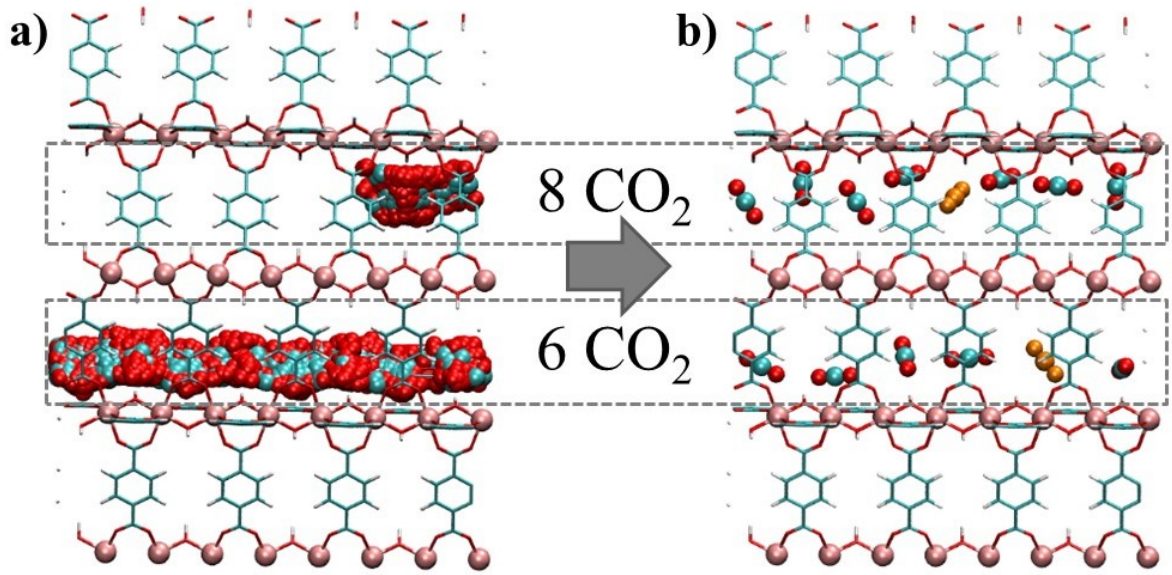

Figure 4-11. *In a), an ab plane representation of MIL-68(In) containing the trajectories of two different CO_2 molecules within two different triangular channels over the same 500 ps period (ie. The MD simulation results shown for both CO_2 molecules are from 0 → 500 ps) is shown. An image of the CO_2 molecule's position is shown every 0.5 ps. In b), the same representation of the framework is shown but with the loading of each triangular channel corresponding to the representation shown in a). Orange CO_2 molecules in b) indicate the same CO_2 molecules which were tracked in a) at some point throughout the total 2.5 ns trajectory.*

Analysis of the dynamic behaviour of the CO2 molecules in binding regions **B3-CO_2** and **B4-CO_2** of the hexagonal channel shows a different behaviour compared to **B1-CO_2** and **B2-CO_2**. The hopping from one binding site to another was so frequent, only the first 250 ps needed to be characterized to provide a representative sample of the dynamics within the channel. The binding energies for **B3-CO_2** (22.2 kJ/mol) and **B4-CO_2** (19.9 kJ/mol) are lower compared to the range of binding energies found for pockets **B1-CO_2** and **B2-CO_2** (differences range from 0.2 to 9.3 kJ/mol), and residence times are shorter for **B3-CO_2** and **B4-CO_2** than for **B1-CO_2** and **B2-CO_2**. The longest residence time for **B3-CO_2** is ~ 45.5 ps and shortest residence time is ~ 2 ps. The average residence time over all three trajectories is ~ 17 ps (with a mode of ~ 5 ps). The longest residence time for **B4-CO_2** is ~ 28.5 ps and the shortest residence time observed was < 1 ps. The average residence time over all three trajectories is ~ 8 ps (with a most repeated value (mode) of ~ 5 ps). Since **B3-CO_2** has a

stronger binding energy than **B4-CO_2**, it is no surprise to see the trend in residence times observed here. See Figure 4-12 for an illustration of residence times for **B3-CO_2** and **B4-CO_2**. From the longest residence time observed for **B4-CO_2** (Figure 4-12 c)), the binding is evidently weaker compared to that of **B3-CO_2** (Figure 4-12 b)), as it tends easily to "rock" from the neighbouring **B4-CO_2** to the neighbouring **B3-CO_2** while still remaining within the **B4-CO_2**. **B3-CO_2** on the other hand remains much more localized throughout the longest residence time observed.

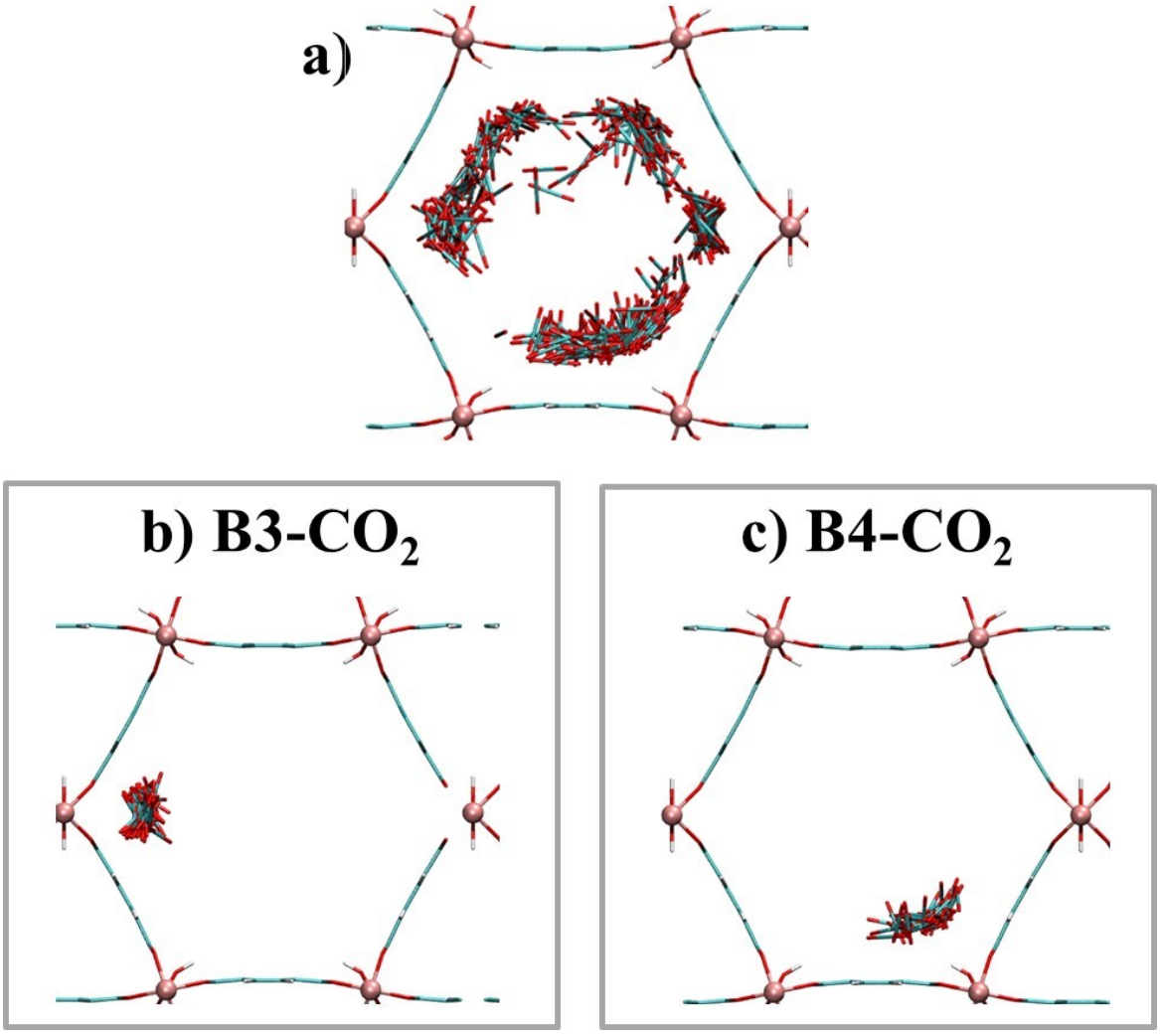

Figure 4-12. *In a), a view of a MIL-68(In) hexagonal channel along the c axis shows a trajectory for a single CO_2 molecule over the course of the first 250 ps of simulation. Snapshots of the CO_2 molecule are taken every 0.5 ps. The partial trajectories corresponding to the longest residence time for* ***B3-CO₂*** *(45.5 ps) (b) and* ***B4-CO₂*** *(28.5 ps) (c) are also shown, where snapshots of CO_2 are taken every 0.5 ps.*

This study demonstrates preliminary findings regarding the dynamics of CO_2 in MIL-68(In). Especially since the effect of dynamics are capture by ^{13}C SSNMR spectra, we wish to carry out more rigorous quantitative studies on the dynamics of guests in the framework. This includes study of the mean angle of CO_2 with respect to the binding sites, mean and average residence times, switching rates and possibly even studies of the mobility of CO_2

throughout the different channels (ie. Diffusion) in order for a thorough analysis to be carried out. Details on future work to be carried out on this system are offered in Chapter 5.

4.3.3 DMF Binding Site Analysis

GCMC simulation results are shown for DMF in MIL-68(In) in Figures 4-13 and 4-14. There are three distinguishable binding sites (referred to as **B1-DMF**, **B2-DMF** and **B3-DMF** in this section). Two are found in the hexagonal channel (**B1-DMF** and **B3-DMF**) and another in the triangular channel (**B2-DMF**). Of the hexagonal channel binding sites, one is found near the In1 SBU (**B1-DMF**) and another is found near the In2 SBU (**B3-DMF**). Of the three binding sites, **B1-DMF** and **B2-DMF** have a significantly higher probability density. In terms of **B3-DMF**, it can be seen from Figure 4-13 that the highest probability density is associated with the grey carbons, which are the CH_3 carbons on DMF. The position of the CH_3 carbons suggest that there is an interaction with the In2-OH-In2 portion of the framework. For all DMF binding sites (as for all CO_2 binding sites), there is no strong interaction with the metal center.

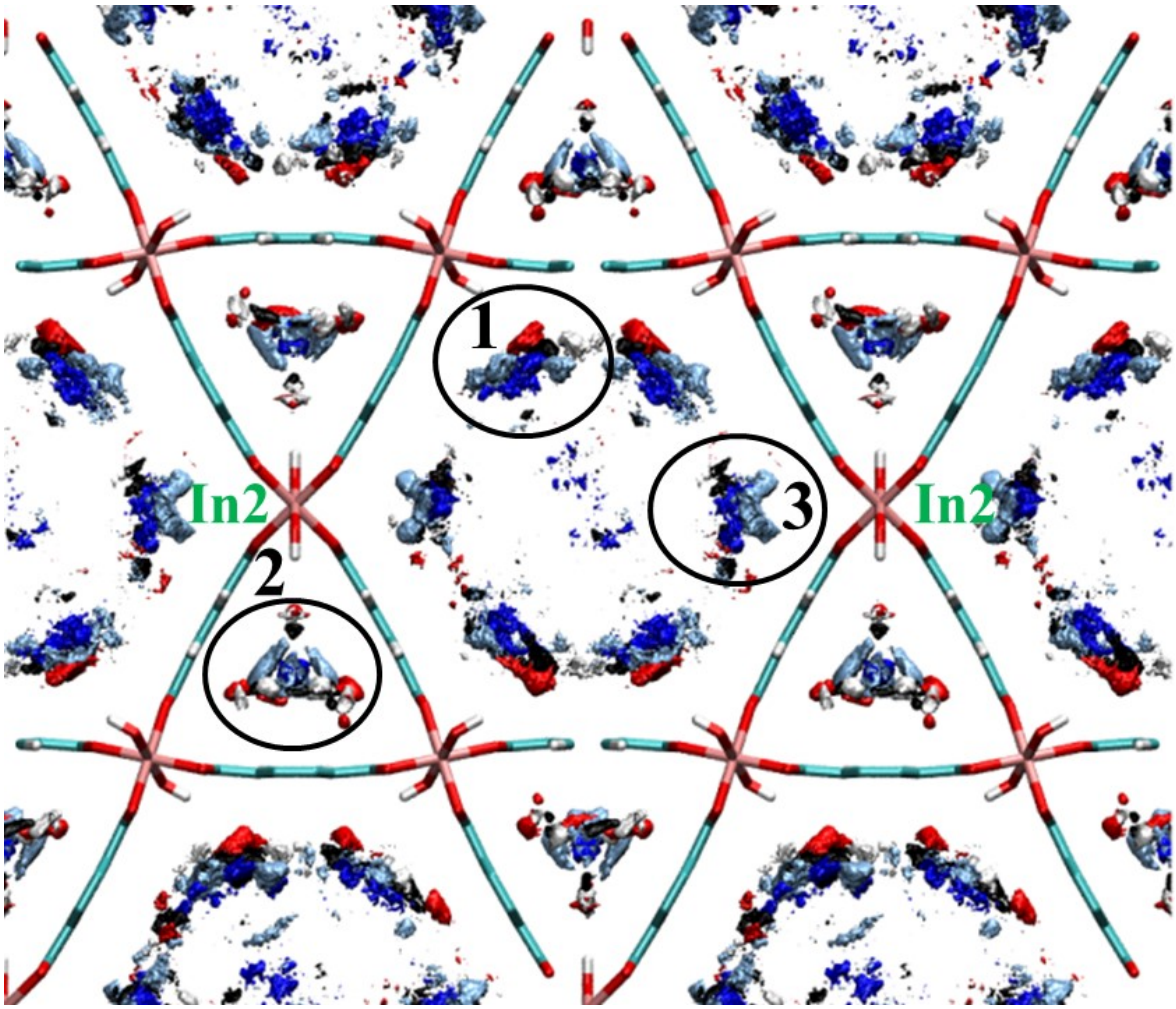

Figure 4-13. *GCMC-derived isosurface plot of the DMF probability density in activated MIL-68(In). Isovalue = 0.02, T = 298 K, P = 1.0 bar. Blue: DMF-N, Red: O, Black: DMF-C (from C=O), Grey: DMF-C (from CH_3), Pink: In, Light blue: framework C, White: H. In2 are indicated on the figure, and all other unmarked In atoms are In1.*

The probability density persists at higher isovalues for DMF in the triangular channel (**B2-DMF**) compared to that of DMF in the hexagonal pore (**B1-DMF** and **B3-DMF**). This could mean it is more likely for these binding sites to be occupied first (at lower pressures) than binding sites found in the hexagonal pore. In Figure 4-14, a possible configuration of DMF in site **B2-DMF** is shown in the triangular channel. Like with CO_2 binding sites, the so-called "sites" should more so be considered binding pockets, in which the DMF molecule can be found in several favourable binding configurations within this binding region. The

orientations in Figure 4-14 are of high probability. In it, a DMF oxygen interacts with a linker-benzene H atom.

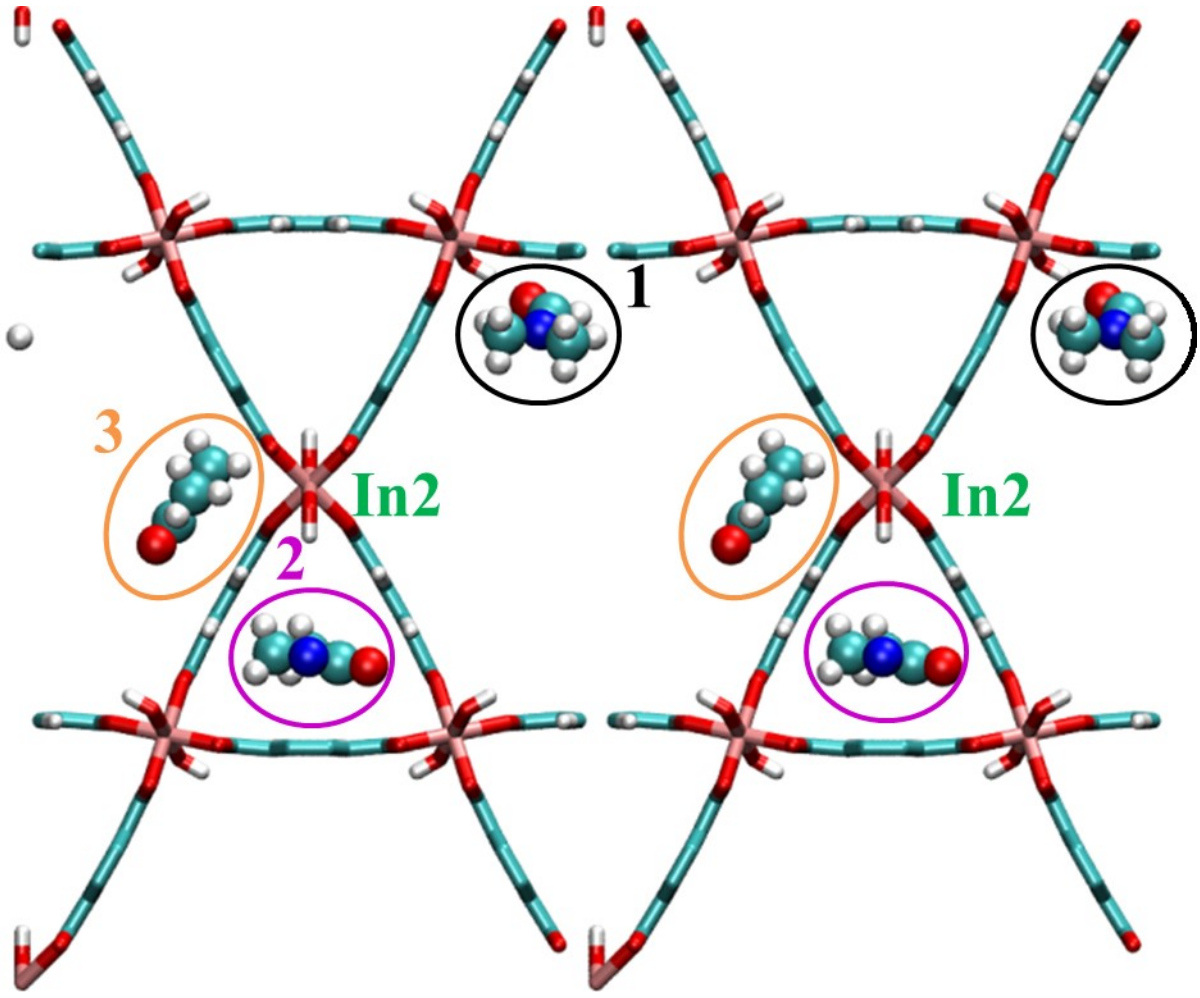

Figure 4-14. *DFT optimized DMF binding sites* ***B1-DMF***, ***B2-DMF*** *and* ***B3-DMF*** *found in MIL-68(In). Blue: DMF-N, Red: O, Pink: In, Light blue: C, White: H. In2 are indicated on the figure, and all other unmarked In atoms are In1.*

For the hexagonal channel binding site near In1 (**B1-DMF**), a hydrogen bond forms between the DMF oxygen and the hydrogen from the In1-OH-In1 chains. This corresponds well with findings related to CO_2, as it is also the behaviour observed when CO_2 is found near the In1 SBU (**B4-CO_2**). This binding site turns out to be the strongest among all the DMF binding sites found.

The weakest DMF binding site, **B3-DMF**, is located near In2 in the hexagonal channel. Once again, analogous to **B3-CO_2** which also binds near In2, several weak interactions contribute to binding. Notably, the DMF-methyl group hydrogens interact with a BDC linker carboxylate oxygen as well as the In2-OH depending on their spatial orientation, and the DMF-N interacts with another BDC linker carboxylate oxygen. Figure 4-15 depicts the way in which DMF interacts with surrounding atoms for all three binding sites. Table 4-3 contains all relevant interatomic distances for the DMF binding sites found within MIL-68(In), as well as binding site energies. For **B2-DMF**, the binding site found in the triangular channel, the electrostatic contribution to the binding energy is negative (-2.9%). This indicates a binding site which is highly favoured through dispersion interactions but non-binding through electrostatic interactions.

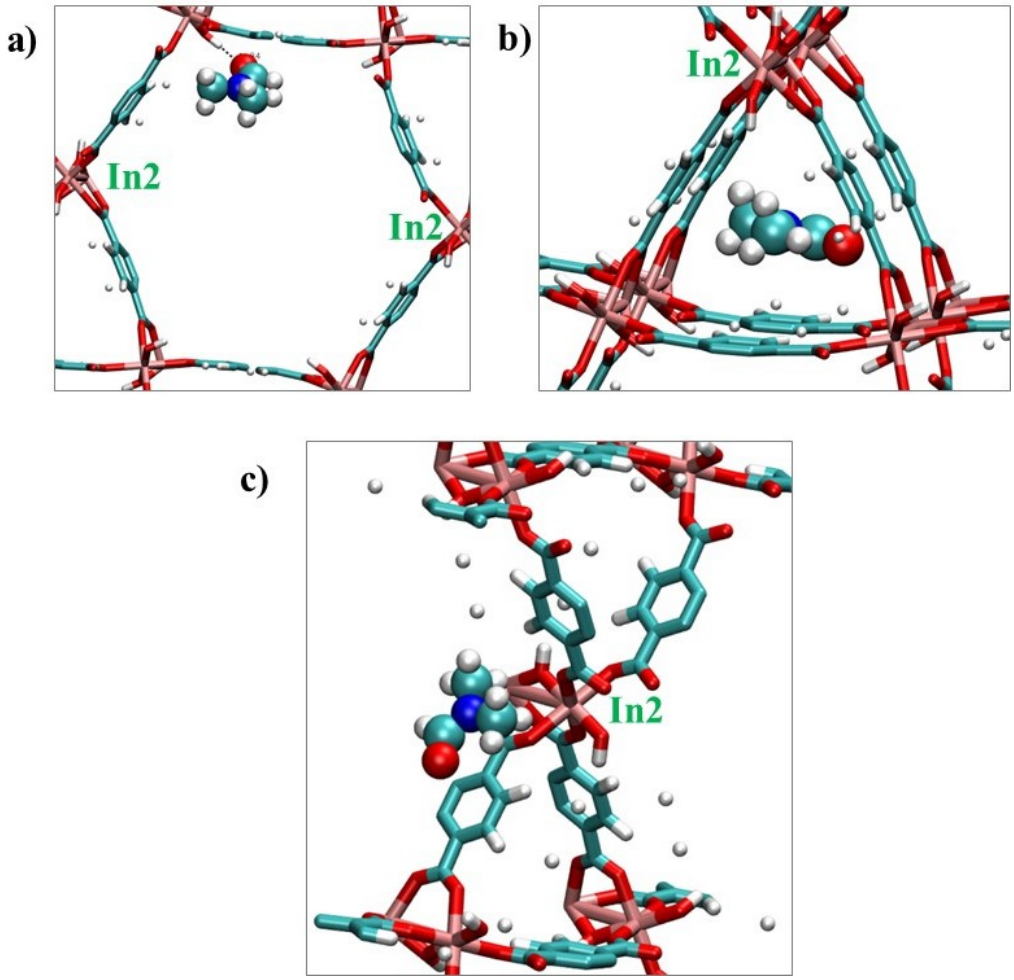

Figure 4-15. *Enhanced views of DFT optimized DMF binding sites* ***B1-DMF*** *(a),* ***B2-DMF*** *(b) and* ***B3-DMF*** *(c) found in MIL-68(In). Blue: DMF-N, Red: O, Pink: In, Light blue: C, White: H. In2 are indicated on the figure, and all other unmarked In atoms are In1.*

Table 4-3. *Binding energy and distances to framework atoms for DMF binding sites found in MIL-68(In).*

B1-DMF (Hexagonal Pore)	GCMC	DFT
Shortest Distance of DMF Oxygen to In1-OH (Å)	2.65	1.84
Shortest Distance of DMF CH_3 Hydrogen to linker-carboxylate O (Å)	2.76	2.51
Shortest Distance of DMF atom to In1 (Å)	4.87	4.16
Shortest Distance of DMF atom to In2 (Å)	8.83	8.60
Total Binding Energy (kJ/mol)*	54.2 (17.5%)	76.6
B2-DMF (Triangular Pore)	GCMC	DFT
Shortest Distance of DMF Oxygen to linker-benzene H (Å)	2.69	2.46
Shortest Distance of DMF to In2-OH (Å)	4.57	4.62
Shortest Distance of DMF atom to In1 (Å)	4.55	4.57
Shortest Distance of DMF atom to In2 (Å)	6.13	5.86
Total Binding Energy (kJ/mol)*	72.0 (-2.9%)	67.7
B3-DMF (Hexagonal Pore)	GCMC	DFT
Shortest Distance of DMF CH_3 Hydrogen to linker-carboxylate O (Å)	3.07	2.64
Shortest Distance of DMF CH_3 Hydrogen to In2-OH (Å)	3.36	2.27
Shortest Distance of DMF-N to linker-carboxylate O (Å)	4.25	3.27
Shortest Distance of DMF atom to In2 (Å)	3.72	3.36
Shortest Distance of DMF atom to In1 (Å)	7.62	7.35
Total Binding Energy (kJ/mol)*	41.8 (24.7%)	49.0

** Percentages included in parentheses next to the GCMC-derived binding energies are the binding energy decomposition results for the electrostatic contribution to binding, and are given in %.*

Comparisons between the different CO_2 and DMF binding sites found in MIL-68(In) can provide valuable insight. Although the locations of the binding sites were similar for both guests, the binding energies found for CO_2 binding sites (Tables 4-1 and 4-2) were all significantly lower than the binding energies found for DMF (Table 4-3). From the DMF and CO_2 probability density plots (Figures 4-13 and 4-4 respectively), the strongest DMF binding site (**B1-DMF** shown in Figure 4-15a)) has a higher probability density near In1 than In2 while the strongest hexagonal channel CO_2 binding site (**B3-CO_2** shown in Figure

4-6) shows the opposite trend, showing a higher probability density near In2 than In1. In terms of comparison of dipole moment, CO_2 does not have one at all, whereas the dipole moment for DMF is 3.82 Debye, meaning the CO_2-related hydrogen-bond interactions will be relatively weak in comparison to equivalent interactions found for DMF. It also goes without saying that DMF is a significantly larger guest (12 atoms) than CO_2 (3 atoms), meaning that there are greater possibilities for interaction of several DMF atoms with the framework. This is why the ^{115}In NMR experiments carried out by the Huang group only mostly detect the stronger framework-DMF interactions, shown clearly by the significant change in the In1 signal from solvated to activated MIL-68(In) (changes in ^{115}In signal shown in Figures 4-2c) and 4-2b)). For the comparatively weak CO_2 binding sites, the ^{115}In NMR spectrum shows little change from the activated MOF to the CO_2 loaded MOF (Figures 4-2b) and 4-2a)), but the small changes in the spectral data do appear to be focused on the In2 centers, which is consistent with the strongest binding site found in the hexagonal pore **B3-CO_2**.

4.3.4 Conclusion

GCMC simulations and DFT calculations show no direct interaction between CO_2 and the In centers found in MIL-68(In), which is in agreement with the ^{115}In SSNMR results collected by the Huang group. We observe four CO_2 binding sites with different types of interaction (listed in order decreasing binding strength): **B1-CO_2** which is found in center of the triangular channel, and is found directly beneath the linkers; **B2-CO_2** which is also in the center of the triangular channel, but instead of being directly under the linkers, is found in the interstices formed by the linkers; **B3-CO_2** which is found near In2 SBUs and interacts with several atoms surrounding the In2 center, mostly through H-bonds; finally **B4-CO_2**

which will only appear at higher pressures, which H-bonds directly with the OH group connecting the infinite In1 chain. **B1-CO_2** and **B2-CO_2** are less localized than **B4-CO_2** and especially **B3-CO_2**. Based on the ^{13}C SSNMR data collected by the Huang group, there should be three unique binding sites within the MOF. Although we find four binding sites, **B4-CO_2** is weak in comparison to the other binding sites. This may explain why only three are observed in the SSNMR results. Our GCMC results were compared with those found in another study for an isostructural MOF, MIL-68(Al). From their probability density plots, it appears that our hexagonal channel binding sites show the opposite trend in terms of probability. This suggests that the metal center identity may play some role in this change.

MD simulations provided information on the CO_2 dynamics, which are challenging to ascertain using SSNMR alone. Average residence times were obtained for all binding sites (**B1-CO_2:** ~84 ps, **B2-CO_2:** ~120 ps, **B3-CO_2:** ~ 17 ps **B4-CO_2:** ~ 8 ps) and match the relative trend in binding energies. Of particular interest was the discovery that the loading of the triangular channel could greatly change the hop rate of a CO_2 molecule from site **B1-CO_2** to **B2-CO_2** and vice versa: indeed, residence times were around 10 times longer when every binding site in the 8-site channel was occupied vs. when two of all 8 sites were vacant.

A series of canonical MC simulations were run to observe the effect of a change in temperature on the distribution of probability of adsorbed CO_2 within the MOF. At 403K, the CO_2 moves freely within the MOF and is less restricted to the binding sites we identified. At a low temperature of 150K, the CO_2 molecules are much more restricted, and over the course of the canonical MC simulation mostly occupy the binding sites we identified using GCMC. At a moderate temperature of 293K, a situation somewhere between the two

previously described is observed. These simulation results all match temperature-dependant ^{13}C SSNMR-spectra collected by the Huang group.

A combined GCMC and DFT investigation of N,N-dimethylformamide (DMF) was carried out. For DMF, three major binding sites are identified. Two binding sites (**B1-DMF** and **B3-DMF**) are found in the hexagonal channel, and are similar to the **B3-CO_2** and **B4-CO_2** sites found for CO_2. Interestingly, the DMF binding site (**B1-DMF**) which is analog to the **B4-CO_2** site found for CO_2 is the strongest of all, whereas **B4-CO_2** is the weakest of among all CO_2 binding sites found. The other DMF binding site is found in the triangular channel (**B2-DMF**), and the carbon on DMF interacts with oxygen atoms which interconnect In2 chains. A comparison of the strongest CO_2 hexagonal channel binding site (**B3-CO_2** shown in Figure 4-6) and the strongest DMF binding site (**B1-DMF** shown in Figure 4-15a) found in MIL-68(In) shows that the binding energy is significantly stronger for the DMF binding site, and the strongest DMF binding site has a higher probability density near In1 while the strongest hexagonal pore CO_2 binding site shows a higher probability density near In2. This is consistent with the ^{115}In NMR spectral data (shown in Figure 4-2), as greater changes are observed in the In1 signal from the as-made (DMF-solvated) to activated MIL-68(In).

4.4 $Ba_2TMA(NO_3)$

GCMC and MD simulations in addition to DFT calculations are performed to better understand the interactions of DMF and CO_2 with $Ba_2TMA(NO_3)$, a MOF with non-equivalent Ba metal SBUs. As both guests investigated were suspected of interacting quite strongly with the Ba centers, computational techniques (including Bader charge differences and charge density difference) were employed to better grasp whether any charge transfer interactions were at play. Throughout this section, simulation results are compared to the SSNMR spectral data acquired by the Huang group when possible.

4.4.1 Structure and SSNMR Analysis

$Ba_2TMA(NO_3)$ is a MOF first synthesized and characterized by Foo *et al.* which contains Ba metal SBUs, trimesic acid organic linkers (TMA, or benzene-1,3,5-tricarboxylic acid) and NO_3^- ions which when assembled form one-dimensional, three-leaf clover shaped channels with a widest dimension of 13 Å and narrowest dimension of 6.5 Å.[13] Prior to activation, DMF binds to certain Ba centers, but TGA experiments show it to be removed once the MOF is appropriately heated. In the paper by Foo *et al.*, characterization efforts are focused on the pre-activated MOF, but Professor Huang's powder XRD experiments show the pre-activated and activated structures to be essentially identical (see Figure 4-16 below). This MOF is one of the few reported I^3O^0 type frameworks, which refers to Ba-O-Ba bonds which extend in 3 dimensions, whereas generally they will have connectivity of a 0 (inorganic node), 1 (inorganic chain) or 2 (inorganic plane)-dimensional nature. In the work by Foo *et al.*, $Ba_2TMA(NO_3)$ showed promise for separation of CO_2 from CH_4 in both equilibrium and breakthrough experiments, and a very recent study shows that the MOF may

also be of interest for base-catalyzed reactions, especially when the MOF undergoes specific thermal pre-treatment conditions for controlled defect formation.[14]

Like MIL-68(In), this MOF has two non-equivalent Ba metal SBUs which will be referred to as Ba1 and Ba2. However, in this case the Ba centers differ in their coordination, not just in their bond lengths which was the case for MIL-68(In): Ba1 is coordinated with five different TMA linkers (bidentate bonds are formed between Ba1 and three of the TMA linkers and monodentate bonds are formed between two of the TMA linkers and Ba1) for a total of 8 coordination points. Prior to activation, DMF can also bind to Ba1 for a total of 9 coordination points. As for Ba2, it also has 8 coordination points, though they are different: 4 bonds are formed through two bonds to each of two NO_3^- groups and another 4 through 4 COO^- singly coordinating TMA linkers. From the single-crystal XRD results in the work by Foo *et al.*, the distance of DMF-O to Ba2 centers was longer (3.189 Å) than that for DMF- O and Ba1 (2.955 Å), but it is noted that despite this longer distance, Ba2 may also bind to two DMF molecules, meaning it could also be 10-coordinate when solvated.[13] The framework structure and differences in coordination of the metal SBUs are shown below in Figure 4-17.

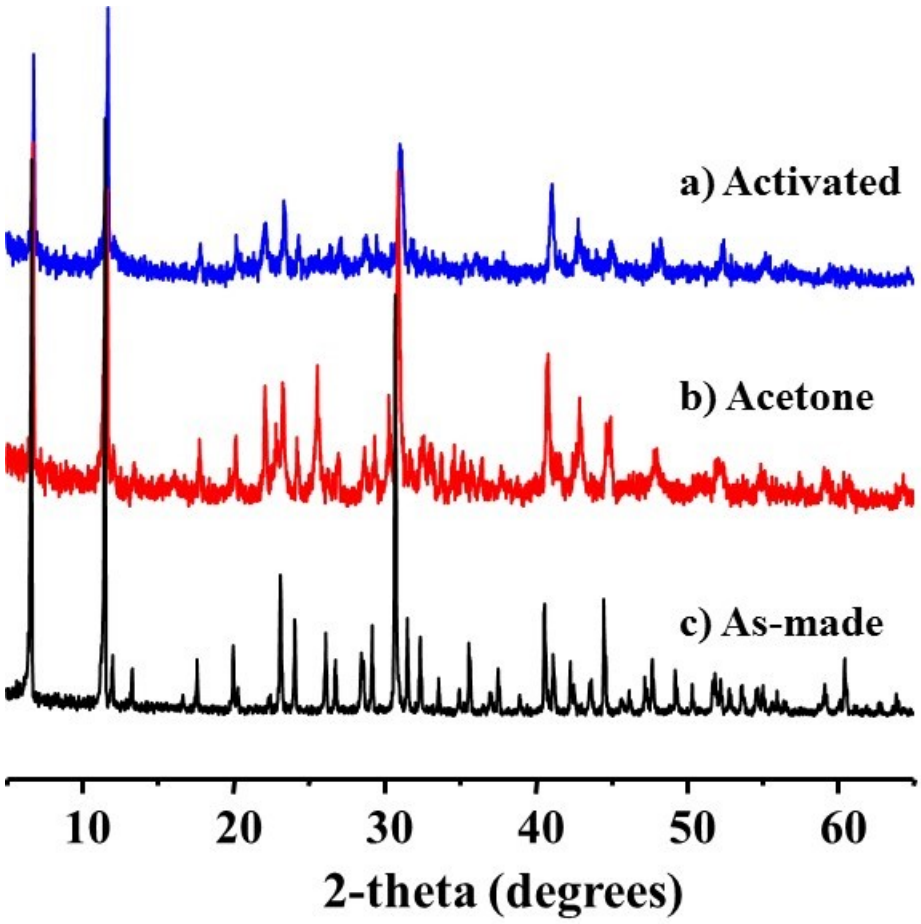

Figure 4-16. *Experimental Powder X-ray Diffraction (PXRD) results for activated $Ba_2TMA(NO_3)$ (a) $Ba_2TMA(NO_3)$ as-made, which contains the DMF solvent (c) and $Ba_2TMA(NO_3)$ containing acetone solvent (b). The acetone solvated structure PXRD is included as solvent exchange of DMF with acetone in necessary for activation of the MOF. Data acquired and provided by Professor Yining Huang (Western University).*

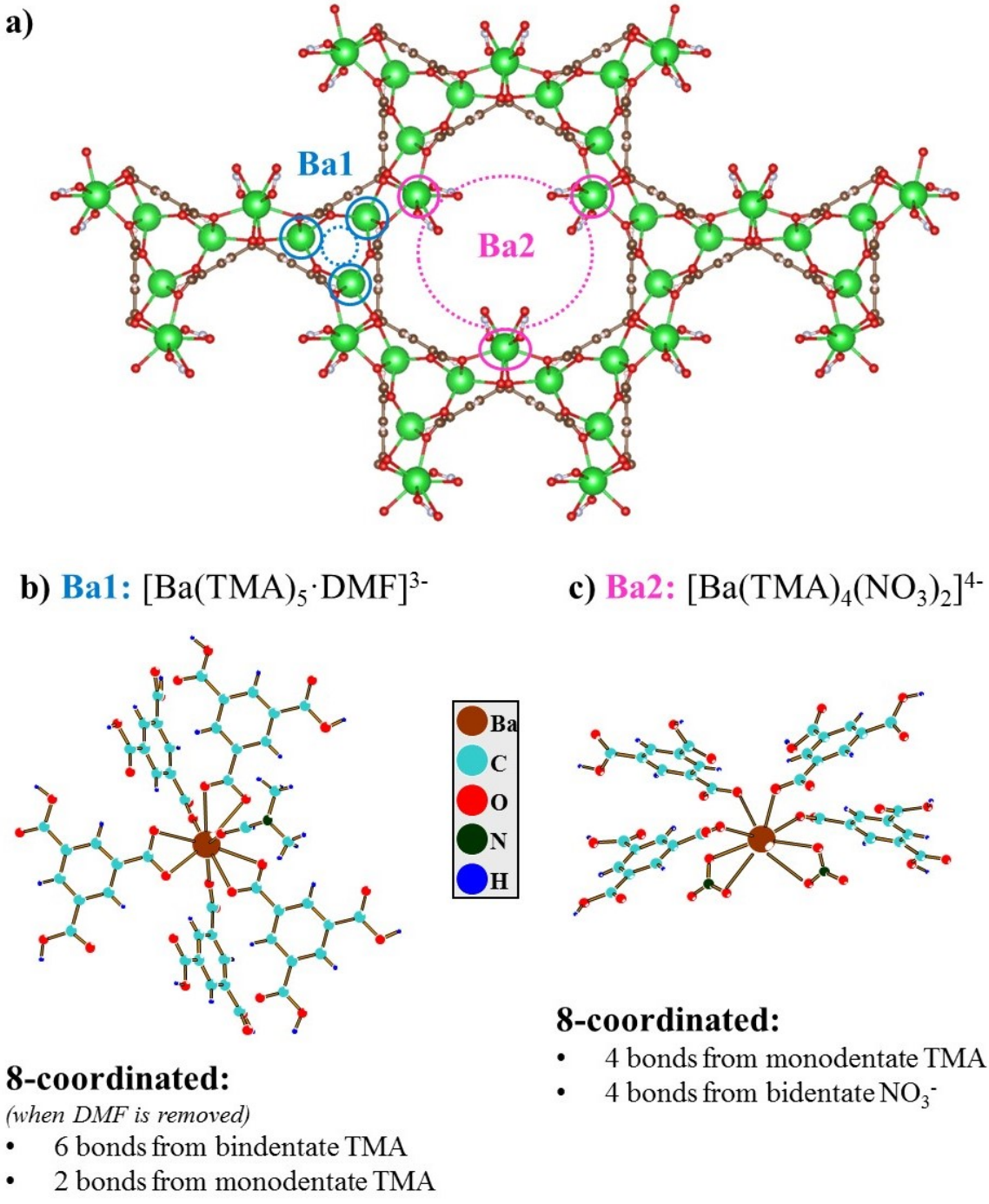

Figure 4-17. *$Ba_2TMA(NO_3)$ 3D 2x2x3 supercell (a) showing the large one-dimensional channel formed by the structure. Ba1 and Ba2 metal SBUs are indicated within the 3D structure. The different metal SBUs Ba1 and Ba2 are shown and described in b) and c), respectively.*

This MOF was studied by the Huang group by $^{135/137}$Ba SSNMR and ^{13}C SSNMR. The adsorption of CO_2 had a tremendous impact on the $^{135/137}$Ba SSNMR spectrum, which resulted in no visible signal after adsorption. Although the effect of the guest on the metal center seems important, due to the signal disappearing it was not possible to identify which of the two Ba centers were responsible for selective adsorption of CO_2. The ^{13}C SSNMR results obtained by the Huang group however were able to show that the guest is quite strongly bound to the framework, and that there are two binding sites (see Figure 4-18 below).

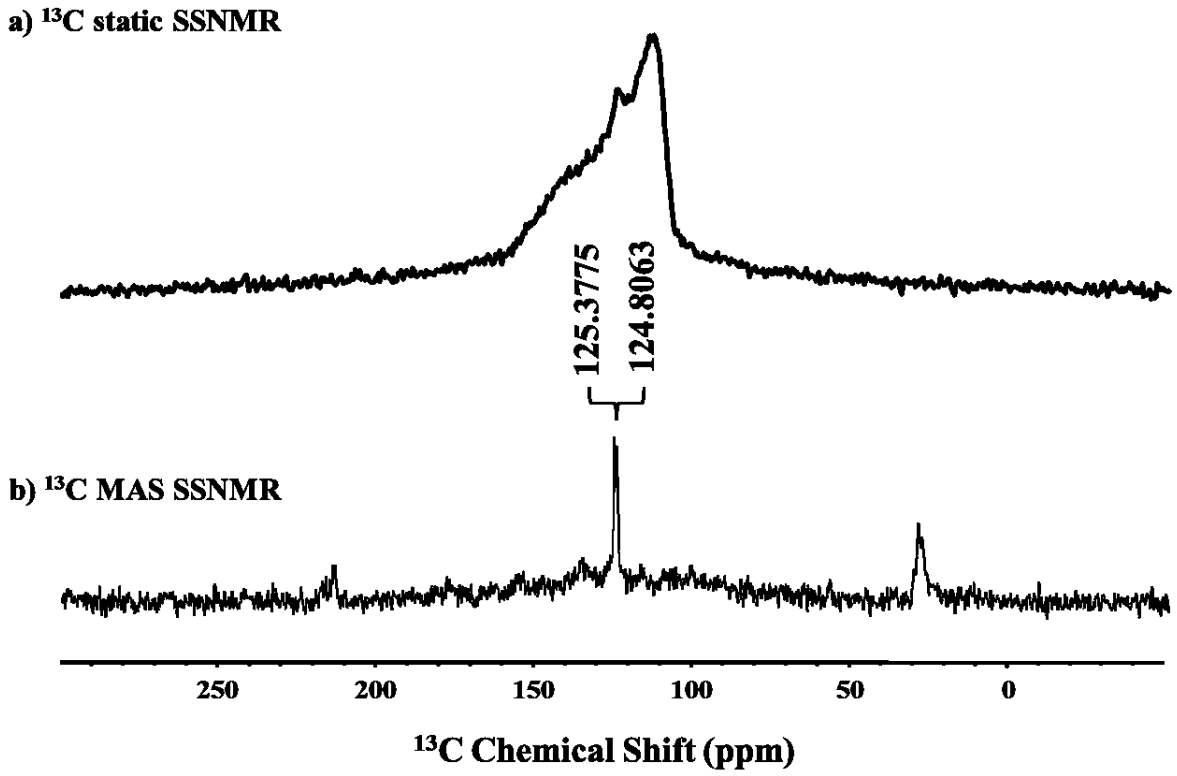

Figure 4-18. *Static (a) and MAS (b) ^{13}C SSNMR data for CO_2 loaded in $Ba_2TMA(NO_3)$ (1:0.1 Ba:CO_2). The strong, high peaks indicate relatively strong binding strength. The two peaks corresponding to two different binding sites are indicated in the MAS spectrum. Note: ^{13}C signal is not shown for organic SBU contributions. ^{13}C-enriched CO_2 gas was loaded into the activated framework to increase the CO_2 signal. Data acquired and provided by Professor Yining Huang (Western University).*

Our computational investigation of $Ba_2TMA(NO_3)$ aims to elucidate similar characteristics compared to the MIL-68(In) work which was already documented in this thesis, which includes the following:

- The number and localization of CO_2 binding sites within $Ba_2TMA(NO_3)$;
- The number and localization of DMF binding sites within $Ba_2TMA(NO_3)$;
- A comparison of CO_2 and DMF binding sites obtained through our study;
- The Ba SBU which is responsible for selective adsorption of guest (or whether one of the two sites is responsible for selective adsorption);
- A qualitative picture of the dynamic behaviour of CO_2 binding sites within $Ba_2TMA(NO_3)$.

4.4.2 CO_2 Results

4.4.2.1 Binding site analysis

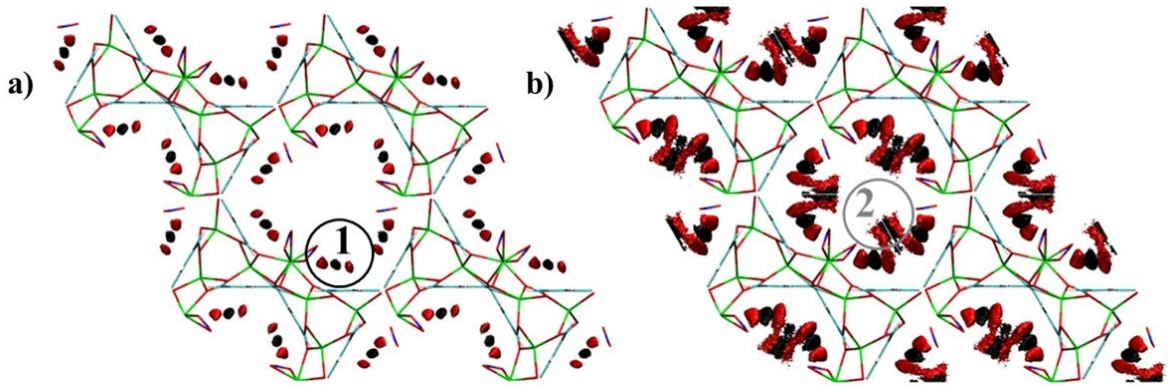

Figure 4-19. *Isosurface plots of the probability density showing a single CO_2 binding site (**BB1-CO_2**) in activated $Ba_2TMA(NO_3)$ at higher probability isovalue (0.05) (a) and a second CO_2 binding site (**BB2-CO_2**) at slightly lower isovalue (0.013) (b). T = 298 K, P = 1.0 bar. Black: CO_2 - C, Red: O, Blue: N, Green: Ba, Light blue: MOF C, White: H.*

Figure 4-19 shows an overview of GCMC simulation results. A very well-localized, single CO_2 binding site can be seen near both Ba1 and Ba2 centers (will be referred to as **BB1-CO_2**, where the first **B** stands for "Ba"). At higher pressures, another slightly less well

localized binding site forms directly "above" two of the binding sites as evidenced by decreasing the isovalue of the probability density plot (will be referred to as **BB2-CO_2**) (see Figure 4-19, right).

The oxygen on the localized binding site (**BB1-CO_2**) is directly between Ba1 (Ba1-O distance: 3.14 Å) and Ba2 (Ba2-O distance: 3.60 Å). An interaction with another Ba1 atom, closer to the other CO_2 oxygen (Ba1-O distance: 3.63 Å) also plays a role in the stability of **BB1-CO_2**. (Note: throughout the text, the Ba1 which is closer to **BB1-CO_2** will be referred to as Ba1-a, and the Ba1 which is further from **1** will be referred to as Ba1-b). It is worth nothing here that because all Ba1 centers are crystallographically equivalent, all Ba1 binding environments must be identical. As a result of this, for a CO_2 binding site which interacts closely with Ba1-a (3.14 Å) and less closely with a Ba1-b site (3.63 Å), there will be another site which interacts closely with Ba1-b (3.14 Å), but from another channel. This is why three **BB1-CO_2** binding sites are present near the threefold symmetric Ba1 equilateral triangular motif (see Figure 4-20a)). Figure 4-20 provides a visualization of all interactions of the **BB1-CO_2** site with $Ba_2TMA(NO_3)$, and Table 4-4 summarizes all distances relevant to these interactions.

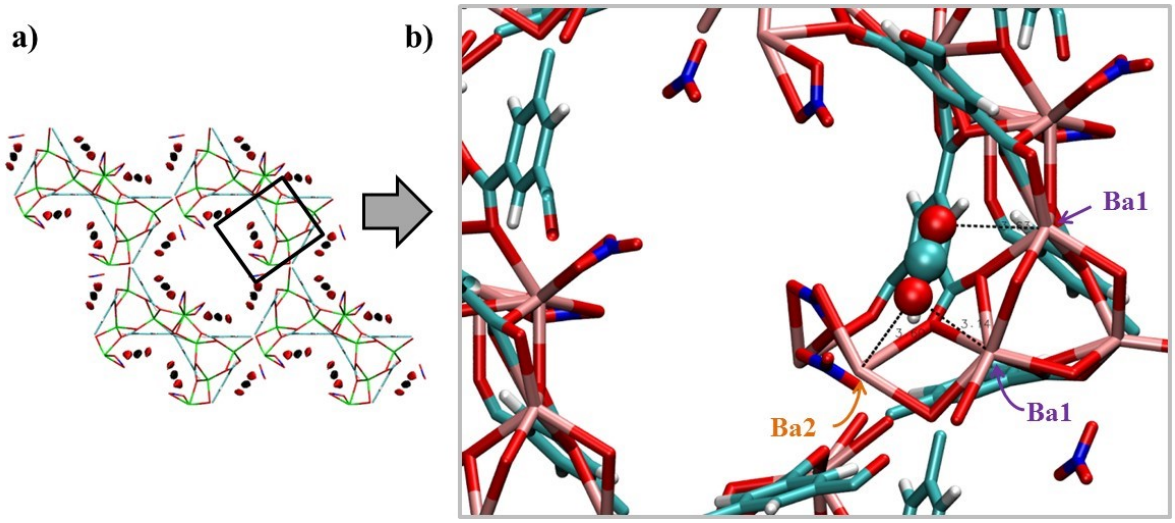

Figure 4-20. *Enhanced view of DFT-optimized CO_2 binding site **BB1-CO$_2$** (b) and GCMC-derived probability density distribution (a). The black square found in a) is representative of the area shown in the enhanced view b). Black: CO_2 - C, Red: O, Blue: N, Green: Ba (left), Pink: Ba (right) Light blue: C, White: H.*

As for **BB2-CO$_2$**, shown in Figure 4-21, it is formed through a cooperative interaction with **BB1-CO$_2$**, as shown by the orientation **BB2-CO$_2$** adopts with respect to **BB1-CO$_2$**. A "T-shape" is formed by the two binding sites because **BB2-CO$_2$** interacts favourably with **BB1-CO$_2$**'s carbon center through its oxygen (**BB2-CO$_2$**(O) – **BB1-CO$_2$**(C) distance: 2.96 Å). These types of cooperative interactions have been seen to provide enhanced binding strength within other MOFs when both T-shape binding sites are occupied.[15] The T-shape is distorted however by the nearby NO_3^- oxygen, which interacts with **BB2-CO$_2$**'s central carbon atom (**BB2-CO$_2$**(C) – NO_3(O) distance: 3.32 Å). A summary of these distances is provided in Table 4-4.

As a technical side-note, we found that it is very important to account for dispersion interactions, as they significantly impacted interactions of the framework with CO_2. Dispersion interactions are accounted for using the Grimme method (DFT+D2).[16] Only parameters for certain elements from the first five rows of the periodic table were included in the original D2 method paper, and parameters for other elements (including Ba) have since

been derived and were provided elsewhere.[17] When dispersive interactions are not accounted for, the interaction of **BB1-CO_2** with Ba1-b contributes less to the binding site's orientation. This is shown in Figure 4-22, and relevant distances are shown in Table 4-4 (see the column entitled "DFT (no dispersion)").

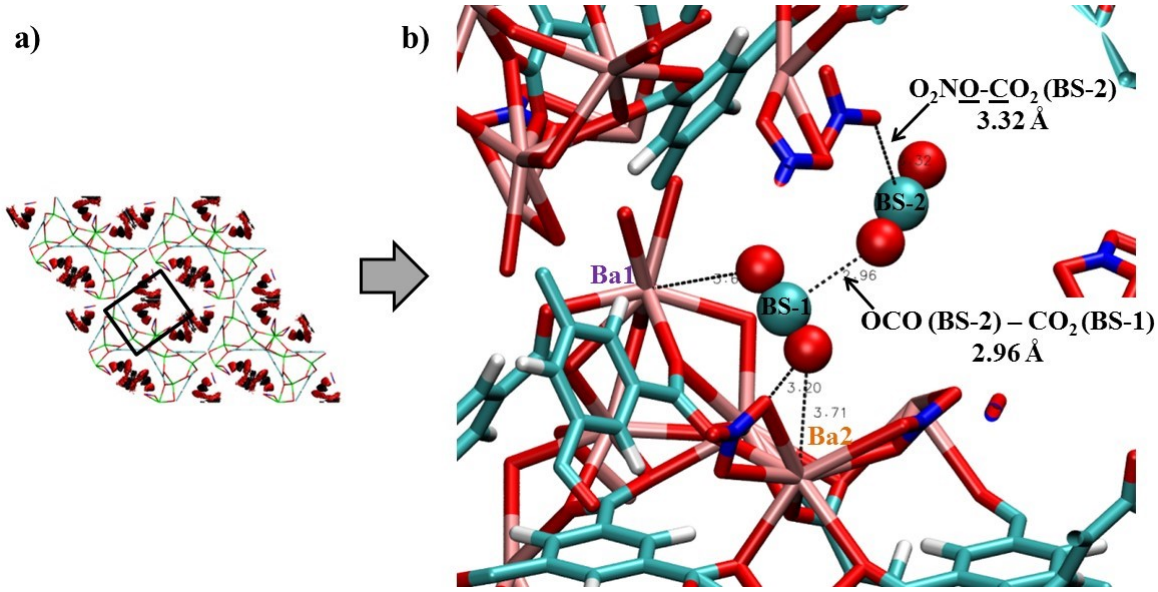

Figure 4-21. *Enhanced view of GCMC-derived CO_2 binding sites **BB1-CO_2** and **BB2-CO_2** (b) and GCMC-derived probability density distribution with smaller isovalue (0.013) (a). The black square found in a) is representative of the area shown in the enhanced view b). Black: CO_2 - C, Red: O, Blue: N, Green: Ba (left), Pink: Ba (right) Light blue: C, White: H.*

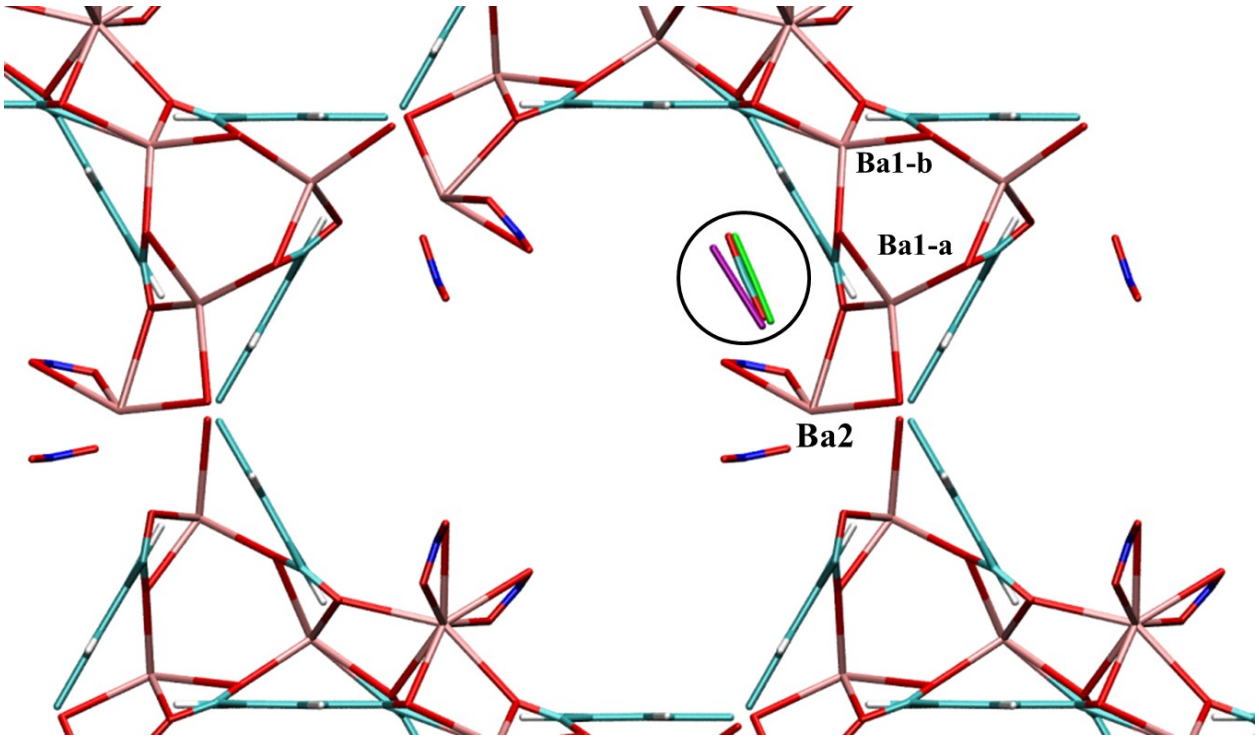

Figure 4-22. *DFT-optimized* ***BB1-CO$_2$*** *positions without dispersion interaction (purple), with dispersion interactions (green) and extracted from GCMC probability distribution (CO_2 located between the two DFT-optimized CO_2). T = 298 K, P = 1.0 bar. Red: O, Pink: In, Light blue: C, White: H. Framework atoms marked are discussed in the text.*

Table 4-4. *Binding energy and distances to framework atoms for CO_2 binding site* ***BB1-CO$_2$*** *and* ***BB2-CO$_2$*** *found in $Ba_2TMA(NO_3)$.*

BB1-CO_2	**GCMC**	**DFT (no dispersion)**	**DFT (dispersion)**
Shortest Distance of CO_2 atom to Ba1 (Å)	3.25	3.37	3.14
Second Shortest Distance of CO_2 atom to Ba1 (Å)	3.75	4.25	3.63
Shortest Distance of CO_2 atom to Ba2 (Å)	3.71	3.58	3.60
Total Binding Energy (kJ/mol)	50.7	-	75.1
Electrostatic Component of Binding Energy (%)*	45	-	-
Noncovalent Component of Binding Energy (%)*	55	-	-
BB2-CO_2		**GCMC**	
Total Binding Energy (kJ/mol)		23.4	
Electrostatic Component of Binding Energy (%)*		44	
Noncovalent Component of Binding Energy (%)*		56	

Table 4-4 shows all relevant **BB1-CO_2** distances and energies, as well as GCMC-derived **BB2-CO_2** binding energy (for force field-derived **BB2-CO_2** distances, see Figure 4-21). Our work confirms that **BB1-CO_2** is a strong binding site, and we also find the binding energy to have a particularly strong electrostatic component. To provide some basis for comparison, the binding energy for CO_2 in a MOF with open metal Mg^{2+} sites, Mg-MOF-74, has been calculated to be 41.4 kJ/mol using the PBE-D2 method we also used.[18] The significantly higher DFT binding energy compared to the GCMC force field-derived binding energy was an indication that there may be some charge transfer interactions at play between **BB1-CO_2** and Ba1/Ba2, which is why an investigation was carried out to explore these effects further in section 4.4.4.

4.4.2.2 Molecular Dynamics

MD simulations were carried out to determine the time evolution of the CO_2 in the two binding sites. This study is analogous to that performed for CO_2 adsorbed in MIL-68(In) (section 4.3.2.4). For this MOF, it is particularly interesting to analyze the frequency (or possibility) of switching of binding sites between both binding sites observed.

The conditions used for this MD study are similar to those used for the MIL-68(In) MD study. A 40 ns MD trajectory is produced at 298K constant temperature and 1bar of constant pressure. (The reader is referred to section 4.2.3 for further details on the MD simulation parameters used). The loading of CO_2 used for the MD simulation was the loading as determined from an equilibrated GCMC simulation at 298K, 1 bar for the same system (122 molecules for a 2x2x3 unit cell MD supercell simulation size, which corresponds to ~10 CO_2 molecules/unit cell, or 3.10 mmol CO_2/g $Ba_2TMA(NO_3)$. It is of relevance to note here that a 2x2x3 supercell was used to satisfy the minimum image

convention, which insures that particles do not interact with their own periodic image. The $Ba_2TMA(NO_3)$ unit cell lengths are a, b, c = [17.8254, 17.8254, 10.2582]. For all our simulations, the cutoff used is 12.5 Å, meaning that the chosen supercell must have minimal dimensions of 25Å in all directions.)

Comparing the dynamics of $Ba_2TMA(NO_3)$ to those of MIL-68(In), it is expected for there to be more of a distinction between the two binding sites observed in this system compared to the distinctions in residence time observed for MIL-68(In)'s **B1-CO_2** and **B2-CO_2** for example, because the binding strengths of the two binding sites **BB1-CO_2** (GCMC: 50.7 kJ/mol, see Table 4-4) and **BB2-CO_2** (GCMC: 23.4 kJ/mol, see Table 4-4) found in $Ba_2TMA(NO_3)$ is not close in magnitude. 5 distinct CO_2 molecules were tracked to determine their dynamics for 2.5 ns. It was found that, for all 5 trajectories, the longest residence time observed for the first, strong binding site (**BB1-CO_2**) was ~713 ps and the shortest residence time observed was ~ 10 ps. Figure 4-23b) provides a depiction of snapshots taken of **BB1-CO_2** over the longest residence time, and the most frequent orientation of CO_2 observed demonstrates the favourable interaction with Ba1 and Ba2. Throughout the 2.5 ns trajectories, The strongest binding site was visited on average 9 times, and on average remained there for ~ 200 ps. In stark contrast, the second, weaker binding site (**BB2-CO_2**) retains a CO_2 molecule for a maximum of ~ 137.5 ps, but a comparable minimum residence time of ~ 3 ps. The average (and mode) residence time was determined to be ~ 50 ps. The weakest binding site is visited approximately twice as many times (19 visits on average for 2.5 ns) as the stronger binding site, though as residence times demonstrate, it is visited for significantly shorter times on average. This is consistent with **BB1-CO_2** being quite strong and **BB2-CO_2** being relatively weak in comparison.

Figure 4-23a) depicts the trajectory of a single CO_2 molecules during 3 ns of simulation, over which period the molecule is capable of traveling throughout the entire channel and accessing every binding site. As shown in Figure 4-23c), a CO_2 molecule can readily travel from **BB2-CO_2** to a different **BB1-CO_2** site within the channel, but it seems that most often the formation of **BB1-CO_2** throughout the trajectory is preceded by the presence of the same CO_2 molecule in an immediate, neighbouring **BB2-CO_2** site.

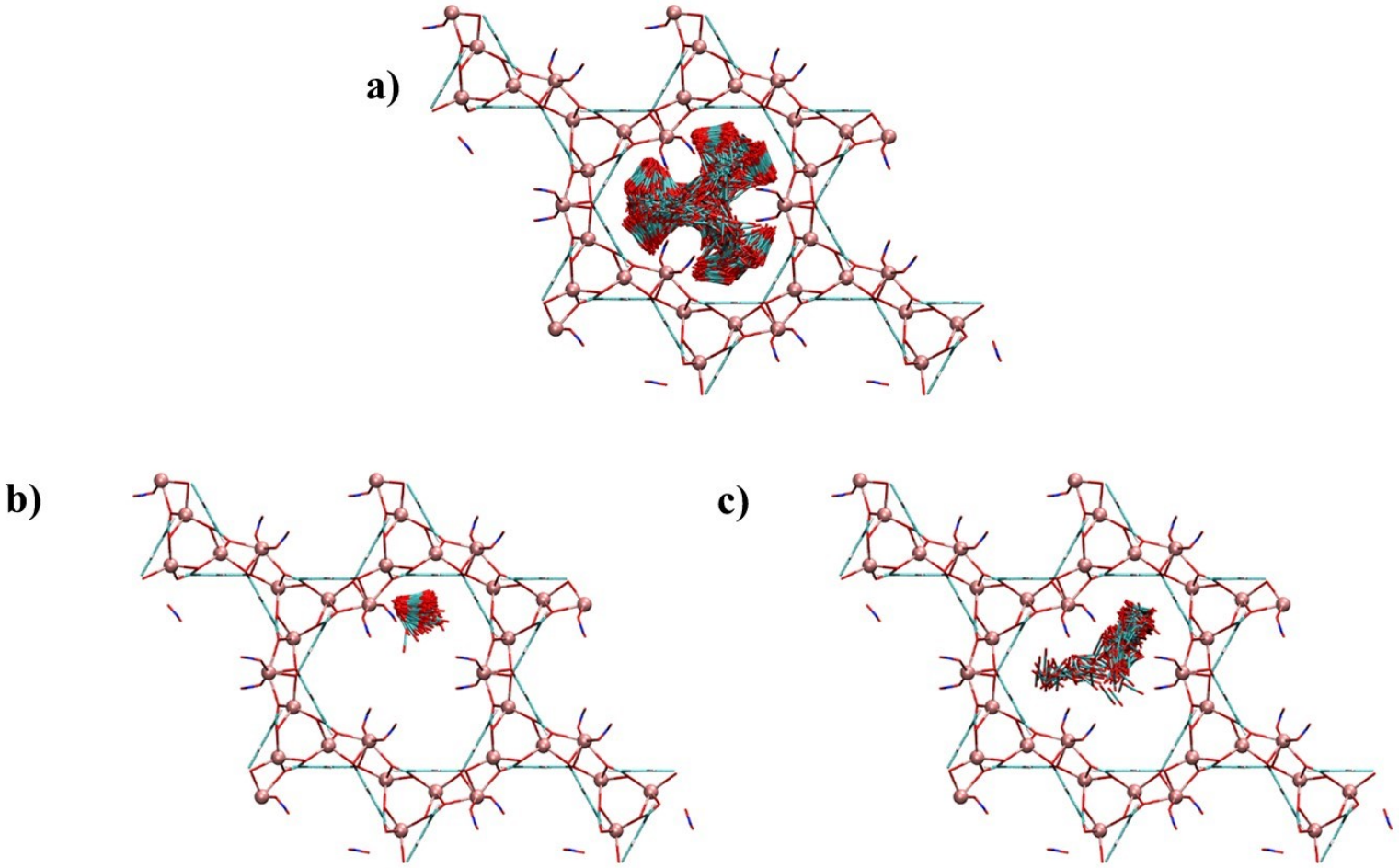

Figure 4-23. *All images shown feature a $Ba_2TMA(NO_3)$ supercell visualized along the c axis. In a) snapshots taken every 0.5 ps are shown for a single CO_2 molecule over the course of 3 ns of simulation. In b), the longest residence time for* ***BB1-CO$_2$*** *(713 ps) is shown (images from trajectory shown every 0.5 ps). Finally, in c) a single CO_2 is shown hopping from BB2-CO_2 to another BB2-CO_2 site (images from trajectory shown every 0.5 ps).*

This study demonstrates preliminary findings regarding the dynamics of CO_2 in $Ba_2TMA(NO_3)$. Especially since the effect of dynamics are captured by ^{13}C SSNMR spectra, we wish to carry out more rigorous quantitative studies on the dynamics of guests in the framework. This includes study of the mean angle of CO_2 with respect to the binding sites, mean and average residence times, switching rates and possibly even studies of the diffusion of CO_2 within the channel. More details on future work to be carried out on this system are given in Chapter 5.

4.4.3 DMF Binding Analysis

Figure 4-24 shows the GCMC probability density plot for DMF which identifies a single binding site, **BB1-DMF**. As shown more clearly in the enhanced view in Figure 4-24 (b), our GCMC results show that DMF can occupy two pairs of symmetrically equivalent binding sites. For a single Ba1 site, there are two possible orientations of the DMF binding site, which bind through the same oxygen atom but show a "flipped" positioning of the hydrogen atoms and CH_3 groups. Due to overlapping atoms, it is impossible for both of these equivalent binding sites to be occupied at once. Apart from the "flipped" pair, in close proximity is another pair of these "flipped" binding sites, in which the oxygen binds through another Ba1 center. In order to better understand this distinction, it is helpful to recall how **BB1-CO_2** was found to bind to both Ba1-a and Ba1-b, two Ba1 centers which face the inside of the pore. In contrast to the "flipped" pair, it appears that **BB1-DMF** bound to Ba1-a could be occupied at the same time as a **BB1-DMF** site bound to a Ba1-b center.

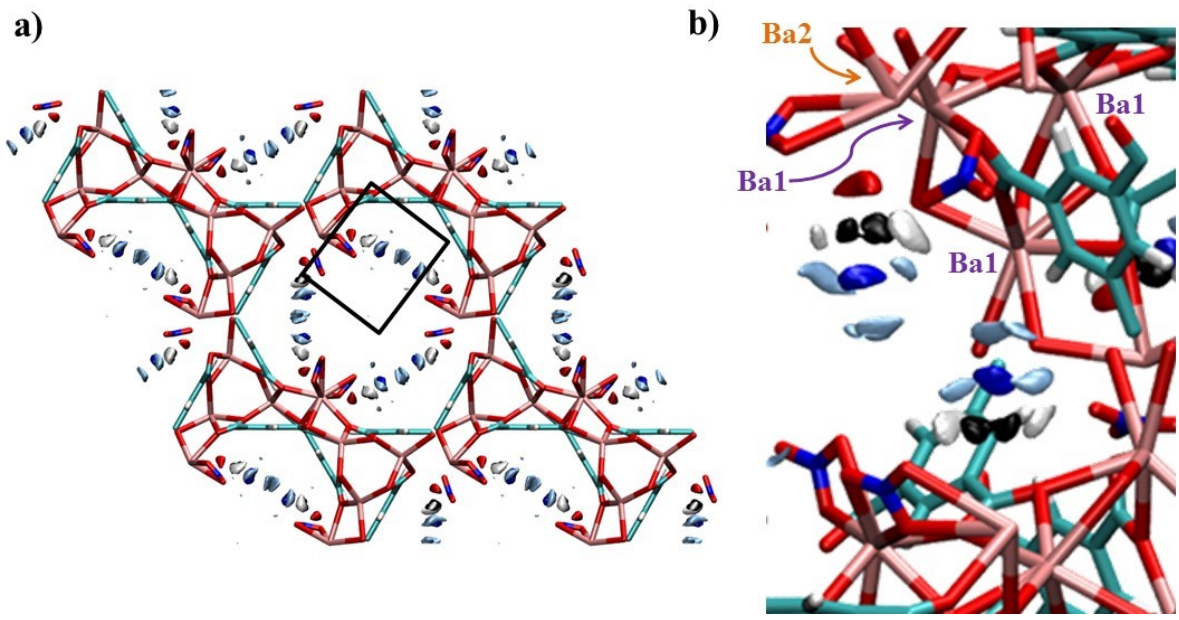

Figure 4-24. *Isosurface plot of the probability density showing the single DMF binding site (**BB1-DMF**) in activated $Ba_2TMA(NO_3)$ in a supercell (a) and an enhanced view of one of these binding sites (b). Isovalue = 0.09, T = 298 K, P = 1.0 bar.) Red: O, Blue: N, Pink: Ba, turquoise: C of framework, White: H, Blue-grey: $\underline{C}H_3$ carbon of DMF, Black: C=O carbon of DMF.*

Our GCMC simulation makes use of a rigid guest model for uptake. For CO_2, this kind of approximation is generally acceptable because CO_2 tends to remain linear when adsorbed in MOFs (although this will likely not be true in cases where strong charge transfer interactions are the dominant interaction, but this can always be verified through DFT calculations), however for a more flexible guest like DMF, the approximation can break down. This is why the rigid guest GCMC simulations are more suited to first finding approximate binding sites. In this case, the short distances suggest that the interaction between the DMF-O and the Ba1 and Ba2 centers is important, but it is possible that the rest of the DMF molecule may relax to a different configuration once optimized. To investigate the possibility, we performed DFT calculations to optimize the approximate DMF binding sites found from the GCMC simulations. As it turns out, the preferred orientation for DMF is not dissimilar from the GCMC-derived position, meaning the rigid DMF model was a good approximation for behaviour of the binding site. What is curious however, as shown in

Figure 4-25, is the difference in orientation the DMF in the original $Ba_2TMA(NO_3)$ CIF file has compared to our optimized binding site. (Note: the original CIF file provided is for pre-activated $Ba_2TMA(NO_3)(DMF)$. It is reasonable to use this structure for our calculations as PXRD experiments for the pre-activated and activated MOF are very similar, meaning that the structure does not change significantly upon activation. See Figure 4-16 in section 4.4.1 for PXRD spectra). The O=C-N group has the same orientation and localization for both the GCMC and CIF-derived binding sites. The difference between the GCMC-derived and experimentally-derived DMF configurations lies in the orientation of the two CH_3 groups found on N. For our GCMC-derived molecule, the CH_3 groups are in the most favourable orientation for free DMF. However, for the CIF-derived binding site, the CH_3 groups are oriented in such a way that they are closer to the pore walls. In this CIF orientation, the CH_3 groups are oriented perpendicularly to the rest of the molecule, whereas in the GCMC-derived binding site, the DMF backbone is within a single plane. The calculated binding energy for the CIF-derived DMF configuration (DFT-CIF (VASP), see Table 4-5) is significantly lower than that of our GCMC-derived configuration (DFT (VASP), also in Table 4-5).

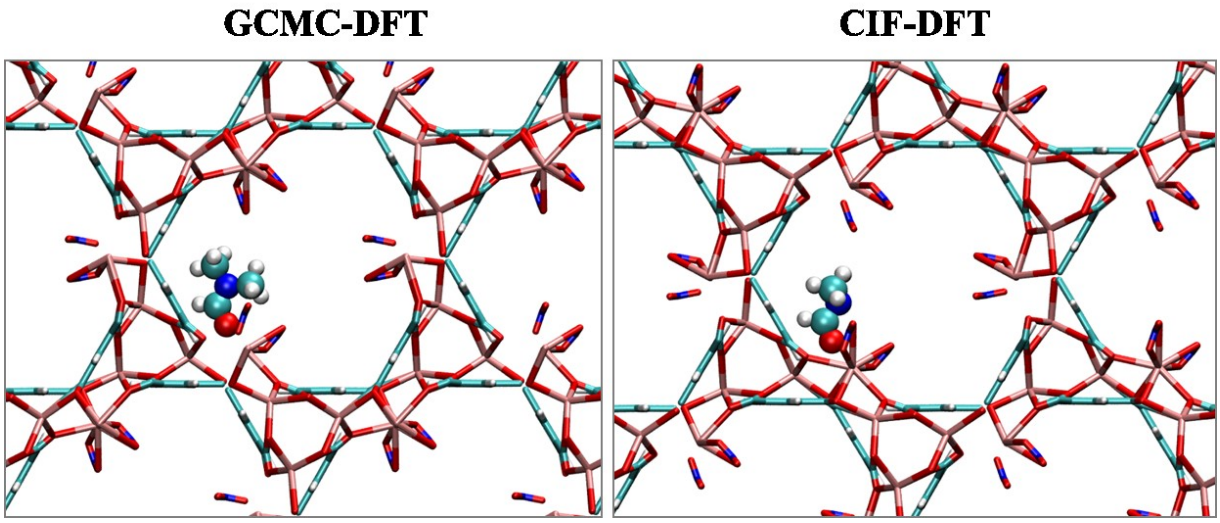

Figure 4-25. *DFT-optimized DMF binding site in activated $Ba_2TMA(NO_3)$ supercell with GCMC-derived and CIF-derived initial configurations. Red: O, Blue: N, Pink: Ba, turquoise: C, White: H.*

Table 4-5. *Binding energy and distances to framework atoms for DMF binding site found in MIL-68(In) (**BB1-DMF**). * The DMF positions and energy for DFT-CIF are those taken from DFT-optimized CIF-DMF positions provided within the H-optimized Ba MOF.*

BB1-DMF	GCMC	DFT (VASP)	DFT-CIF* (VASP)	Experimental
Shortest Distance of DMF –O atom to Ba1 (Å)	3.19	3.01	2.98	2.955
Shortest Distance of DMF –O atom to Ba2 (Å)	3.26	3.16	3.32	3.189
Total Binding Energy (kJ/mol)	124.9	195.3	65.8	-

** The DMF positions and energy for DFT-CIF refer to the DFT-optimized CIF-derived DMF positions. Optimization was necessary because no H atoms were included in the DMF included in the framework or on the framework organic SBUs in the original CIF file. The optimized DMF CIF-derived positions are quite similar to that found pre-optimization.*

Finally, relevant DMF binding distances are shown in Table 4-5. The calculated distances from Ba1 and Ba2 to the DMF-oxygen match well with experiment. The binding energy of DMF is quite high, which reflects the strong interaction of DMF with the metal centers. As well, as was observed for **BB1-CO_2** in section 4.5.2.1, the DFT binding energy for **BB1-DMF** is much higher than the force field-derived binding energy, which indicates the possibility of charge transfer interactions between **BB1-DMF** and Ba1/Ba2. The investigation of these effects is carried out in the next section.

4.4.4 Charge transfer interactions between metal SBUs and guest

As both strong CO_2 and DMF binding sites position the guest molecules in close proximity to both Ba1 and Ba2, it is necessary to explore the possibility of covalent bonding or charge transfer interactions involving the metal centers. The GCMC simulations we performed do not capture these effects, so we utilized Bader charge analysis and charge density difference analysis of the DFT-derived total electron densities.[19] In the case of CO_2 the DFT-optimized distances between Ba1-**BB1-CO_2** and Ba2-**BB1-CO_2** show that **BB1-CO_2** is distinctly closer to Ba1 than Ba2, while in the case of DMF, **BB1-DMF** is approximately the same distance from the two types of Ba centers. Thus it is interesting to compare and contrast the findings from these two types of charge analyses for both CO_2 and DMF in $Ba_2TMA(NO_3)$.

The Bader charges of atoms in a molecule (or periodic material) result from a partitioning of the total electron density. They are the product of Richard Bader's intuitive Atoms in Molecules (AIM) partitioning scheme.[19] In this approach, molecules are divided into atomic regions based on the topology of total electron density. Since there are always maxima of the charge density at the nuclei (or very close to them), the density will reach a minimum between any two atoms to form a 'valley'. Walking along the bottom of these 'valleys' defines a natural surface from which molecules can be divided into atomic regions. The charge enclosed within these regions (or volumes) defines the Bader charge of an atom within a molecule. In this work, we use Bader charge analysis as implemented into the VASP periodic DFT package by Henkelman *et al.*[20–22] The quantitative results of Bader charge analyses for **BB1-CO_2** and **BB1-DMF** in $Ba_2TMA(NO_3)$ are given in Tables 4-6 and 4-7, respectively. Diagrams showing the spatial arrangement of atoms listed in Tables 4-6

and 4-7 are available in Figures 4-26 and 4-27, respectively. Bader charges were calculated for both the empty framework and the framework with guest adsorbed. The empty framework and isolated guest molecule charges were then subtracted from the Bader charges on the framework with the guest adsorbed. When the charge difference is zero for a given framework atom, this indicates that inclusion of guest species does not affect the charge on the framework atom. Our results show that for distant framework atoms (> 20 Å), the difference in Bader charges are essentially zero as one would expect. Therefore, the only charge differences included in Tables 4-6 and 4-7 are those which were non-zero. These are framework atoms relatively close to the binding site. It is worth noting that the Bader charge differences obtained were quite small, so it was necessary to use a Fast Fourier Transform (FFT) mesh twice as fine as normal to obtain quantitative differences.

Overall, we expected and did see non-zero charge density differences on the Ba atoms. It is important to note however that the charge differences we found were exceedingly small, on the order of 10^{-3} electrons. These small differences indicate that very little charge transfer is taking place (if at all). In spite of the small differences, it is still interesting to analyze the Bader charge differences, as they indicate the locations where these small amounts of charge are transferred. One noteworthy result is that linker atoms which are further away from the binding site show, in some cases, larger charge differences than those observed on the Ba atoms to which the guest binds directly. The next paragraphs relay this finding using the quantitative data acquired.

Although the **BB1-CO_2** oxygen is clearly closer to the Ba1 than Ba2 (3.14 Å vs. 3.60 Å), the low-magnitude charge transfer interactions seem to mostly be taking place with Ba2 (-0.0033) according to values from Table 4-6. In support of this is the second strongest

charge transfer interaction (0.0019) which takes place on the NO_3-oxygen which connects to Ba2 closest to CO2. The third most important contribution (0.0012) is for the Ba1-oxygen nearest to CO2, followed by the Ba2-oxygen (-0.0010), which is of opposite sign.

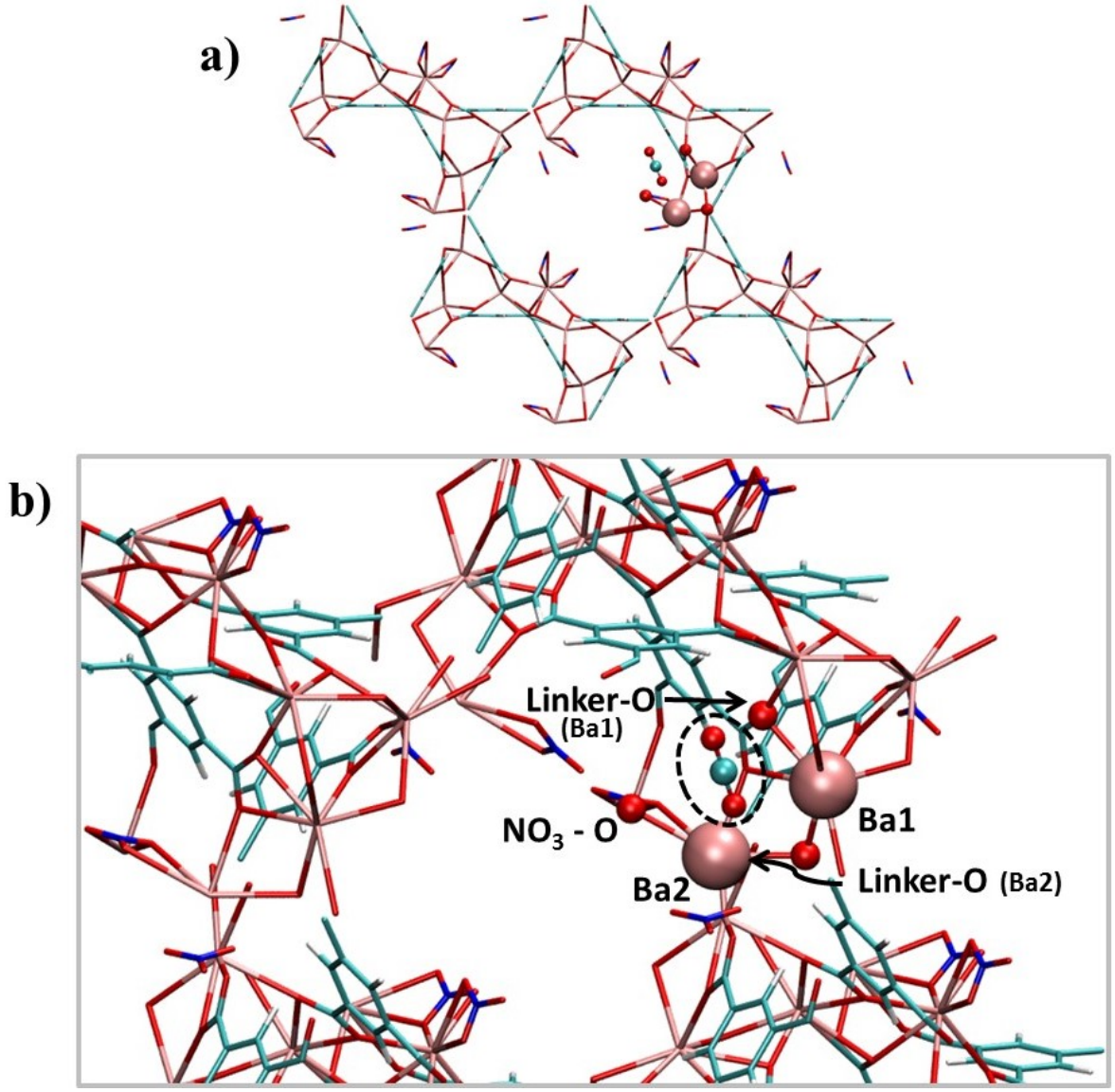

Figure 4-26. *DFT-optimized* ***BB1-CO₂*** *in $Ba_2TMA(NO_3)$ (shown along c axis) (a) and close-up view of the same* ***BB1-CO₂*** *site (b). Atoms which have been named in b) are those upon which Bader charge analysis revealed non-zero results. Corresponding numerical results are available in Table 4-6. Red: O, Blue: N, Pink: Ba, turquoise: C, White: H*

Table 4-6. *DFT-derived Bader charge analysis for* ***BB1-CO_2*** *in $Ba_2TMA(NO_3)$. Charges shown are for atoms are as indicated in Figure 4-26.*

Atom name	Bader $q_{MOF+guest}$ – Bader q_{MOF}
Ba1	-0.0004
Ba2	-0.0033
NO_3 – O	0.0019
O - Linker (near Ba1)	0.0012
O – Linker (near Ba2)	-0.0010

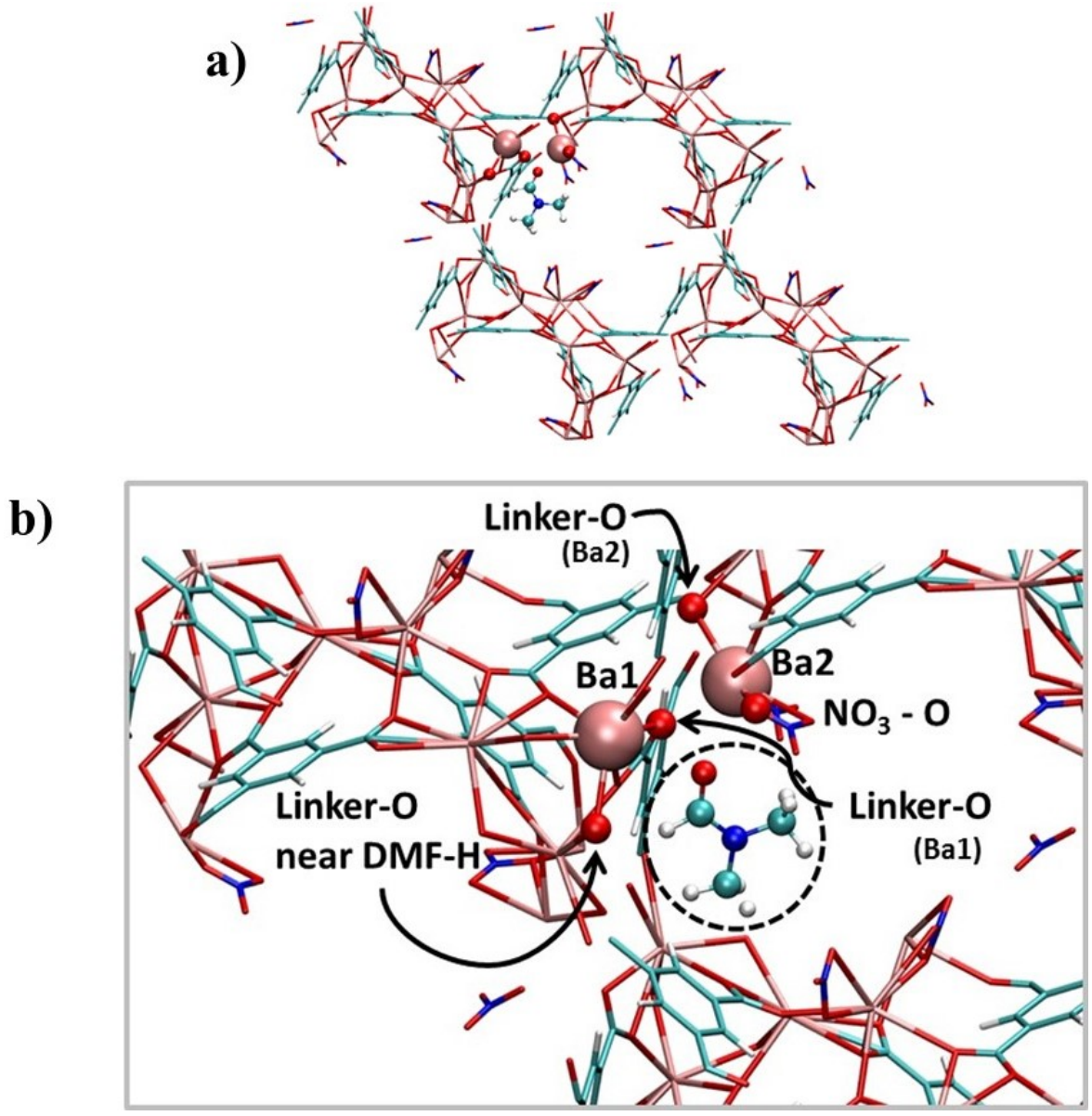

Figure 4-27. *DFT-optimized* ***BB1-DMF*** *in $Ba_2TMA(NO_3)$ (shown along c axis) (a) and close-up view of the same* ***BB1-DMF*** *site (b). Atoms which have been named in b) are those upon which Bader charge analysis revealed non-zero results. Corresponding numerical results are available in table 4-7.*

Table 4-7. *DFT-derived Bader charges for* ***BB1-DMF*** *in $Ba_2TMA(NO_3)$. Charges shown are for atoms are as indicated in Figure 4-27.*

Atom name	Bader $q_{MOF+guest}$ – Bader q_{MOF}
Ba1	-0.0024
Ba2	-0.0042
NO_3 – O	-0.0338
O – Linker (near Ba1)	-0.0172
O – Linker (near Ba2)	-0.0017
O – Linker (near Ba1 and DMF-H)	0.0082

For **BB1-DMF** (see Table 4-7), change in Bader charges upon guest adsorption are in some cases an order of magnitude larger than that observed for CO_2. In this case, the **BB1-DMF** oxygen is more equally spaced between Ba1 and Ba2 (3.01 Å and 3.16 Å respectively), so accordingly we expect to see an increased charge transfer from Ba1 compared to CO_2. Indeed, Ba1 (-0.0024) is involved in charge transfer, and Ba2 (-0.0042) is also involved, although slightly more than with CO_2.

The largest charge transfer interaction occurs on the NO3- oxygen (-0.0338) followed by the Ba1-O from the linker (-0.0172). This is interesting, as it demonstrates that transfer of charge from DMF to both Ba2 and Ba1 becomes distributed over the connected linker-carboxylate oxygen atoms or the NO_3^- oxygen atoms. The Ba2-O charge difference (-0.0017) is much lower, so it seems charge is preferentially distributed towards NO_3^-. This is agrees with the charge difference found on Ba2 (-0.0042), which is coordinated to the NO_3 group, and appears to be more heavily influenced by the guest than Ba1 (-0.0024). However, Ba2 is very slightly further away (3.16 Å) than Ba1 (3.01 Å), so it appears from our analysis that distance does not dictate which metal center is most heavily involved in transfer of charge. In any case, even the largest charge density difference arising from Bader analysis of DMF

adsorbed in $Ba_2TMA(NO_3)$ is on the order of 10^{-2} electrons, which is very small. Although there appears not to be significant charge transfer at play in any of the guest-host systems, our results do suggest slightly more charge transfer for **BB1-DMF** than **BB1-CO_2** adsorbed in $Ba_2TMA(NO_3)$.

In addition to the difference in Bader charges, the difference in charge density within the MOF can also be studied to give some idea of how charge is distributed throughout the MOF instead of on specific atoms. In this way, an analysis of Bader charge difference and charge density difference is complementary.

Unlike the Bader charge analysis which ascribes the total charge density to atomic regions, the charge density difference analysis simply involves determining the difference in total charge density at each point in space using the following relationship:

$$\Delta\rho = \rho_{MOF+guest} - \rho_{MOF} - \rho_{guest}$$

Where all of the "ρ"s represent electron densities which are functions of real space, i.e. $\rho(\vec{r})$. $\rho_{MOF+guest}$ is the charge density of the MOF including adsorbed guest species, ρ_{MOF} is the charge density for the empty MOF and ρ_{guest} is the charge density of the isolated guest species positioned as it would be in the MOF-guest complex.

The colour maps of the charge density difference, $\Delta\rho$, are shown for both **BB1-CO_2** (Figure 4-28a)) and **BB1-DMF** (Figure 4-28b)). Recall that three Ba centers are involved in the binding of **BB1-CO_2** in $Ba_2TMA(NO_3)$ as previously discussed. The labelling of Ba atoms mentioned here is shown in Figure 4-28 as well as previously in Figure 4-26. Ba1-a and Ba2 are involved in binding one of the oxygen atoms of CO_2 in site **BB1-CO_2**, while the other oxygen atom interacts with Ba1-b. The results shown for **BB1-CO_2** adsorbed in $Ba_2TMA(NO_3)$ in Figure 4-28a) suggest stronger interaction with Ba1-a than Ba2 due to

more intense coloring of the charge density plot, which is the reverse of the trend observed for the same system with Bader charge analysis, where the charge was observed to change slightly more on Ba2 than Ba1-a. The stronger charge transfer with Ba1 is consistent with the shorter DFT-derived Ba1-**BB1-CO_2** distance (3.14 Å, compared to 3.60 Å for Ba2- **BB1-CO_2**). Nonetheless, the results do show that CO_2 is interacting with both metal centers. The change in charge density near the other end of **BB1-CO_2**, near Ba1-b, also demonstrates interaction with this third Ba center. This was not observed using Bader charge analysis, likely due to the interaction being quite weak compared to other interactions, which according to the quantitative Bader results were also weakly interacting sites. We also know from DFT calculations that the presence of this center has some influence on **BB1-CO_2**, as depending on whether or not dispersion interactions were included, the distance of CO_2-oxygen to this metal center could change quite a bit (see Figure 4-22 and "Second Shortest Distance of CO_2 to Ba1" in Table 4-4).

Calculated charge density difference for **BB1-DMF** in $Ba_2TMA(NO_3)$ is displayed in Figure 4-28 (b). As with Bader charge analysis, the intensity of charge transfer appears to be overall higher for this guest than with **BB1-CO_2**. However, based on the colour map, it is not possible to say whether Ba1 or Ba2 interacts more strongly with the **BB1-DMF** oxygen atom, as was done for the **BB1-CO_2** oxygen atom. The charge density difference results, in addition to supporting Bader charge analysis results, therefore serve well to finalize our proposal about whether **BB1-DMF** binds preferentially to Ba1 or Ba2: we find that both Ba1 and Ba2 actively contribute to binding of DMF. Additionally, the colour map in Figure 4-28b) shows an increase in charge density away from **BB1-DMF** and into the framework

linkers. This displacement of charge into the organic SBUs was also shown to occur via Bader charge analysis.

Although the colour maps created for charge density difference in both **BB1-CO_2** and **BB1-DMF** give insight on where charge is transferred, the magnitude of $\Delta\rho$ values is on the order of 10^{-3} electrons $\cdot$ $Å^{-2}$. Based on both Bader analysis and charge density difference analysis, we conclude that the interactions between the guests and the Ba centers observed can be ascribed to polarization interactions rather than charge transfer. Additionally, we find a slight increase in the intensity of these polarization interactions for **BB1-DMF** compared to **BB1-CO_2**.

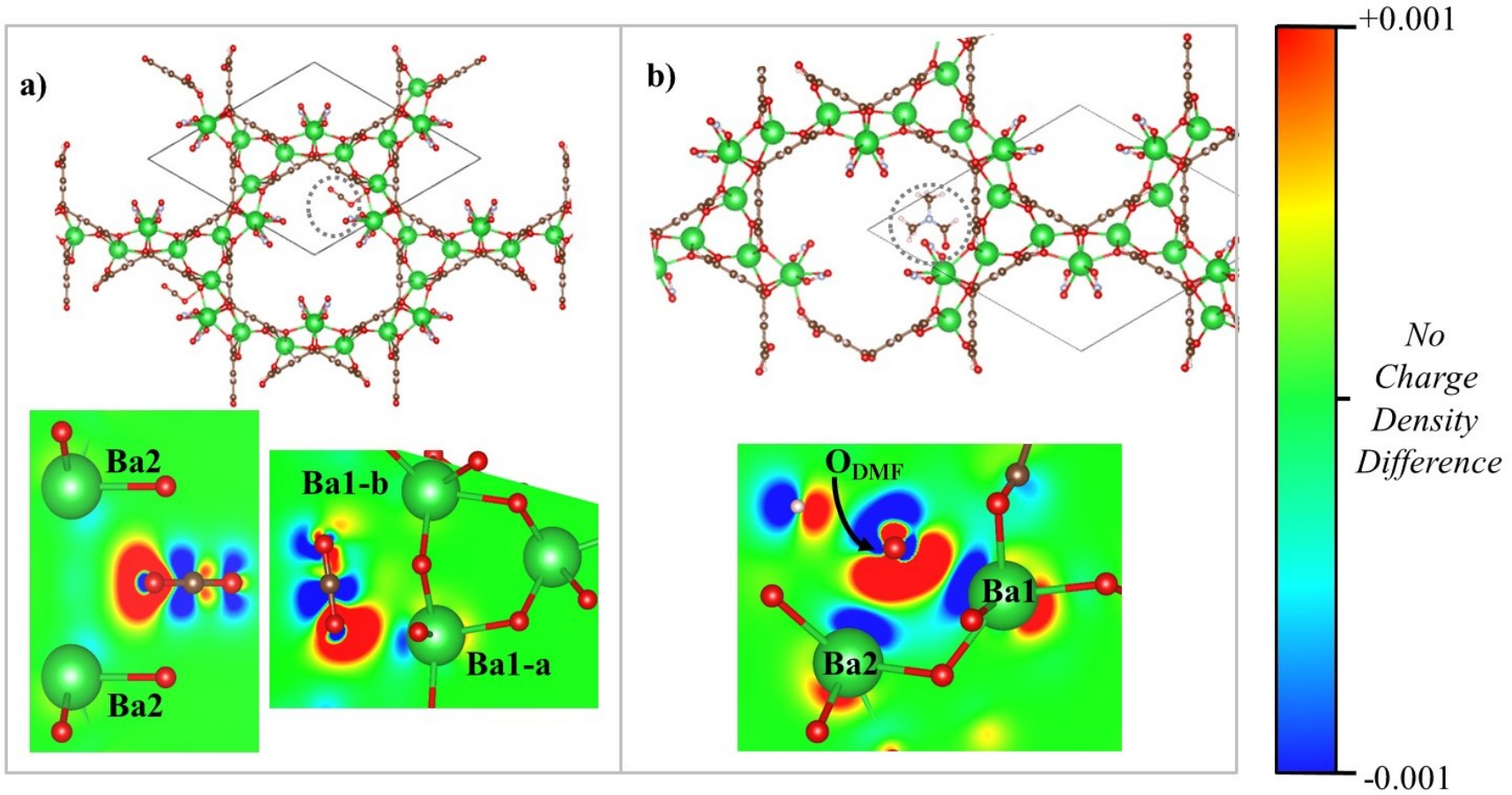

Figure 4-28. *Charge density difference for DFT-optimized* ***BB1-CO₂*** *(a) and* ***BB1-DMF*** *(b) binding sites in $Ba_2TMA(NO_3)$. For each figure, a circled binding site within the supercell is shown, and the charge density difference colour maps are shown below. For* ***BB1-CO₂****, a first colour map is shown which cuts through a (Ba2)-(Ba2)-(****BB1-CO₂****(O)) plane, and a second colour map is shown cutting through a (Ba1-a)-(Ba1-b)-(****BB1-CO₂****(O)) plane. For* ***BB1-DMF****, the colour map cuts through a (Ba2)-(Ba1)-(****BB1-DMF****(O)) plane. Calculated charge density differences vary between -0.001 and +0.001 electrons· $Å^{-2}$, as shown in the colour bar on the right. Brown: C, Green: Ba, Red: O, White: H, Light blue: N*

4.4.5 Conclusion

GCMC simulations and DFT calculations were carried out to investigate the interactions of guests with $Ba_2TMA(NO_3)$. In terms of DMF, a single binding site is identified (**BB1-DMF**), for which the DMF-oxygen interacts directly with both Ba1 (3.01 Å) and Ba2 (3.16 Å). This corresponds well with experimentally determined Ba1-O and Ba2-O distances (2.955 and 3.189 Å). We find that **BB1-DMF** does not bind to a single Ba site, but instead that both Ba1 and Ba2 contribute to binding **BB1-DMF** through DMF's oxygen atom. Charge density difference and Bader charge analysis are used to make these claims, and also show that polarization interactions are taking place.

One main CO_2 binding site (**BB1-CO_2**) is observed in $Ba_2TMA(NO_3)$. The area where CO_2 binds is roughly the same as where DMF binds with a few differences: first, the other CO_2 oxygen (ie. The oxygen which is not binding to Ba1 and Ba2 like with DMF) interacts with a different Ba1 center (referred to as Ba1-b). This interaction is evidenced by the two atoms' proximity, turning dispersion interactions on and off for DFT optimization calculations and charge density difference results. Second, the distances are skewed so that **BB1-CO_2** is closer to Ba1-a (3.14 Å) than Ba2 (3.60 Å). Whether or not this truly indicates that CO_2 interacts more strongly with Ba1 than Ba2 however seems debatable, as Bader charge analysis and charge density difference provide differing conclusions. In any case, both Bader charge analysis and charge density difference results show that there are polarization interactions between **BB1-CO_2** and Ba atoms, which are even weaker than those found for **BB1-DMF**. The results suggest that **BB1-CO_2** interacts with both metal centers (Ba1-a and Ba2) to some extent, as well as weakly with the second Ba1 site (Ba1-b). A second CO_2 binding site (**BB2-CO_2**) appears at higher isosurface probability, and would in

practice appear at higher pressures. **BB2-CO_2** cooperatively binds by interacting with the first binding site (in a T-shape with **BB1-CO_2**) as well as with an NO_3^- oxygen (through the **BB2-CO_2** carbon). This cooperative binding interaction has been observed in other MOFs. The identification of two CO_2 binding sites is in agreement with the ^{13}C SSNMR data acquired by the Huang group, which also identifies two binding sites.

Finally, MD simulations were also carried out to probe the dynamics of CO_2 in the MOF. The ordering of the average residence times for **BB1-CO_2** (~200 ps) and **BB2-CO_2** (~50 ps) is as expected given the relative strength of these two binding sites. The order in which the binding sites were visited was of interest: a single CO_2 molecule was often seen hopping from one **BB2-CO_2** to another site **BB2-CO_2** but never from a site **BB1-CO_2** to another site **BB1-CO_2**. This is certainly related to another observation: a site **BB1-CO_2** is consistently occupied directly after the immediate neighbouring site **BB2-CO_2** has been visited. In addition to providing unique insight on the interactions of CO_2 with $Ba_2TMA(NO_3)$, this type of information is very important for our experimental collaborator Professor Huang, as he has the possibility to reproduce SSNMR spectral curves based on these kinds of simple models (see Future Work, Chapter 5).

4.5 Summary of findings

Throughout this work, we have not only shown the value of molecular simulation for characterizing MOFs in many different ways (binding site analysis using GCMC simulation, temperature-dependant binding behaviour using canonical MC, guest dynamics via MD simulation as well as charge transfer interactions using Bader charges and charge density difference), but we have also shown how often molecular simulation and SSNMR spectroscopy are in agreement, be it through number of binding sites, strength of guest

binding or temperature-dependant guest interactions. We are capable of providing explanations for phenomena which are poorly understood using SSNMR, such as detailed times of residence on a per binding site basis as well as possible mechanisms for switching of distinct guest binding sites. Thanks to all the results of this work and prior efforts, it is clear that the combination of SSNMR and molecular simulation forms a powerful analytical procedure for characterizing MOFs, and this novel set of microscopic characterization techniques represents one of many efforts aimed at applying MOFs as adsorbents commercially.

4.6 References

(1) Sutrisno, A.; Terskikh, V. V; Shi, Q.; Song, Z.; Dong, J.; Ding, S. Y.; Wang, W.; Provost, B. R.; Daff, T. D.; Woo, T. K.; Huang, Y. *Chemistry* **2012**, *18*, 12251–9.

(2) Taulelle, F.; Bouchevreau, B.; Martineau, C. *CrystEngComm* **2013**, *15*, 8613.

(3) Harris, R. K.; Wasylishen, R. E.; Duer, M. J. *NMR Crystallography*; 1st ed.; Wiley, 2009; p. 520.

(4) Xu, J.; Terskikh, V. V; Huang, Y. *Chemistry* **2013**, *19*, 4432–6.

(5) Mowat, J. P. S.; Miller, S. R.; Slawin, A. M. Z.; Seymour, V. R.; Ashbrook, S. E.; Wright, P. a. *Microporous Mesoporous Mater.* **2011**, *142*, 322–333.

(6) Bryce, D. L.; Bernard, G. M.; Gee, M.; Lumsden, M. D.; Eichele, K.; Wasylishen, R. E. *Can. J. Anal. Sci. Spectrosc.* **2001**, *46*, 46–82.

(7) Duer, M. J. *Solid-State NMR Spectroscopy: Principles and Applications*; 1st ed.; John Wiley & Sons, 2002; p. 592.

(8) Koller, H.; Weiss, M. *Top. Curr. Chem.* **2012**, *306*, 189–227.

(9) Smith, W.; Forester, T. R. *J. Mol. Graph.* **1996**, *14*, 136–141.

(10) Yang, Q.; Vaesen, S.; Vishnuvarthan, M.; Ragon, F.; Serre, C.; Vimont, A.; Daturi, M.; De Weireld, G.; Maurin, G. *J. Mater. Chem.* **2012**, *22*, 10210.

(11) Volkringer, C.; Meddouri, M.; Loiseau, T.; Guillou, N.; Marrot, J.; Férey, G.; Haouas, M.; Taulelle, F.; Audebrand, N.; Latroche, M. *Inorg. Chem.* **2008**, *47*, 11892–901.

(12) Wu, L.; Xue, M.; Qiu, S.-L.; Chaplais, G.; Simon-Masseron, A.; Patarin, J. *Microporous Mesoporous Mater.* **2012**, *157*, 75–81.

(13) Foo, M. L.; Horike, S.; Inubushi, Y.; Kitagawa, S. *Angew. Chem. Int. Ed. Engl.* **2012**, *51*, 6107–11.

(14) Valvekens, P.; Jonckheere, D.; De Baerdemaeker, T.; Kubarev, A.; Vandichel, M.; Hemelsoet, K.; Waroquier, M.; Van Speybroeck, V.; Smolders, E.; Depla, D.; Roeffaers, M. B.; De Vos, D. E. *Chem. Sci.* **2014**.

(15) Vaidhyanathan, R.; Iremonger, S. S.; Shimizu, G. K. H.; Boyd, P. G.; Alavi, S.; Woo, T. K. *Science* **2010**, *330*, 650–3.

(16) Grimme, S. *J. Comput. Chem.* **2006**, *27*, 1787–99.

(17) Grimme, S. DFT-D3 - DFT-D3 - A dispersion correction for density functionals, Hartree-Fock and semi-empirical quantum chemical methods http://www.thch.uni-bonn.de/tc/index.php?section=downloads&subsection=DFT-D3&lang=english.

(18) Park, J.; Kim, H.; Han, S. S.; Jung, Y. *J. Phys. Chem. Lett.* **2012**, *3*, 826–829.

(19) Jensen, F. *Introduction to Computational Chemistry*; 2nd ed.; John Wiley & Sons, 2007; pp. 299–303.

(20) Henkelman, G.; Arnaldsson, A.; Jónsson, H. *Comput. Mater. Sci.* **2006**, *36*, 354–360.

(21) Sanville, E.; Kenny, S. D.; Smith, R.; Henkelman, G. *J. Comput. Chem.* **2007**, *28*, 899–908.

(22) Tang, W.; Sanville, E.; Henkelman, G. *J. Phys. Condens. Matter* **2009**, *21*, 084204.

5 – Conclusion

5.1 Summary

There were two, distinct goals for this two-part thesis. The goal of the first part of this thesis was to further study the performance of the popular N_2-TraPPE force field for N_2 gas adsorption in MOFs, and to develop an improved force field for high accuracy N_2 adsorption in MOFs.

In Chapter 3, we first demonstrate the failure of N_2-TraPPE to reproduce quantitative uptake data in MOFs. N_2-TraPPE (in combination with UFF and ESP charges for the framework atoms) is the N_2 force field in current widespread use for simulating gas adsorption in MOFs, and we have found that in all cases it significantly overestimates experimental N_2 uptake.[3] This prompted us to use the N_2-TraPPE force field parameters, which are designed to reproduce liquid vapour equilibria for pure N_2 gas, as the starting point for our modified parameters, which we call the Nitrogen In MoFs (NIMF) model. The NIMF force field parameters are fitted to a wide variety of experimental coordinatively saturated MOF isotherm data from literature, and further validated with supplementary experimental MOF isotherm data. Our tests show NIMF to be transferable for any coordinatively saturated MOF, and its use results in much higher accuracy uptake isotherms. Indeed, calculated CO_2/N_2 selectivies using NIMF ranged from 3 to 6 times higher than those found using N_2-TraPPE, indicating that materials studied computationally with N_2-TraPPE would have been judged to be of lesser interest for carbon capture. NIMF can therefore be used to accurately predict N_2 uptake, CO_2/N_2 selectivity (for carbon capture) and O_2/N_2 selectivity (for air separation) in MOFs which have not yet been synthesized. This

is expected to greatly benefit the development of emerging carbon capture and oxyfuel-combustion technologies.

In the second part of this thesis work, we aimed to provide an in depth molecular simulation study of CO_2 and DMF adsorption in the MOFs MIL-68(In)[1] and $Ba_2TMA(NO_3)$[2]. This is done with the broader goal of complementing the SSNMR experiments carried out by Professor Yining Huang's group on MIL-68(In) and $Ba_2TMA(NO_3)$ in order to contribute our findings to the growing field of NMR crystallography.

In Chapter 4, we present and interpret our molecular simulation results for gas adsorption in two different MOFs with two non-equivalent metal SBUs, MIL-68(In) and $Ba_2TMA(NO_3)$. We have made use of a wide variety of molecular simulation techniques to analyze the host-guest interactions, including grand canonical Monte Carlo (GCMC) simulations, periodic DFT calculations, molecular dynamics (MD) simulations, canonical Monte Carlo (for MIL-68(In)) and Bader charge/charge density difference studies (for $Ba_2TMA(NO_3)$). We also find that in all instances, our simulation data is in very good agreement with the SSNMR experimental results collected by the Huang group.

For MIL-68(In), our molecular simulation studies showed no direct interaction between CO_2 and the In centers found in MIL-68(In), which is in agreement with experimental ^{115}In SSNMR results which show no change in NMR signal between the evacuated MOF and the MOF containing adsorbed CO_2. MIL-68(In) contains two distinct channel types (a smaller triangular channel and larger hexagonal channel), which we have found enables it to have 4 distinct binding sites. **B1-CO_2** is found in center of the triangular channel, and is found directly beneath the linkers; **B2-CO_2** is also in the center of the triangular channel, but

instead of being directly under the linkers, is found in the interstices formed by the linkers; **B3-CO_2** is found near In2 SBUs and interacts with several atoms surrounding the In2 center, mostly through H-bonds and finally **B4-CO_2** is a weaker binding site which only will appear at higher pressures and H-bonds directly with the OH group connecting the infinite In1 chain. Our findings agree well with ^{13}C SSNMR data collected by the Huang group, which identifies three unique binding sites within MIL-68(In) (**B4-CO_2** has a lower probability in comparison to **B1-CO_2**, **B2-CO_2** and **B3-CO_2**). **B1-CO_2** and **B2-CO_2** are stronger in binding energy than **B3-CO_2** and **B4-CO_2**, but they also appear to be less well localized within their respective binding pockets due to multiple favourable orientations than **B4-CO_2** and especially **B3-CO_2**. The binding sites we identify are compared with the CO_2 binding sites found by Yang *et al.* for isostructural MIL-68(Al).[4] The most striking difference is that their probability density plots show the opposite trend in terms of probability for the hexagonal channel binding sites (ie. They identify the same binding sites **B3-CO_2** and **B4-CO_2**, but they identify **B4-CO_2** as being of a higher probability than **B3-CO_2**). This suggests that the metal center identity may play some role in this change.

The effect of temperature-effects on the probability density distribution of CO_2 in MIL-68(In) was also investigated. At 403K, CO_2 is less restricted to the binding sites we identified. At 150K, highly localized probability densities show that the CO_2 molecules are almost completely restricted to the identified binding sites over the course of the canonical MC simulation. At 293K, a situation somewhere between that described for 150K and 403K is observed. These simulation results all match temperature-dependant ^{13}C SSNMR-spectra collected by the Huang group, which show CO_2 in a bound, complex state at 150K, whereas at 403K the sole SSNMR peak observed very much resembles that of free CO_2.

CO_2 dynamics were investigated in MIL-68(In) using MD simulations. Average residence times were obtained for all binding sites (**B1-CO_2:** ~84 ps, **B2-CO_2:** ~120 ps, **B3-CO_2:** ~ 17 ps **B4-CO_2:** ~ 8 ps) and match the relative trend in binding energies. Of particular interest was the discovery that the loading of the triangular channel could greatly change the hop rate of a CO_2 molecule from site **B1-CO_2** to **B2-CO_2** and vice versa: indeed, residence times were around 10 times longer when every binding site in the 8-site channel was occupied vs. when only 6 sites were occupied.

As for DMF in MIL-68(In), three major binding sites are identified. Two binding sites (**B1-DMF** and **B3-DMF**) are found in the hexagonal channel, and interact with the framework in a similar way as **B3-CO_2** and **B4-CO_2** found for CO_2. Interestingly, the DMF binding site (**B1-DMF**) which is analog to **B4-CO_2** is the strongest of all, whereas **B4-CO_2** is the weakest of all CO_2 binding sites found. The other DMF binding site is found in the triangular channel (**B2-DMF**), and the carbon on DMF interacts with oxygen atoms which interconnect In2 chains. A comparison of the strongest CO_2 hexagonal channel binding site (**B3-CO_2**) and the strongest DMF binding site (**B1-DMF**) shows that the binding energy is significantly stronger for the DMF binding site, and the strongest DMF binding site has a higher probability density near In1 while the strongest hexagonal pore CO_2 binding site shows a higher probability density near In2. This is consistent with the ^{115}In NMR spectral data, as greater changes are observed in the In1 signal from the as-made (DMF-solvated) MOF compared to that of the activated MOF.

In our study of $Ba_2TMA(NO_3)$, we used GCMC simulation to identify a single binding site for DMF (**BB1-DMF**). The short **BB1-DMF** oxygen-Ba distances found for both Ba1 (3.01 Å) and Ba2 (3.16 Å) suggest that the binding site may interact with both of the non-

equivalent metal sites. This corresponds well with XRD-derived experimental values (Ba1-O distance: 2.955 Å and Ba2-O distance: 3.189 Å). Charge density difference and Bader charge calculations confirm that **BB1-DMF** interacts with both metal centers, as charge density differs on both Ba1 and Ba2 metal centers binding to DMF compared to the same metal centers found in evacuated $Ba_2TMA(NO_3)$. Bader charge analysis shows that polarization interactions take place between **BB1-DMF** and the Ba centers.

As for CO_2, a main binding site (**BB1-CO_2**) and secondary binding site (**BB2-CO_2**) are observed in $Ba_2TMA(NO_3)$. **BB1-CO_2** interacts with the framework in roughly the same area and in the same way as the DMF binding site found in $Ba_2TMA(NO_3)$, and from the recorded distances also appears to interact with both Ba centers (Ba1-O: 3.14 Å and Ba2-O: 3.60 Å). There are however a few distinguishing features between **BB1-CO_2** and **BB1-DMF**. First, the other **BB1-CO_2** oxygen (ie. The oxygen which is not binding to Ba1 and Ba2 like with DMF) interacts with a different Ba1 center (referred to as Ba1-b, whereas the main binding Ba1 is referred to hereafter as Ba1-a). This interaction is evidenced by the proximity between **BB1-CO_2** and Ba1-b, turning dispersion interactions on and off for DFT optimization calculations and charge density difference results. Second, the distances are skewed so that the **BB1-CO_2** oxygen is closer to Ba1 (3.14 Å) than Ba2 (3.60 Å). Whether or not this suggests **BB1-CO_2** interacts more strongly with Ba1 than Ba2 however seems debatable, as Bader charge analysis and charge density difference provide differing conclusions. In any case, both Bader charge analysis and charge density difference results show that there are polarization interactions between **BB1-CO_2** and Ba atoms, which are weaker compared to those found for **BB1-DMF**. Our charge density difference and Bader charge results do suggest that the CO_2 binding site interacts with both metal centers (Ba1-a

and Ba2) to some extent, as well as weakly with the second Ba1 site (Ba1-b). The other CO_2 binding site (**BB2-CO_2**) only appears at higher isosurface probability, and cooperatively binds through interaction with **BB1-CO_2** as well as with a framework NO_3^- oxygen. This cooperative binding interaction has been observed in other MOFs.[5] The ^{13}C SSNMR data acquired by the Huang group for CO_2 adsorbed on $Ba_2TMA(NO_3)$ identifies two different CO_2 binding environments in the MOF, which is in perfect agreement with our results.

As was done with MIL-68(In), the dynamics of CO_2 in the MOF were studied using MD. The ordering of the average residence times for **BB1-CO_2** (~200 ps) and **BB2-CO_2** (~50 ps) is as expected given the relative strength of these two binding sites. A single CO_2 molecule was often seen hopping from one site **BB2-CO_2** to another site **BB2-CO_2** but never from a site **BB1-CO_2** to another site **BB1-CO_2**. Additionally, a site **BB1-CO_2** is consistently occupied directly after the immediate neighbouring site **BB2-CO_2** has been visited, which indicates that a specific transition state may be required for **BB1-CO_2** to be occupied.

Throughout this thesis, we have shown the value of molecular simulation for characterizing MOFs in many different ways. We have shown how our molecular simulation results are in good agreement with SSNMR spectroscopy experiments (Chapter 4). Additionally, our computations are capable of providing insight on aspects, such as molecular dynamics, which SSNMR experiments cannot provide many details about. We have also developed a new force field for gas uptake and selectivity predictions for even better agreement between computational and experimental results (Chapter 3). In addition to reproducing the correct data on exisiting MOFs, NIMF will also allow for high accuracy uptake and selectivity predictions in hypothetical MOFs. From these two studies, it is clear that molecular simulation can greatly benefit the study of MOFs in different ways. From

microscopic materials characterization to predictions regarding the macroscopic gas uptake isotherms, it is our hope that our efforts are a step forward in the development of higher performance materials meant for applications which have the potential to benefit global populations as well as the environment.

5.2 Future work

5.2.1 NIMF Force Field

The primary objective in development of the NIMF force field was to create a quick, high accuracy method for determining the single-component uptake isotherms for N_2 in MOFs. This is of special importance within the Woo group, because a large hypothetical MOF database has been created (> 1 million different MOF structures and counting), and screening the structures for desirable properties is currently underway. One application of great interest is sorbents for carbon capture, and a particularly important parameter for MOFs applied in this context is the CO_2/N_2 selectivity. Using the NIMF parameters, screening of the database for N_2 uptakes and CO_2/N_2 selectivities is currently underway.

Up to date, experimental isotherms collected to gain insight on gas separations have mostly consisted in the collection of single-component isotherms for the gases to be separated at the relevant temperature and pressure conditions. This is because experimental multi-component gas adsorption experiments are more challenging the the single-component experiments in practice. In contrast, multi-component gas adsorption studies derived from molecular simulation are relatively simple and routinely performed. One future direction we wish to explore with the NIMF model would be to test its ability to be used in conjunction with other gas force fields, particular CO_2 and O_2 force fields.

Chapter 3 provided insight on the macroscopic effect of a change in the N_2 force field's Lennard-Jones parameters through comparison of N_2-TraPPE and NIMF uptake isotherms. However, a study of the microscopic effects of the change in parameters, such as changes in the location and/or number of binding sites, was not studied. This could prove to be a very interesting future direction for the work on the NIMF.

Finally, the best assessment of NIMF will be provided through comparison of even more simulated isotherms with a wide variety of experimental data. This is already in progress within the Woo group. The improved prediction offered by NIMF compared to N_2-TraPPE for Ni4-PyC (see section in Chapter 3), a MOF which has yet to be published and was provided to the Woo group for study by Dr. Ramanathan Vaidhyanathan.[6] Therefore, comparisons of N_2 uptakes derived by experiment, NIMF and N_2-TraPPE for new MOFs is already an ongoing research interest.

5.2.2 Molecular Simulation in Ba_2TMANO_3 & MIL-68(In)

The Huang group has attempted to reproduce the ^{13}C SSNMR lineshape for CO_2 adsorbed in MIL-68(In) using an approximate model generated using the Exchange Program for Relaxing Spin Systems (EXPRESS).[7] The EXPRESS software simulates the dynamics of a guest using approximate motions (ie. Hopping from one site to another, cone-based rotational motion, etc.) and can successfully reproduce static and MAS SSNMR chemical shift anisotropy. The parameters the Huang group found which provide a good fit for the SSNMR lineshape seem to suggest that the binding sites in the hexagonal channels may be stronger than those found in the triangular channels, which is in direct conflict with our simulation findings. We determined MIL-68(In) to have four unique binding sites of varying strength, and the MOF has non-equivalent metal centers in addition to two geometrically

very different accessible channels. Because of this, the description of the dynamics within MIL-68(In) is incomplete using a simple model with few parameters. Although the simple EXPRESS model derived by the Huang group provides a good representation of the SSNMR lineshape, other models may be able to provide a better fit. Molecular dynamics (MD) simulations were carried out in this thesis to determine the interactions of CO_2 through time with MIL-68(In), but apart from the quantitative residence times provided, the data extracted from the MD simulations provided qualitative insight on the how a molecule switches from one binding site to another. In the future, we plan to more rigorously analyze the MIL-68(In) MD trajectories to extract meaningful descriptions of guest motions and guest exchange mechanisms over the course of the 40 ns simulation using an in-house developed analysis code. This information can be used to develop a new model to reproduce the MIL-68(In) ^{13}C SSNMR lineshape for adsorbed CO_2. It is foreseeable that such an analysis will also be beneficial for study of CO_2 dynamics in $Ba_2TMA(NO_3)$.

Another future direction in relation to this project would be, broadly, the reproduction of the ^{13}C SSNMR spectral data from MD simulation trajectories. This has previously been explored by Alavi *et al.* for CO_2 molecules found within clathrate hydrate cages.[8,9] A major advantage of this technique is that assumptions on the guest motion within the host need not be made, as the lineshape is extracted directly from the MD trajectory.

5.3 Thesis Related Publications

1. **Provost, B.R.**; Daff, T.D.; Woo, T.K. "Parameterized N_2 Model for Improved Simulated CO_2/N_2 and O_2/N_2 Selectivity in Metal Organic Frameworks" *Submitted to Langmuir*

2. Wang, W.D.; **Provost, B.R.**; He, P.; Woo, T.K.; Wang, W.; Huang, Y. "^{115}In, ^{17}O and ^{13}C Solid-State NMR Spectroscopy and Computational Modelling for Characterization of the Metal-Organic Framework MIL-68(In)" *Manuscript in preparation*

3. Wang, W. D.; **Provost, B.R.**; Woo, T.K.; Wang, W.; Huang, Y. "$^{135/137}$Ba and ^{13}C Solid-State NMR Spectroscopy and Computational Modelling for Characterization of $Ba_2TMA(NO_3)(DMF)$." *Manuscript in preparation*

5.4 References

(1) Volkringer, C.; Meddouri, M.; Loiseau, T.; Guillou, N.; Marrot, J.; Férey, G.; Haouas, M.; Taulelle, F.; Audebrand, N.; Latroche, M. *Inorg. Chem.* **2008**, *47*, 11892–901.

(2) Foo, M. L.; Horike, S.; Inubushi, Y.; Kitagawa, S. *Angew. Chem. Int. Ed. Engl.* **2012**, *51*, 6107–11.

(3) Potoff, J. J.; Siepmann, J. I. *AIChE J.* **2001**, *47*, 1676–1682.

(4) Yang, Q.; Vaesen, S.; Vishnuvarthan, M.; Ragon, F.; Serre, C.; Vimont, A.; Daturi, M.; De Weireld, G.; Maurin, G. *J. Mater. Chem.* **2012**, *22*, 10210.

(5) Vaidhyanathan, R.; Iremonger, S. S.; Shimizu, G. K. H.; Boyd, P. G.; Alavi, S.; Woo, T. K. *Science* **2010**, *330*, 650–3.

(6) Vaidhyanathan, R.; De Luna, P.; Daff, T. D.; Woo, T. K. (unpublished results).

(7) Vold, R. L.; Hoatson, G. L. *J. Magn. Reson.* **2009**, *198*, 57–72.

(8) Alavi, S.; Dornan, P.; Woo, T. K. *Chemphyschem* **2008**, *9*, 911–9.

(9) Olivieri, A. C. *Concepts Magn. Reson.* **1996**, *8*, 279–292.

6 – Appendices

A. Python Scripts

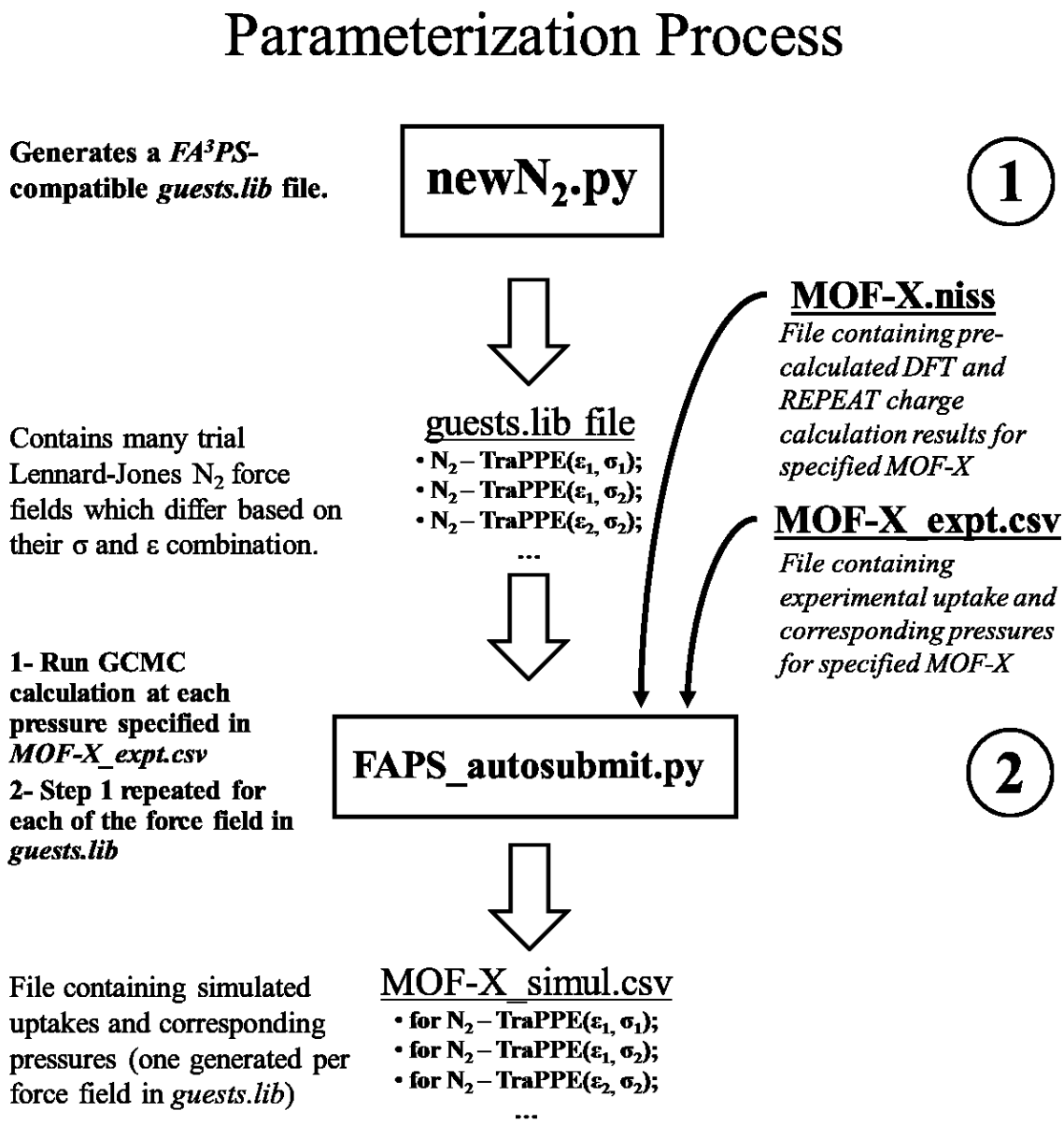

Parameterization Process (cont'd)

File containing simulated uptakes and corresponding pressures (one generated per force field in *guests.lib*)

MOF_simul.csv
- **for N_2 – TraPPE(ε_1, σ_1);**
- **for N_2 – TraPPE(ε_1, σ_2);**
- **for N_2 – TraPPE(ε_2, σ_2);**

...

MOF-X_expt.csv

Apply equation 4 (see section 3.4.2) to data in all *MOF-X_simul.csv* and MOF-X_exp.csv

least_squares_grid.py

3

A grid which shows S_{ave} as a function of changes in Lennard-Jones parameters σ and ε.

MOF-X_LJ_master.csv
- **for N_2 – TraPPE(ε_1, σ_1);**
- **for N_2 – TraPPE(ε_1, σ_2);**
- **for N_2 – TraPPE(ε_2, σ_2);**

...

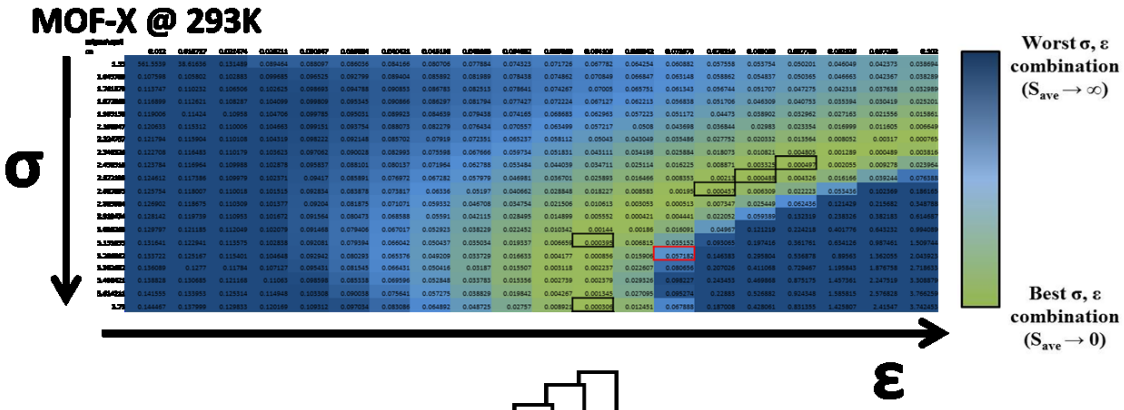

Repeat for all temperatures and all MOFs & Produce Combined S_{ave} Grid manually

B. Weighting Scheme

Table 6-1. *MOF names and corresponding temperature and pressure ranges used in parameterization set. Weighting factors 1-5 are: Metal Center Type weight (1), Organic Secondary Building Unit (SBU) Type weight (2), MOF Similarity (3), Temperature weight (4) and Pressure Range (5). These five factors are multiplied to obtain the "Final Weighting" which is used in parameterization.*

MOF Name	*T (K)*	*Max P (bar)*	*1*	*2*	*3*	*4*	*5*	*Final Weighting (ω_{ij})*
CALF-15	293	1	0.75	1	1	0.9	1	0.675
CPF-6	273	1	0.75	1	1	0.75	1	0.5625
CROFOUR-1-Ni	298	1	1	0.8	1	1	1	0.8
MOF-177	293	1	0.75	1	0.6	0.9	1	0.405
MOF-177	298	1	0.75	1	0.6	1	1	0.45
MOF-177	303	1	0.75	1	0.6	0.9	1	0.405
MOOFOUR-1-Ni	298	1	1	0.8	1	1	1	0.8
NJU-Bai3	273	20	0.75	1	0.8	0.75	0.8	0.36
NJU-Bai3	298	20	0.75	1	0.8	1	0.8	0.48
PCN-26	195	1	0.75	1	0.6	0.3	1	0.135
PCN-26	273	1	0.75	1	0.6	0.9	1	0.405
PCN-26	298	1	0.75	1	0.6	1	1	0.45
TIF-A1	273	1	0.75	1	0.8	0.75	1	0.45
TIF-A1	298	1	0.75	1	0.8	1	1	0.6
CoHLH2O2	273	1	1	1	0.8	0.75	1	0.6
CoHLH2O2	298	1	1	1	0.8	1	1	0.8
Cubpy1-SiF6	298	1	0.75	1	1	1	1	0.75
Cubpy2-SiF6	298	1	0.75	0.8	1	1	1	0.6
∞[Cu(Me-4py-trz-ia)]	273	40	0.75	1	0.6	0.75	0.6	0.2025
∞[Cu(Me-4py-trz-ia)]	298	40	0.75	1	0.6	1	0.6	0.27
∞[Cu(Me-4py-trz-ia)]	323	40	0.75	1	0.6	0.65	0.6	0.1755
ZIF-8	298	25	0.75	1	0.45	1	0.8	0.27
ZIF-8	308	25	0.75	1	0.45	0.85	0.8	0.2295
ZIF-8	318	25	0.75	1	0.45	0.7	0.8	0.189
ZIF-8	328	25	0.75	1	0.45	0.65	0.8	0.1755
NiDABCO	294	25	1	1	0.6	0.9	0.8	0.432
NiDABCO	314	25	1	1	0.6	0.75	0.8	0.36
NiDABCO	350	25	1	1	0.6	0.5	0.8	0.24